

Award Accounts

The Chemical Society of Japan Award for Creative Work for 2006

Three-Dimensional Micro- and Nano-Structuring of Materials by Tightly Focused Laser Radiation

Saulius Juodkazis,[1] Vygantas Mizeikis,[1] Shigeki Matsuo,[2] Kosei Ueno,[1] and Hiroaki Misawa*[1]

[1]Research Institute for Electronic Science, Hokkaido University, Sapporo 001-0021

[2]The University of Tokushima, 2-1 Minamijosanjima, Tokushima 770-8506

Received July 9, 2007; E-mail: Misawa@es.hokudai.ac.jp

Three-dimensional laser microfabrication blends microscopy, optical nonlinear phenomena, photomodification, laser trapping, and creates novel possibilities for fabrication of micro- and nano-structures in a wide range of materials. This work reviews various implementations of laser photo-structuring and micromanipulation applied to photo-modification of various materials: glasses, crystals, polymers, gels, and liquid crystals.

1. Introduction

High-resolution three-dimensional (3D) optical structuring of materials is an actively developing area of fundamental and applied materials research. Although still in its infancy, it has nevertheless produced some practical contributions to modern science and technology by supplying high-quality nano-/micro-structures defined with high spatial resolution.[1] Optical fabrication in three dimensions has especially benefited from the advent of high-power ultrafast picosecond and femtosecond lasers, because shorter pulses invoke stronger nonlinearities, which enable one to induce more efficient and better-localized photomodification of 3D materials.

Photomodified materials are expected to open new application fields in chemistry and material science due to their altered physical and chemical properties, e.g., crystalline materials such as sapphire and quartz become amorphous and wet-etchable after modification induced by micro-explosion at the focal region of a tightly focused ultra-short pulse. The shock-modified materials can possess a different crystalline structure and form high-pressure phases with properties never used before for practical applications.[2–7] Control over phase transitions and, especially glass transition, becomes feasible due to very fast thermal quenching rates when sub-1 ps pulses are employed. Ultra-fast thermal quenching is expected to create new ceramics, glasses, and new composite nano-structured materials.

Tightly focused laser beam have been successfully applied to cell transfection, perforation, and gene transfer.[8,9] This technique also relies on a phase transformation at the focus of a laser beams/pulse where a bubble is formed by micro-explosion. The pressure generated by the micro-explosion can be used for a precise modification of bio-objects, organelles, and cells. This technique can be incorporated into micro-fluidic chips and micro-total analysis systems with variety of biological and chemical applications.

Photonic crystals (PhCs)[10,11] (see, Ref. 12 for a recent review) are yet another 3D micro-structures which are expected to impact modern science and technology. In chemistry, control over the rate of chemical reactions can be achieved via modifications of spontaneous emission in a 3D PhC cavity with a full photonic bandgap (similarly to the Purcell effect in a 1D cavity[13]). Also, new pathways of reactions via excited states can become feasible.

Currently, femtosecond laser fabrication has achieved resolution of surface patterning by self-organized ripple structures and controlled photo-polymerization at the 20–200 nm feature size. At these dimensions the local field enhancement effects begin to play an important role[14] and such nano-structures are prospective in sensor applications based on surface enhanced Raman scattering. At even smaller ≈1–10 nm feature size and correspondingly larger enhancements of local field, the sensitivity required to achieve a detection level of single molecular emission can be achieved. This is expected to open new directions in analytical chemistry. Recent advances in plasmonics, where light field localization enters nanometer dimensions is very promising in this regard.[12] New light harvesting schemes based on nano-structured materials are highly expected in photo-voltaics for sustainable solar energetics and reduction of carbon footprint.[15] Materials with engineered electrical and magnetic properties, the metamaterials, are emerging with new optical properties and prospects to manipulate light propagation do to their particular nano-structure.[16]

Here, we outline the basic physical principles of high-resolution 3D optical photo-structuring techniques and present some of the results achieved in practice. It is shown that photomodification with resolution of tens-of-nanometers in all three dimensions has been achieved. Also, the mechanisms of laser

Published on the web April 10, 2008; doi:10.1246/bcsj.81.411

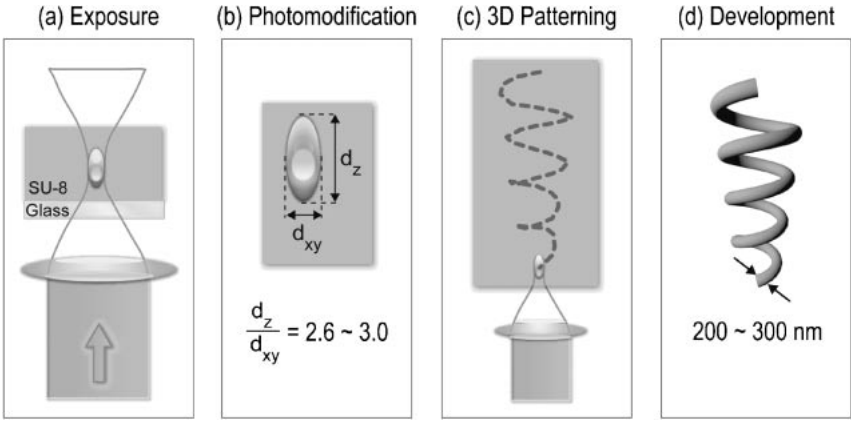

Figure 1. The principle of direct laser writing. (a) Tightly focused laser pulses induce permanent photomodification in the high-intensity region at the focal spot, in this case the material is photoresist SU-8, where photomodification is of latent nature and occurs as photoacid generation which subsequently triggers cross-linking of the underlying polymeric base. (b) Shape of the focal region defined by a constant-intensity surface is ellipsoidal, with major (axial) and minor (lateral) diameters d_z and d_{xy}, respectively. For tight focusing with an objective lens $NA = 1.35$–1.4, the elongation ratio is $d_z/d_{xy} \approx 2.8$. (c) Drawing continuous lines in SU-8 by sample (or focal spot) translation results in photomodification patterns. (d) After development these patterns become transformed into solid features. Their diameter can be adjusted by varying the laser beam intensity. In SU-8, features with lateral size of 200–300 nm are typically achievable and allow fabrication of extended, mechanically stable microstructures.

nano-micro-manipulation and structuring of soft matter gels and liquid crystals is presented. An optical control of local structure of gels and liquid crystals on a nanometer scale allows the creation of a non-local response with an effect extending up to tens-of-micrometers. The effects of self-organization allows the achievement of macro-size effect after impact on a micro-scale and, hence, have potential for practical applications.

2. Principles of Laser Photo-Modification of Materials

Currently, several methods of three-dimensional optical structuring of materials are known. To explain their most common principles we have chosen as an example the so-called direct laser writing (DLW) technique, which is schematically illustrated in Figure 1. As an example, we have chosen a negative photoresist SU-8[17] as the initial material for fabrication. Figure 1a shows a laser beam, tightly focused inside the film of SU-8 deposited on a glass substrate. The processes underlying 3D laser photo-structuring occur in the waist of the laser beam, where local intensity of the optical field is highest. The latter region can be reasonably well approximated by an ellipsoid, as is illustrated in Figure 1b. Use of focusing optics with high numerical aperture (*NA*), such as microscope oil immersion objectives with $NA \approx 1.4$ typically allows the reduction of the lateral dimensions of the ellipsoid to $d_{xy} \approx \lambda$, where λ is the laser wavelength. The use of highly localized irradiation brings conceptual elements of microscopy into laser photo-structuring. Returning to Figure 1a, one may note that in this scheme laser beam is depicted as being transmitted more or less freely through the sample. Hence, the sample is transparent at the laser wavelength (otherwise it would not penetrate the sample) everywhere, except for the focal region, where high-intensity radiation induces non-linear optical response, including absorption. SU-8 is transparent at wavelengths $\lambda > 360$–400 nm, and if laser wavelength is in near-infrared (NIR) spectral range, nonlinear two-photon absorption (TPA) or multi-photon absorption (MPA) processes are needed for photomodification. Due to nonlinearity, the size of absorbing region is even smaller than that of the focal spot. With modern high-power and pulsed laser systems, optical nonlinearities can be induced in a wide range of materials. Thus, elements of nonlinear optics enter the field of laser photo-structuring. The absorption can induce various kinds of permanent photomodification, for example, defects' generation at lower pulse energy and even void formation at high energy after an optical breakdown of the initial material at the location of the focal point. In the case of photoresist SU-8 considered here, photomodification occurs first as optical photoacid generation and later, during post-processing stages as thermal cross-linking of SU-8 constituent polymer. These changes remain latent until chemical development, which removes unexposed SU-8, leaving only the hard, cross-linked regions is applied.[18] By translating the laser beam inside the sample, complex patterns consisting of photomodified regions are recorded as illustrated in Figure 1c, which after development become transformed into corresponding solid features (Figure 1d). If photomodification occurs as optical damage, chemical development is generally not required, and patterns consisting of linear regions of less-dense material (or voids) are obtained immediately. Due to the tight focusing and optical nonlinearities, lateral size of the recorded features may be significantly smaller than the laser wavelength. For lasers operating at near-infrared and visible wavelengths, feature size of 200–300 nm is easily achievable and the fabricated structures are mechanically stable, provided that topology of the structure favors mechanical stability necessary to withstand capillary forces during development.[19] Photo-polymerized 3D structures with cross-sections comparable with tens of molecular diameters were demonstrated.[20]

3. Experimental Implementations of Laser Photo-Structuring

According to the previous section, 3D drawing is achieved

by translating the tip of a sharp "optical pen." The "pen" can access points inside the material due its transparency, and can fabricate the material due to its optical nonlinearity. Other elements, like sample/laser beam translation are optional, and in other implementations of laser microfabrication can be realized differently, or may be not needed at all. Below we will briefly describe DLW setup used in our studies.

A derivative of DLW, mostly aimed at parallelization of the drawing process, uses a micro-lens array (MLA) instead of a single lens. Drawing is then achieved simultaneously by multiple focal regions and allow fast fabrication of large periodic structures.

Another widely used method for parallelized fabrication is by multiple-beam interference (also known as holographic recording). In this technique the material is exposed to periodic intensity field of multiple interfering laser beams, which can simultaneously irradiate relatively large areas ($\approx$mm^2). This technique is mostly used with materials exhibiting non-destructive photomodification, such as photoresist SU-8. Since interference recording differs somewhat from the DLW, its practical implementation will be briefly described in this Section.

3.1 Implementation of Direct Laser Photo-Structuring. The photo-structuring of materials carried out in our studies was made using a basic DLW setup which with some modifications has been presented in our earlier work.[21–34] Its optical layout is shown in Figure 2. The same setup can be used for spectroscopic characterization of the processes within small focal volumes whose cross-sections are smaller than several micrometers.[35,36] As a laser source for photo-structuring a Hurricane X system (Spectra-Physics) operating at a variable repetition rate of up to 1 kHz, and having pulse duration and central wavelength $\tau_{\text{pulse}} = 120$ fs and $\lambda_{\text{pulse}} = 800$ nm, correspondingly was used. When needed, second harmonic of the same laser with central wavelength of 400 nm can be also used. The laser beam can be opened or blocked by an electro-mechanical shutter (not shown), and is coupled to Olympus IX71 optical microscope equipped with a dry or oil-immersion objective lenses. As high-resolution recording requires tight focusing, most often oil-immersion lenses with high numerical aperture of $NA \approx 1.0$–1.4 are used. The laser beam is coupled to the objective lens using a dichroic mirror, highly reflective

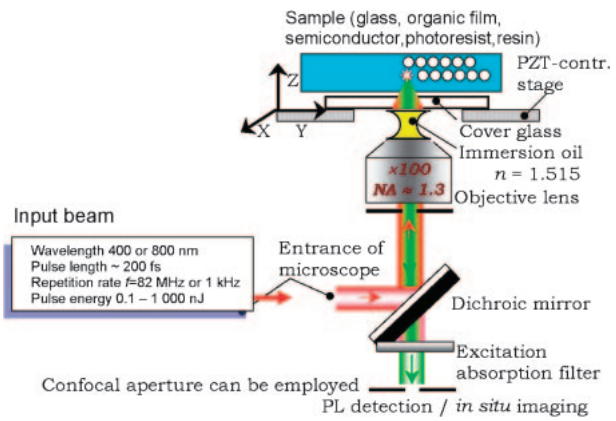

Figure 2. Schematic layout of experimental setup for DLW (see text for explanations).

at the laser wavelength(s), but transmissive at other spectral positions. Such setup enables one to collect photoexcited fluorescence, induced broadband continuum or transmitted radiation of an external illumination source mounted above the sample (not shown) for in situ imaging or spectral analysis. Rejection of unwanted radiation can be improved by using an excitation absorption filter, mounted below the dichroic mirror. The sample is mounted on a piezo-electric transducer (PZT)-controlled high precision 3D translation stage, which ensures positioning within the range of hundreds of micrometers with accuracy of a few nanometers. We have used a combination of P-517.2CL and P-518.ZCL stages from Physik Instrumente with a positioning range of up to 100 µm along each coordinate. The trajectory and speed of the stage motion as well as opening and closing of the shutter are controlled synchronously with the arrival of laser pulses by customized software running on a personal computer. As a result, the system can create discrete or contiguous exposure traces according to need. Discrete traces consist of non-connecting smallest exposed volumes (voxels), while continuous traces consist of overlapping voxels arranged into lines. The schematic picture in Figure 2 illustrates recording of discrete traces by optical damage. The possible range of samples may include dielectrics, semiconductors, or other materials transparent at the laser wavelength (mostly suitable for fabrication by optical damage), as well as photoresists and resins (mostly suitable for fabrication by optical cross-linking of polymers).

3.2 Implementation of a Multiple-Beam Interference Method. Various optical schemes used in fabrication by multiple-beam interference usually differ in ways the multiple interfering beams are obtained and converged on the sample. The most straightforward approach is to use multiple beam-splitters for obtaining a set of coherent beamlets, and a set of optical delay lines to ensure their temporal matching. However, such setups are cumbersome to align and are highly susceptible to mechanical disturbances.

In our studies, we use an optical scheme based on a diffractive beam splitter (DBS), which is highly suited for obtaining multiple, perfectly synchronized beamlets. Layout of microfabrication setup which uses DBS is shown in Figure 3.[19,37–42] The beam from the same femtosecond Ti:Sapphire laser system as in the previous Figure is passed through the DBS, which can be represented by a stack of parallel diffraction gratings having different groove orientations (most often the grooves are mutually perpendicular). Transmitted and diffracted orders of the first grating in the stack are further diffracted by the subsequent grating(s), and as a result a set of diverging beamlets is obtained. In practice, instead of stacked gratings, a single plate with complex transmission function of several gratings, recorded holographically, is used. Our setup employed various DBS elements, of which G1023A (from MEMS Optical, Inc.) can be mentioned as a typical example. The set of beamlets is subsequently collimated by achromatic lens and passed through the amplitude mask which selects the beamlets required for obtaining the desired 3D structure. Optical path length between the DOE and the sample is typically 20 cm. As the beamlets propagate in free space, they can be optionally passed through variable phase retarder (PR) plates (not shown) which set their mutual phases, helping to create complex 3D

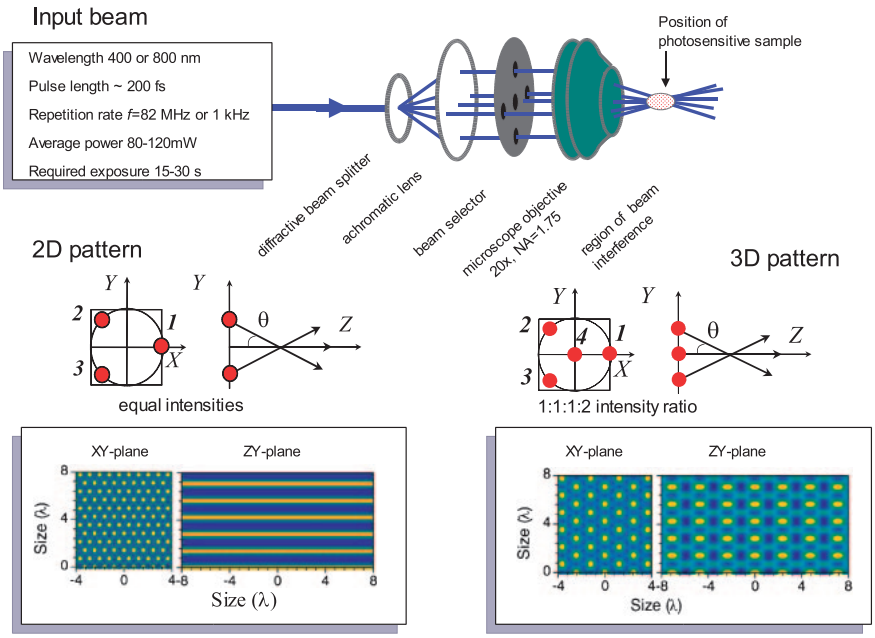

Figure 3. Schematic layout of experimental setup based on DBS for multiple-beam interference recording (top), three-beam configuration as seen on the beam selector plane, and their theoretically calculated interference intensity pattern (bottom left), the same for the case of four-beam interference (bottom right). In the calculated patterns the distances are calibrated in units of wavelength, λ; the angle of side beams with an optical axis was 60°.

interference patterns. The parallel, phase-controlled set of beamlets is then focused into the sample using a focusing lens having numerical aperture $NA = 0.5$–0.75. In this setup focusing is not as tight as in the case of DLW setup considered earlier. Although focusing is not essential for multiple-beam recording, it is helpful in achieving two goals: first, a moderately elevated average exposure needed for photomodification, and second, a relatively uniformly exposed area with lateral size of hundreds of micrometers. Typical samples used for interference recording technique are thin films of SU-8 photoresist, spin-coated on glass substrates to the thickness of about 10–50 μm.

DBS-based setup is highly suitable for use with pulsed ultrafast lasers. DBS produces so-called tilted laser pulses whose mutual coherency and zero time delay are maintained across the entire cross-sectional plane of their overlap on the sample, despite their different incidence directions. Therefore, the region of their spatial interference coincides with the region of overlap. For non-tilted pulses, such as those obtained with reflective beamsplitters, the interference region size is limited due to the requirement for the optical path difference not to exceed the pulse (coherence) length. When such pulses overlap with large mutual angles, this condition may be only met near the central part of the region of their spatial overlap.

Dimensionality and topology of the interference pattern depends on the number of interfering beams, their amplitudes and phases as well as incidence angles. A simple illustration of these circumstances is also given in Figure 3. For example, three interfering beams selected by the beam-selector plate as illustrated in the figure can create a 2D interference pattern with triangular periodic lattice in the x–y plane. To obtain 3D interference patterns, one needs a fourth beam coincident with the optical axis of the optical setup. In such case, triangular periodic lattice in the x–y plane is obtained, on which periodic modulation along the z axis direction is imposed. More complex intensity patterns can be obtained by adding more beams and by controlling their amplitudes and phases.

By mounting a CCD sensor in the sample plane and using a focusing lens with smaller magnification (compared to the lens used for the fabrication), one can monitor 2D intensity patterns at various positions along the z axis, and thus verify the qualitative correspondence between the patterns expected from numerical simulations and the actual intensity patterns without the need to actually record the structures.

4. Resolution of Laser Photo-Structuring

The maximum resolution of laser photo-structuring, achieved in the eventual recorded structures depends on several factors. The most important of them are listed below:

1. Spatial localization of the incident radiation. In DLW the degree of localization depends directly on the tightness of focusing. In multiple-beam interference recording the degree of localization depends on the period of interference pattern, which in turn depends on the mutual angles between the recording beams. In both cases theoretical limit of localization is close to the central wavelength of the laser.

2. Type and order of the optical nonlinearity defines the degree of spatial localization of nonlinear absorption. Nonlinear absorption first of all depends on the local intensity of the optical field, and due to nonlinearities spatial variation of the absorption is sharper than the intensity variation. Since permanent photomodification usually occurs above certain threshold exposure, by careful adjustment of the laser intensity photomodification can be localized within regions much smaller than the optical field. In DLW, this circumstance enables one to surpass the diffraction-limited resolution. In multiple-beam

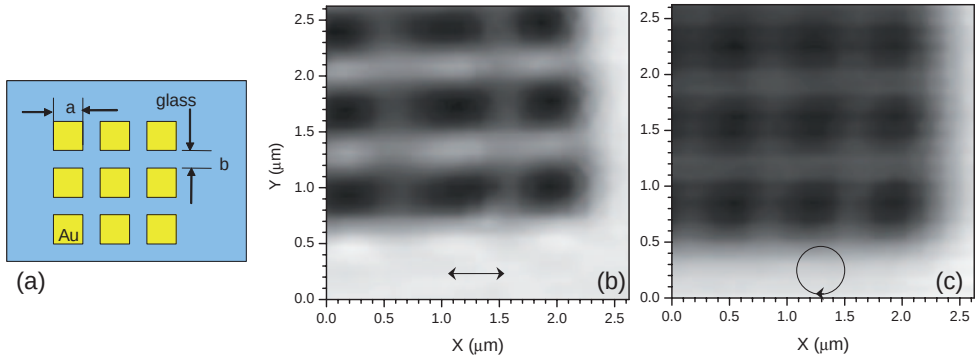

Figure 4. (a) A pattern of gold squares with $a = 0.5\,\mu m$ and $b = 0.3\,\mu m$ sputtered on cover glass substrate, (b) photoluminescence map of the dye excited and imaged through the above pattern using objective lens of $NA = 1.35$, acquired with a spatial scan step of 75 nm using horizontally polarized laser pulses with a central wavelength of 800 nm, (c) the same for circularly polarized pulses.

interference recording, size of the recorded features can be also reduced due to the nonlinearities.

3. Spatial spreading of excitation region can occur due to processes like thermal conduction, photoexcited carrier diffusion, and secondary excitation of the material, for example by fluorescence or broadband continuum. These processes usually decrease the resolution and are therefore unwanted.

4. Mechanical stability of the structures. In structures recorded by optical damage, destruction of significant volume fraction of the initial material may lead to strains, and their relaxation may induce structural collapse, thus rendering the structures unsuitable. For structures recorded by polymer cross-linking, mechanically weaker samples may be destroyed by the action of capillary forces during drying. All these processes are unwanted, as they limit the eventual achievable resolution.

Optical resolution achievable by a tightly focusing microscope objective lens with $NA = 1.35$ is illustrated by the following experimental example. Figure 4a shows schematic picture of a metallic mask, consisting of metal-coated square regions with side length of 500 nm, separated by gaps of 300 nm. Such mask was fabricated on a glass substrate using electron-beam lithography (EBL) and lift-off techniques. For the resolution test, the mask was mounted in place of the sample in the DLW setup (see Figure 2). On top of the mask, a thin layer of fluorescent dye dissolved in toluene was deposited by dropping; the dye was transparent at the laser wavelength of 800 nm, but fluorescence still could be excited via two-photon absorption (TPA). The laser beam was focused on the mask, and its focal spot was scanned with step of 75 nm in the sample plane, simultaneously recording the spectrally integrated intensity of dye fluorescence. Thus, this experiment essentially implemented imaging of the metallic mask by two-photon laser scanning microscopy. The fluorescence intensity maps acquired using linearly and circularly polarized laser pulses are shown in Figures 4b and 4c. In both images the gaps in the mask are resolved, which illustrates that resolution of the imaging is comparable to the gap width (300 nm), which is somewhat smaller than the laser wavelength. Comparison between the images in Figures 4b and 4c also shows that for a linearly polarized radiation the optical resolution is non-isotropic, and is higher along the direction perpendicular to the polarization direction. This feature is a consequence of ellipticity with elongation parallel to the incident beam polarization direction, seen in cross-sectional shapes of tightly focused, polarized laser beams according to vectorial Debye theory.[40] Circularly polarized beam, which contain both linear polarizations, have isotropic resolution as can be seen from Figure 4c. Numerical analysis of these images reveals that for circular polarization the resolution is about 350 ± 15 nm. This value is better than half of the laser wavelength and therefore clearly falls into the category of sub-diffraction limited resolution. As will be demonstrated later, practical recording in SU-8 by DLW typically provides resolution within the 200–400 nm range, which is very close to the above estimate.

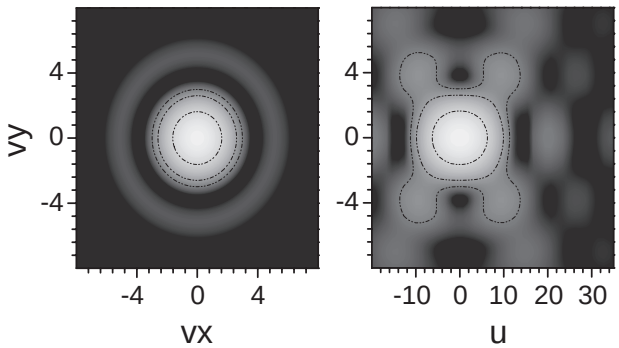

Figure 5. Cross-sectional maps of the laser beam intensity near the focal spot of the lens (waist of the beam), (a) in x–y plane, (b) in x–z or y–z planes. The intensity scale is logarithmic, the spatial coordinates are given in optical units of (v, u), the contour lines mark the 0.5, $\exp(-1)$, and $\exp(-2)$ levels.

4.1 Beam Delivery and Spatio-Temporal Distortions. For a plane wave with wavelength λ, focused by a lens with numerical aperture NA, transverse diameter of the focal spot can be roughly estimated as $d = 1.22\lambda/NA$, where λ is the wavelength of irradiation. This expression defines basic optical resolution of the DLW process.

To be more precise, intensity distribution at the focus can calculated using textbook expressions,[43] and the result is plotted in Figure 5 where the radial and axial optical coordinates v, u are given by:

$$v = \frac{2\pi}{\lambda}\frac{R}{F}r, \quad u = \frac{2\pi}{\lambda}R^2\left(\frac{1}{F} - \frac{1}{z}\right), \tag{1}$$

where r, z are the radial and axial coordinates in the focal plane, F is the focal length of the lens, R is the radius of the uniformly illuminated pupil, and λ is the wavelength. The point-spread function (PSF) shown in Figure 5 is presented in normalized optical coordinates and the actual r, z dimensions of the focus can be found for the specific R, F values (the numerical aperture is $NA = n\sin(\alpha) \simeq nR/F$, here n is the refractive index).

More precise estimations of the focal spot size would require accounting for the spatial profile of the laser beam, its clipping by the aperture of the objective lens,[44] vectorial nature of electromagnetic radiation[20,40] and spatio-temporal distortions of the laser radiation.[45,46] These factors typically reduce the resolution of DLW process. For interference recording, influence of beam and focusing imperfections is less important, compared with DLW. Nevertheless, the distortions may create unwanted variations in the average intensity and contrast of the interference fringes, and therefore should be minimized.

Minimization of spatial distortions requires elimination of aberrations introduced by the beam-guiding inaccuracy (for example off-axis propagation, koma and other third-order aberrations) and pulse tilt. This basically involves optimization of the linear optical system, which is widely studied and extensively covered by the existing literature.[47]

Elimination of temporal distortions is somewhat more difficult, especially with ultrafast lasers whose pulse shape can not be directly monitored in time-domain. For example, after passing through an Olympus oil-immersion microscope objective lens with $NA = 1.35$, the pulse length increases from 165 ± 10 fs to 258 ± 10 fs.[48] It is helpful to remember that most of the modern multi-component microscope objective lenses are optimized for image formation during observation, and not for focusing of ultra-short pulses. Microscope objectives comprise significant thickness of optical glass, and therefore provide a favorable environment for dispersive effects, which may stretch and distort temporal envelopes of even perfect Fourier transform-limited pulses. This situation is further complicated by frequency chirp, which is often present in laser pulses. Ultrashort pulses having high instantaneous intensities may undergo a variety of linear and non-linear spatio-temporal transformations, which in the extreme case may even lead to optical damage of the objective. Tilt of the pulse front which inevitably occurs upon propagation of pulse through prisms or reflection from gratings (present in setup and in stretcher-compressor of a regenerative amplifier) is equivalent to the axial aberration when different spatial wings of the same pulse are focused axially at different locations, thus smearing focal intensity. Measurement and compensation for a pulse tilt should be considered for high precision laser nano-/micro-structuring.[49]

In these circumstances one has to pay special attention to maintaining relatively low pulse energy during the experiments, and to use indirect monitoring techniques of the temporal shape of the pulses. Measurements of the pulse spectrum and autocorrelation function are the most widely available monitoring techniques, which allow determination of the pulse length, and verification of their transform-limited character. Another technique, which is currently gaining some popularity is a new implementation of a frequency-resolved optical gating (FROG) using a simplified device.[50] FROG allows simultaneous estimates of temporal and spectral parameters of pulses from the same experimental measurement, and can directly reveal pulse chirp and tilting. Thus, temporal optimization of laser output typically involves observation of the pulse spectrum and autocorrelation function or its FROG trace and adjustment of the optical system. In laser systems with regenerative amplifier (such as Spectra Physics' Spitfire or Hurricane systems used in our experiments), pulse parameters can be optimized by adjusting the pulse compressor.

Measurements of the pulse parameters are most easily conducted in front of the focusing lens, in which case they ignore the actual temporal shape of the pulses at the focus. Autocorrelation and FROG measurements after passing through the objective (or at the focus) are much more difficult and not always accurate, since they require one to use additional optics for recollimating the beam, or detectors adapted for measurements directly at the focal spot. As a crude practical measure, one can determine the conditions for optimal spatio-temporal focusing of ultrashort pulses by in situ observation of the broadband continuum or nonlinear photoluminescence at the focal spot. The optimum conditions can usually be identified by minimum energy of the incident pulses at which broadband continuum or emission can still be observed.

Recent years have seen increasingly active attempts to use active control of pulse parameters for laser photo-modification and structuring of materials. In these experiments, femtosecond laser pulses are spectrally modified using pulse shaper; in amplified laser systems this is done prior to pulse injection into the amplifier. Pulse shapers use liquid crystal or acousto-optical grating-based spectral modulation techniques. In our experiments, we use Dazzler acousto-optical pulse shaper (from Fastlite).[51] For example, by creating a spectral intensity envelope with a dip at the maximum, so called gain narrowing occurs in regenerative amplifier as shown in Figure 6. This pulse shaping technique can be further extended to produce multiple amplified pulses with different slopes, amplitudes, and phases from a single seed pulse. The threshold of photo-modification inside crystalline sapphire was demonstrated to

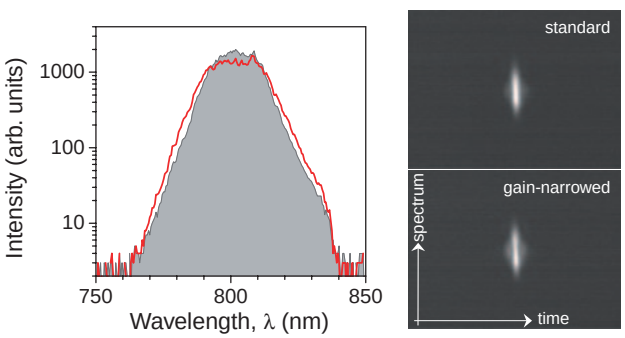

Figure 6. Comparison between the spectra of laser pulses from Spitfire (Spectra Physics) laser system (gray profile): nearly transform-limited pulse of 45 fs duration (line): gain-narrowed 40 fs duration pulse modulated using Dazzler prior to amplification. On the left their corresponding time-spectrum FROG traces are shown A spectral hole of 15% was an optimal condition for producing the shortest pulses.

be dependent on the relative phase of two pulses produced from a single femtosecond pulse using Dazzler.[49]

4.2 Role of Thermal Photo-Modification of Materials. It would be difficult to discuss extensively the rich variety of mechanisms of interaction between light and matter (see, Section **7** for detailed description of interaction between light and ionised solid or plasma). Therefore, here we will only briefly describe some of thermal phenomena accompanying exposure of materials to ultrashort laser radiation.

As a crude approximation, optical damage occurring at the focus of a lens can be regarded as analogous to the well-known burning of materials induced by a beam of focused sunlight. However, radiation of ultrafast lasers arrives to the material as a short pulse of nearly monochromatic and coherent radiation, capable of inducing nonlinear optical effects. Since thermal conductivity across the distances close to the lateral size of the focal region ($\approx$1 μm) during subpicosecond time interval is insignificant, the optical damage is almost independent of the pulse duration. Such regime of optical damage is often termed as non-thermal. An illustration of this regime is given in Figure 7, which shows a match, with the head cut through without ignition using a femtosecond laser beam. However, this fact does not prove the eventual non-thermal nature of optical damaging. Absent during the action of the laser pulse, in some materials thermal excitation may still occur during the later stages as a result of energy relaxation in which the optically delivered energy is transferred to the underlying lattice, and may become crucially important for the generation of high-pressure micro-regions and micro-explosions.[46,52]

The above processes are important mostly for inorganic solid glasses and fabrication by optical damage. Photoresists and liquid photo-curing resins are typically fabricated without structural damage. Nevertheless, thermal effects may be strongly present even in this regime. Thermal excitation typically comes from electrons, which are heated up by sub-picosecond pulses to temperatures close to 1000 K. Their emission according to Wien's law has a maximum at $\lambda_{max} = \beta/T$, with $\beta = 2.9 \times 10^{-3}$ K. This is secondary emission at wavelengths of 2–3 μm, corresponding to the relaxation of internal degrees of freedom of organic molecules. It can be reabsorbed, thus effectively heating the resist and facilitating cross-linking (See eq 2 in Section **5.6**).[53]

3D photo-polymerization can be also achieved via one photon absorption when irradiation is tightly focused.[54–56] The required nonlinearity of the polymerization occurs via temperature increase at the focal region.[55] Figure 8 shows 3D structures photo-polymerized by DLW using 355 nm and 20 ps laser pulses.[54] In order to achieve higher resolution and to exploit 3D character of photo-polymerization a two-photon absorption is necessary as was demonstrated in Ref. 57 by measuring the intensity dependence of transmission. The power law $\approx I^2$ for the feature size was established when femtosecond pulses at 400 nm central wavelength were scanned in Nopcocure800 (San Nopco, Inc.) at slow 1 kHz repetition rate which excluded thermal accumulation. Obviously, thermal excitation was also important for photo-polymerization in this case due to absorption into upper energy levels of polymer (see, absorption spectra shown in Figure 8).

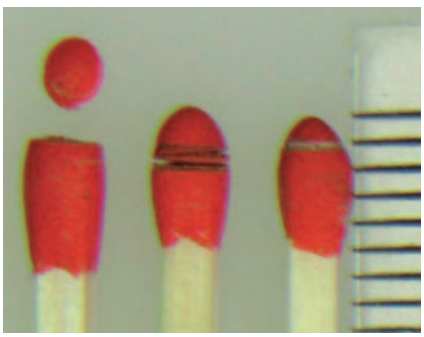

Figure 7. Laser cutting across a match head without ignition by femtosecond laser pulses with wavelength of 795 nm, temporal length of 150 fs, and a repetition rate of 1 kHz. Average power in the beam was 240 mW, focusing by a spherical lens with focal length of $f = 10$ cm, the cutting was done by manual scanning of the focal point. The ruler is calibrated in divisions of 1 mm.

5. Microstructures Produced by Direct Laser Photo-Structuring

In this Section, we will present examples of 3D microstructures fabricated in different materials by the DLW technique. The fabricated samples are mostly periodic structures intended for applications as photonic band gap (PBG) materials, also known as photonic crystals (PhC). Beside these structures, we will also demonstrate recording of single features in photoresist SU-8 with ultra-high resolution.

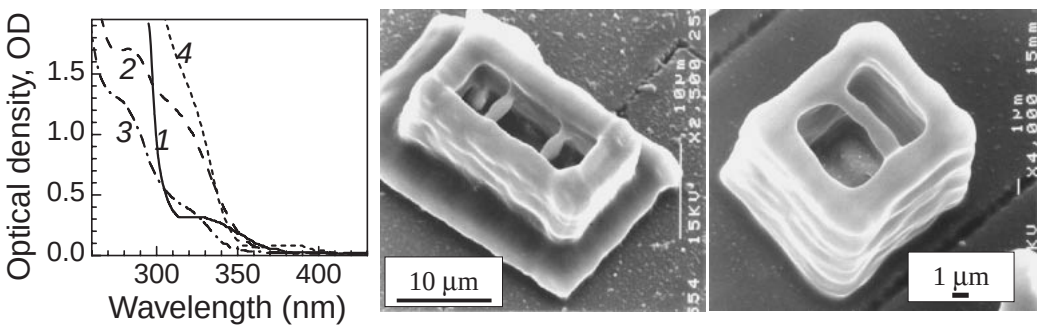

Figure 8. Absorption spectra of several acrylic resins: Nopcocure800 (1), SCR701 (2), SCR751 (3), and HS671 (4). Optical density, OD, was measured in a 1 cm cuvette filled with 1 wt % 1-methoxy-2-propanol solution of resin. SEM images of 3D structures solidified by 355 nm wavelength laser pulses of 20 ps duration in Nopcocure800.[54]

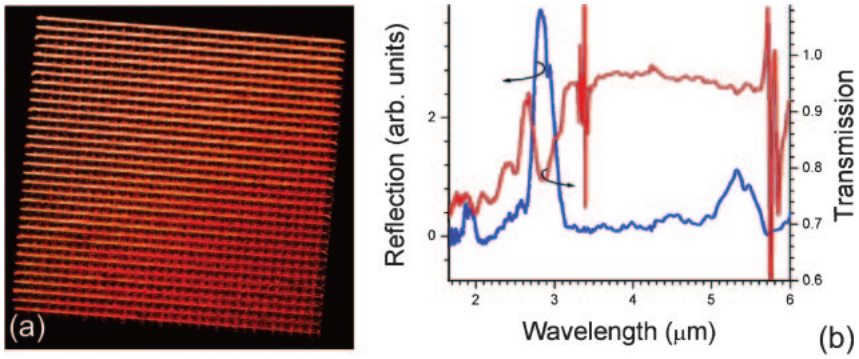

Figure 9. (a) Top plane of a woodpile structure in PMMA imaged by confocal laser scanning microcopy. DLW was done using 800 nm/150 fs pulses focused by $NA = 1.4$ objective lens. Separation between the nearest exposure points (scanning step size) is $\Delta l = 0.2\,\mu m$, distance between the neighboring woodpile rods is $\Delta x = 1.5\,\mu m$, distance between the neighboring woodpile planes is $\Delta z = 1.0\,\mu m$, the number of woodpile layers is $m = 15$. The pulse energy measured at the entrance of the microscope was $I = 74\,nJ$. (b) Transmission and reflection spectra of the structure.

5.1 Photo-Structuring by Optical Damage in Polymers. At an appropriately chosen laser pulse intensity, exposure of transparent solids to tightly focused laser pulses leads to a micro-explosion, which obliterates the material at the center of the focal region, leaving a void, and compresses the remaining material towards the periphery of the focal region, thus creating a thin shell of densified material.[58,59] Thus, voids with densified shell are recorded. The variation in material density is followed by variation in optical density, or refractive index, n. By recording periodic arrays of separated or overlapping voids it is possible to create periodic refractive index modulation, which may lead to opening of PBG, or of incomplete PBG, which are also called photonic stop-gaps (PSG), because they create spectral optical reflectivity and transmissivity variations along a single direction (in contrast to PBG in which reflectivity and transmissivity variations are omnidirectional).

Figure 9a shows image of a top layer of a PhC with woodpile structure, acquired using a scanning optical confocal microscope in reflection. Figure 9b shows optical transmission and reflection spectra of the structure at infrared wavelengths. Woodpile structures are highly sought in photonics because of their strong tendency towards opening a complete PBG at low refractive index contrast.[60] The initial material in which woodpiles were recorded, poly(methyl methacrylate) (PMMA), is widely used in everyday life with addition of ingredients that improve its structural and chemical stability, and is known as plexiglas. For our experiments raw PMMA samples were prepared by casting chloroform solutions on cover-glass substrates and drying them in desiccator. The PhC structures were recorded by scanning the focal spot along the lines of which woodpile structure is comprised. PMMA is relatively soft and melts easily under moderate optical exposure. As a result, the recorded channels have smooth shapes. This can be seen in the image shown in Figure 9a. The photo-modified volumes inside PMMA, especially in the form of discrete voids can be used in 3D optical memory.[61] On the other hand, empty microchannels, or structures composed of microchannels can be interesting, besides photonic, for sensor applications in microfluidics.

Infrared transmission and reflection spectra of the woodpile structure recorded along the woodpile stacking direction (perpendicular to the image plane in Figure 9a) are shown in Figure 9b. Near the wavelength of $\lambda \approx 2.8\,\mu m$ spectrally matched transmissivity dip and reflectivity peak can be seen. Their spectral coincidence is a clear indication of a PSG in the structure at this wavelength along the measurement direction, as the low refractive index contrast of 1.6:1 in the PMMA:air structure does not warrant expectation of a complete omnidirectional PBG).

5.2 Photo-Structuring by Optical Damage in Glasses. Inorganic glasses of which silica glass (SiO_2) is the best example, are widely used in modern science and technology. Therefore, microstructuring of glasses by lasers is of interest to many areas of application. Inorganic glasses typically are much harder than their organic counterparts, and achieving optical damage usually requires higher instantaneous power levels. Damaging by femtosecond pulses is also more disruptive to surrounding regions of glass, and is often described as an optically induced "microexplosion" which leads to formation of a void (or a region with reduced mass and optical densities) surrounded by a thin shell of densified material. The explosion and obliteration of material also sends powerful shock-waves, which may interact with neighboring optically damaged areas, thus creating additional structural damage in the form of cracks. Thus, attempts at 3D structuring of glasses by femtosecond laser irradiation were carried out aimed at direct recording of PhC lattices in silica[21] and in a high refractive index glass.[62] However, due to the processes outlined above structural quality of the samples consisting of closely packed periodic arrays of voids was degraded, and the samples served only as a proof-of-principle demonstration of PSG formation.

A better result was achieved in attempt to record diffraction gratings consisting of hollow core lines in silica glass. Gratings recorded by linear translation of the focal spot position[63] have exhibited distinct diffracted orders and moderate random scattering. In should be noted that residual disorder remaining after recording by femtosecond pulses can be reduced significantly by thermal annealing.[64,65] The photoluminescence spectra of high purity silica damaged by tightly focused picosecond pulses looked similar to the spectra of the same silica glass damaged by femtosecond pulses and afterwards annealed.[66]

Besides thermal treatment, post processing of optically

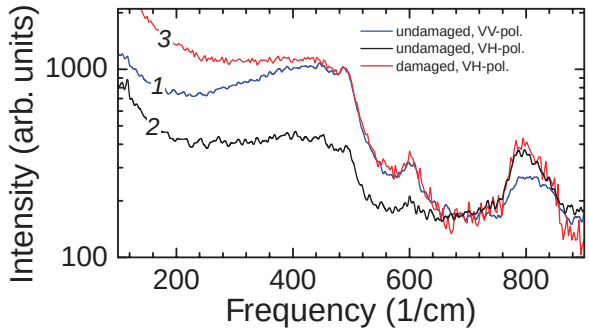

Figure 10. Raman spectra of silica glass before (1 for VH and 2 for VV polarizations) and after (3 for VH polarization) optical damaging; the notation VV means that vertical polarization was used for excitation and the same V-pol. response was monitored. Synthetic silica with OH and Cl concentrations below 100 ppm was used. Fluorescence background was subtracted from the spectra.[70]

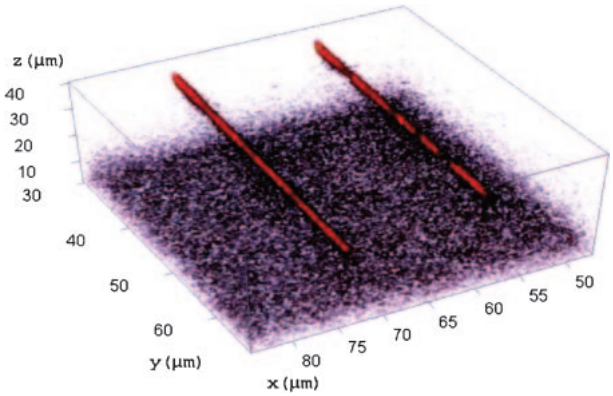

Figure 11. 3D photoluminescence map of a non-bridging oxygen hole center (NBOHC) in low-OH silica (ED-C brand from Nippon Silica Glass) detected at 650 nm and excited by an Ar-ion laser emission line at 514 nm. The linear features seen in the image were recorded by translation of the focal spot position using 800 nm/150 fs pulsed laser radiation focused by an $NA = 1.35$ objective lens.

recorded structures by chemical etching is possible. Optically modified regions of silica glass are more susceptible to etching in HF aqueous solution.[32,67,68] Channels inside high purity silica and sapphire are required for electrophoresis applications where impurity ions are hampering high-resolution measurements of DNA fragmentation via electrical screening of an applied field and due to background emission intervening with photo-detection of photoluminescence.[69] It was demonstrated that faster etching occurs in densified silica by formation of Lewis base structure in which Si–O–Si angle is decreased. The decrease of the intensity ratio of a D_1 Raman line at 495 cm^{-1} to the D_2 at 606 cm^{-1} signifies decrease of 4-ring with respect to 3-ring structures. This is illustrated in Figure 10. However, the collective network vibration band at 800 cm^{-1} is clearly not affected by optical damaging (Figure 10). These findings are consistent with the concept of a denser phase formation by increased relative weight of 3-ring structures after the dielectric breakdown at the focus.[70] The same mechanism accounts for the enhanced wet etching rates in crystalline quartz.[71]

Optically induced defects in glasses[28,64,65] can be also utilized for creation of 3D optical memory elements.[26,72–75] The defect sites possess characteristic photoluminescence (PL) lines which can be utilized for the readout of optical memory. The PL spectrum can be especially strongly modified by thermal post-annealing, which activates movement of oxygen atoms displaced by femtosecond laser irradiation.[64,65] In Figure 11 lines recorded in silica glass are clearly seen in the PL image.

5.3 Photo-Structuring of Glasses and Crystals without Optical Damage. In addition to the experiments described above, DLW is possible in glasses at intensities below the optical damage threshold, where very mild refractive index changes of the order of 10^{-4}–10^{-2} are induced.[76] Extended lines recorded in glass in this regime can be used for optical waveguiding.[77]

Even more versatile recording is possible in anisotropic photorefractive crystals like $LiNbO_3$, where single femtosecond pulses were demonstrated to induce index changes due to photovoltaic effects.[78,79] The modification is reversible, and recorded regions can be erased optically. This finding already demonstrates the basic functionality required for realization of ultrafast 3D rewritable all-optical memory elements. Optical recording of photo-darkening by femtosecond pulses has been demonstrated in chalcogenide glass.[80] The photo-darkening is rewritable and can be erased by annealing at 150–200 °C.

5.4 Photo-Structuring by Optical Damage inside Crystals. Unlike random glasses, crystals possess well-ordered crystalline lattice, which may be very sensitive to optically induced structural defects. Therefore, optical structuring of crystalline solids may be more difficult than that of glasses, and should be done at carefully chosen irradiation conditions, avoiding extensive damage. Refinement of the recorded features may be possible during post-processing, for example by wet etching.

Regions of quartz and sapphire become susceptible to wet etching after irradiation by femtosecond pulses via generation of amorphous phase of the solid, which can be afterwards removed by etching. Using such approach, discrete features having cross-sectional size in sub-micrometer range, or patterns consisting of such features were recorded and subsequently etched in HF aqueous solution.[71] Figure 12 shows topology of a region with amorphous phase recorded in quartz. Similar phenomenon was also observed in sapphire, which in crystalline phase is chemically resistant to HF.[81] The amorphous phase, which can result from irradiation by a single femtosecond pulse is, however, susceptible to etching, which allows recording with subsequent etching of arbitrary patterns in sapphire, simultaneously avoiding crack formation. Boundaries between the amorphous and crystalline phases are very sharp, with transitional region between them having thickness of about 1–2 nm.[82] The surface separating amorphous and crystalline regions corresponds to the location where shock waves are transformed into conventional acoustic waves.[46,52] Figure 13 shows the top-view of the pattern of voids recorded inside sapphire after polishing by a focused ion beam (FIB), and subsequent wet etching. The image reveals clearly the extent of amorphous region. It is noteworthy, that such sharp edge and debris free ablation was observed in GaN by focused femtosecond pulses at 400 nm central wavelength.[30]

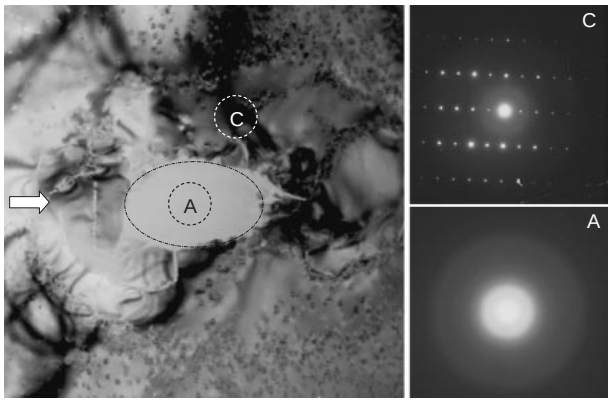

Figure 12. TEM image of a ($\langle 1\bar{1}00 \rangle$)-plane of an amorphized quartz, and electron diffraction patterns of the amorphous (A) and crystalline (C) regions. The arrow marks the direction of the pulse propagation (along the crystalline *c*-axis). The ellipsis marks the amorphous region of approximately 500 nm lateral diameter. The sample was exposed to a single 800 nm/150 fs pulse with energy at the focus of approximately 30 nJ.

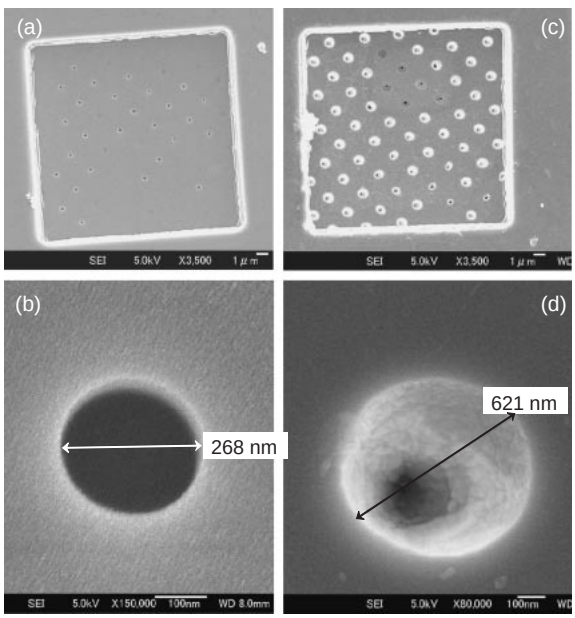

Figure 13. (a,b) Top-view SEM images of voids recorded by single 800 nm/180 fs pulses in sapphire, after FIB polishing. (c,d) The same sample after wet etching for 20 min in a 10% aqueous solution of HF. The recording pulse energy was approximately 100 nJ at the focus.

5.5 Special Cases of Direct Laser Photo-Structuring. 5.5.1 Photo-Structuring by Gauss–Bessel Beams in Glasses: Gauss–Bessel (GB) beams[83] can be generated from Gaussian beam output by standard laser systems using a conical lens, also known as axicon.[84] The key feature of GB beams is their propagation free of diffraction effects present in Gaussian beams. GB beams have a central intensity maximum (which can be also understood as an axially extended focal region) surrounded by cylindrical side lobes (see Figure 14a). Geometrical parameters of the axicon and the beam diameter define the length of the focus. During propagation the energy loss of the central maximum is constantly replenished at the expense of side lobes. Due to this circumstance GB beams are not obscured by the structural damage induced along their propagation path. Hence, multi-pulse exposure with high pulse energy can be used for the recording of elongated features, which would be impossible to achieve using Gaussian pulses without lengthy scanning of the focal point in space.[86,87]

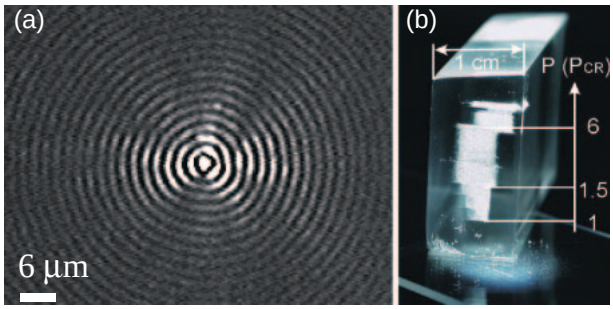

Figure 14. (a) Cross-sectional image of the Gauss–Bessel beam used in fabrication.[84] (b) The linear damage patterns recorded in a block of plexiglas (industrial-scale PMMA) at different pulse energies. The fluence per pulse which corresponded to the critical power of self-focusing, P_{CR}, was 0.9 J cm^{-2}; pulse duration 170 fs, the central wavelength was 805 nm.[85]

Figure 14b illustrates optical damage induced by a GB beam in PMMA at different energies of femtosecond laser pulses. The axial length of non-diffracting propagation of the central intensity maximum was approximately 4 mm under the conditions of the experiment. Extended damage was induced using lateral translation of the sample, as is illustrated in the figure.

5.5.2 Parallel Multi-Focal Direct Laser Photo-Structuring: Laser processing of materials with a higher practical throughput can be achieved by increasing the number of simultaneously formed focal spots in the material. To this aim a multi-lens array[88] or optical diffractive element (DOE)[80] can be used. By lateral scanning the sample or the laser beam, scanning marking, cutting, and dicing can be implemented.

5.6 Direct Photo-Polymerization in Photoresists. Photopolymerization is optically induced cross-linking of monomers and oligomers. The initial materials in which photopolymerization can be utilized for recording 3D micro- and nano-structures are usually liquid resins and solid photoresists. Below we will mostly concentrate on the latter materials. The principles enabling DLW in photoresist SU-8 were already briefly explained in Section **2**. Photoresists are usually photo-sensitized for particular wavelengths of excitation, which are typically in the ultraviolet (UV) spectral range to match eximer laser (at 308 nm) or I-line of Hg-lamp (365 nm wavelength) output. Direct monomer/oligomer absorption becomes significant at wavelengths shorter than 360 nm. Despite different mechanisms of initiation of the photo-polymerization, for a thermally activated process the cross-linking reaction can be described by the following reaction rate equation:[89]

$$\frac{d\alpha}{dt} = A \exp\left(-\frac{E_a}{RT}\right)(1-\alpha)^n, \quad (2)$$

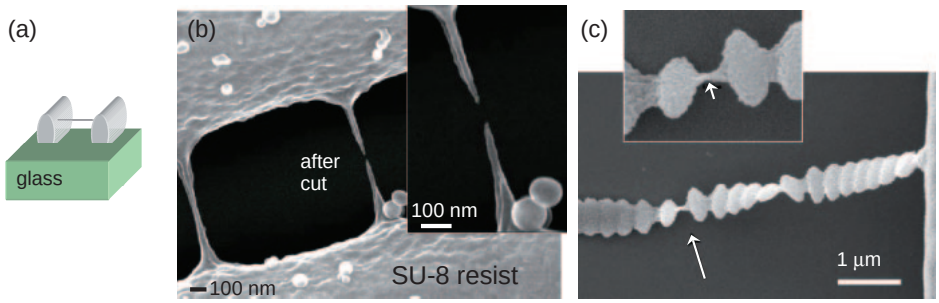

Figure 15. (a) Schematic explanation of recording with ultrahigh resolution in SU-8: at first, thin exposure lines are recorded at a low laser pulse energy (0.3 nm) a few micrometers above the substrate, and later a perpendicularly oriented set of thick lines attached to the surface of the substrate is recorded at a high pulse energy, and acts as a support for the thin lines (or nano-bridges). For both sets of lines, separation between the neighboring exposure sites was 20 nm. (b) SEM image of a nano-bridge having a width of 30 ± 10 nm at the waist, and the same bridge after cutting by a high-energy electron beam.[20] (c) Air-suspended nano-beads recorded near the surface of the glass substrate by a linear scan of the position with 250 nm step at the laser pulse energy of 0.8 nJ.

where α is the rate of reaction, E_a is the activation energy, R is the gas constant, T is the absolute temperature, n is the empirical order of reaction, and A is the empirical frequency factor. This expression shows that thermal effects play significant role along with photo-initiation via nonlinear absorption. In SU-8 photoresist the reaction order is important for photo-polymerization which proceeds with so-called chemical amplification, where several photo-acid generators are released upon cross-linking of two monomers (each having eight cross-linking sites per molecule), thus amplifying the overall propagation of polymerization. The polymerization occurs most effectively between two closely spaced exposed regions of resist, as is illustrated in the following material (see Figure 15c where a bead-like structure was fabricated when intra-pulse separation was larger than the radius of the focal spot (Figure 4)). Such propagation of polymerization occurs mostly during post-bake processing of SU-8 after exposure, and can be used to form sub-100 nm connections between larger exposed and cross-linked structures.[90]

Uniform cross-linking is essential for obtaining stress-free and mechanically stable 3D structures. To this aim the procedures of sample preparation and development are critical. For resists, removal of solvent and densification are the most important as well as post-exposure bake used to saturate the cross-linking. Well-compacted SU-8 films were used to obtain 3D photonic crystal structures without significant distortions due to polymer shrinkage.[22–24,91] Moreover, stress-free 3D structures with cross-sectional size comprising of a few tens of SU-8 constituent molecules were obtained[20] (for more details see the next Section).

5.6.1 Record-High Resolution of Photo-Polymerization in SU-8: Figure 15 presents DLW of discrete linear features in SU-8 with record-high resolution of tens of nanometers,[20] which equals to approximately ten monomer diameters (2 nm per molecule). The lateral size of recorded features, about 30 nm constitutes 1/25th of the recording laser wavelength. The resolution is mostly determined by the laser pulse energy stability during the recording. Shape and geometry of the recorded SU-8 nanorods is not altered by cutting through their middle parts with an electron beam, which indicates absence of strain.

Strain-free structures were obtained partly due to uniform cross-linking of SU-8, and partly due to the use of modified post-processing aimed at reducing the action of capillary forces during the drying of the samples. The modifications involved using non-wetting rinse agents with lower surface tension.[19] The capillary force can be eliminated by using supercritical drying, but practical use of this approach is difficult. The 3D photo-polymerized structures can be coated by Au, Ag, or Cu for plasmonic applications were currently the structures made by planar electron beam lithography and lift-off procedures are utilized where large area patterning and high uniformity are required.[92–94]

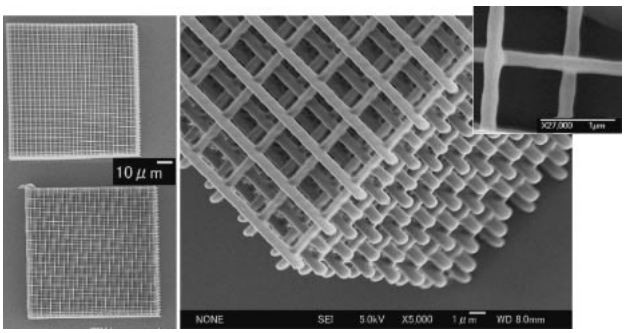

Figure 16. Typical woodpile structures recorded by DLW in SU-8. The inset shows the smallest lateral width of woodpile rods at which extended 3D structure can still be retrieved after development and rinse.

5.6.2 Photonic Crystal Structures with Woodpile and Spiral Architectures in SU-8: The improvements described above have allowed fabrication by DLW of extended photonic crystal structures with woodpile and spiral architectures in SU-8.[22–24,91,95]

Figure 16 shows typical woodpile structures in SU-8 which are self-supporting and open to infiltration by other materials for subsequent enhancement of their refractive index contrast. Structures composed of linear features with lateral diameters of 200 nm and above are mechanically stable and show negligible shrinkage, unlike their counterparts fabricated in liquid resins.[96] For woodpile rods with smaller lateral diameter, achieving mechanical stability of 3D structures often becomes an issue, as retrieval of structures after wet development leads to destructive action of capillary forces. These circumstances

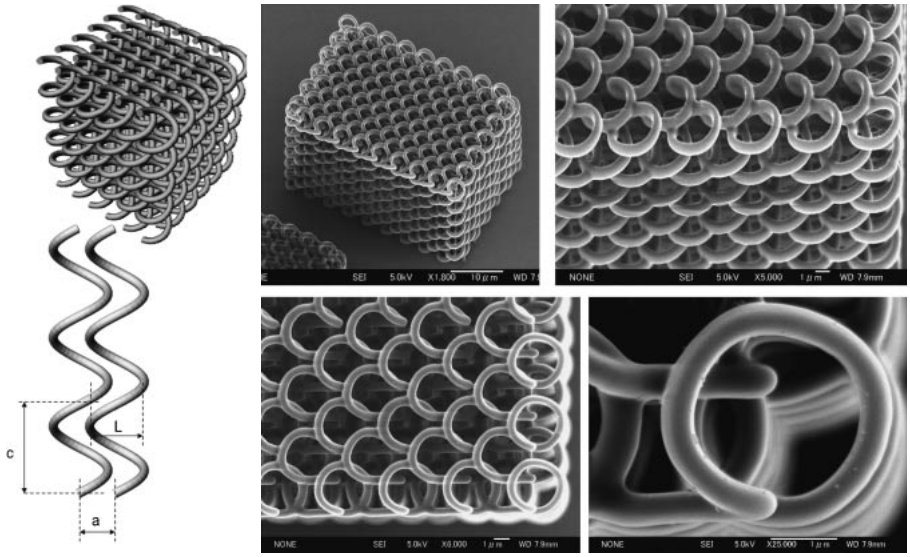

Figure 17. (Left) schematic explanation of parameters of the spiral structure, (middle and right) SEM images of a spiral structure recorded in SU-8 by DLW at optimal exposure conditions.

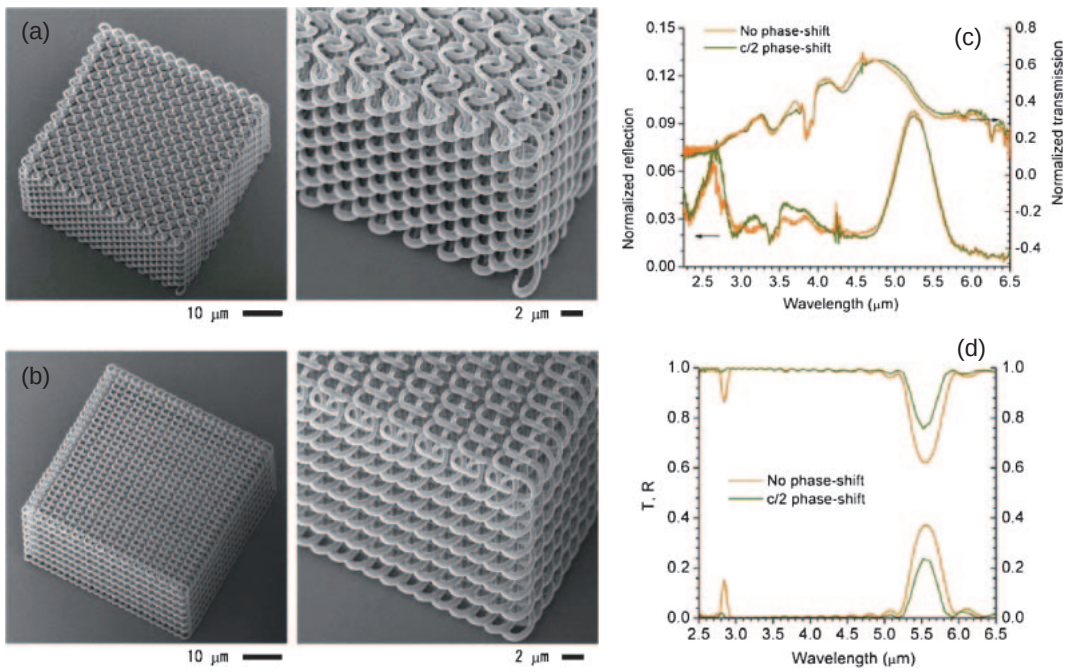

Figure 18. SEM images of 3D PhC structures with spiral architecture in SU-8, (a) with a half-period (π or $c/2$) phase shift between the neighboring spirals, (b) without the phase shift. (c) The measured transmission and reflection spectra of these structures, and (d) the same spectra obtain from numerical simulations.

must be addressed, for example by reducing the action of capillary forces.

Examination of optical properties of the woodpile structures (not shown) has revealed both fundamental (lowest frequency) and higher-order PSG in these structures. Since second and higher-order PSGs are very sensitive to refractive index changes of the environment, these structures can be adapted for sensor applications, i.e., when immersed into liquid or gas they will reveal subtle changes in their composition by spectral transmission/reflection changes at the PSG wavelength.

Figure 17 illustrates schematically the topology and main structural parameters of 3D circular spiral structures as well as shows examples of spiral structures recorded by DLW in SU-8. Figures 18a and 18b show more examples of the spiral structures together with their optical properties at infrared wavelengths in Figures 18c and 18d. These structures exhibit both fundamental and second-order PSGs, which indicate their high structural and optical quality and homogeneity. Notice, that in Figure 18a the neighboring spirals have mutual phase shifts of π. This feature is important for optimization of the optical properties of spiral structures. Currently DLW is the only fabrication technique capable of delivering phase-shifted spiral structures.

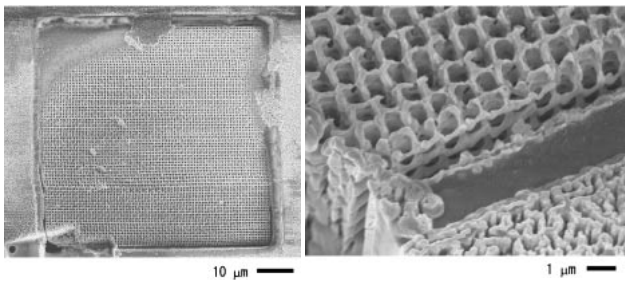

Figure 19. PhC structure with a square-spiral architecture initially fabricated by DLW in SU-8, and subsequently transformed into a Si structure by double infiltration. The SEM images feature top-view (left) and perspective-view of a structure cut by a focused-ion beam (right).[97]

5.6.3 Infiltration of SU-8 Structures by Other Materials: Due to the low index contrast between SU-8 and the surrounding air (1.6 to 1), omnidirectional PBG can not open in SU-8 periodic structures, which nevertheless can be highly suitable as templates for subsequent infiltration by other materials having a higher refractive index.

Figure 19 shows the PhC structure where initial square-spiral SU-8 template was replaced by Si using double-infiltration technique.[98] The top surface of the woodpile seen in the SEM image in Figure 19 corresponds to the top of the cover glass substrate, etched-out after Si growth. Replication of PhC structure in Si was confirmed by SEM observation of FIB cut of the structure.

Figure 20 gives an example of a woodpile structure coated by a film of nickel using electroless coating. Metallic coating of periodic dielectric structures enables fabrication of metallo-dielectric photonic crystals (MDPhC).[99] The coating was carried out as follows. First, the SU-8 templates were sensitized in a solution of $SnCl_2$, then activated in solution of $PdCl_2$ and subjected to electroless plating of Ni in solution of $NiCl_2$, NH_4Cl, NaH_2PO_2, and NH_4OH with pH 9.2, at a temperature of $t = 40\,^{\circ}C$. As Figure 20 illustrates, areas coated by Ni are predominantly smooth and grainless, with some partially or fully "bare" uncoated SU-8 areas and some Ni debris filling gaps between the rods. Such defects are unwanted as they degrade optical quality of the samples. Despite these defects, the samples reveal clear signatures of photonic zero-order gap (characteristic exclusive to metallic PhCs, and a first-order gap near the wavelength of 3.3 μ, in qualitative agreement with theoretical finite-difference time-domain (FDTD) calculations, as is illustrated in the Figure.

6. Photo-Structuring by Multiple-Beam Interference Technique

Practical implementation of fabrication by multiple-beam interference was described earlier in Section **3.2**. Here, we will describe structures obtained using this flexible and versatile method of microstructuring.

In general, the interference field intensity distribution $I(\mathbf{r})$ can be expressed superposition of plane coherent waves:

$$I(\mathbf{r}) = \sum_{n,m} \mathbf{E_n} e^{-i(\mathbf{k_n}\cdot r+\delta_n)} \cdot \mathbf{E_m^*} e^{i(\mathbf{k_m}\cdot r+\delta_m)}, \quad (3)$$

where $\mathbf{E}$ is the complex electric field vector, $\mathbf{r}$ is the radius vector, $\mathbf{k}$ is the wavevector, and $n = m$ represents the number of interfering beams. The phases of beams are given by $\delta_{n,m} = 0$. Simple 2D and 3D periodic intensity patterns obtained for three and four interfering beams, calculated using eq 3, were already shown in Figure 3.

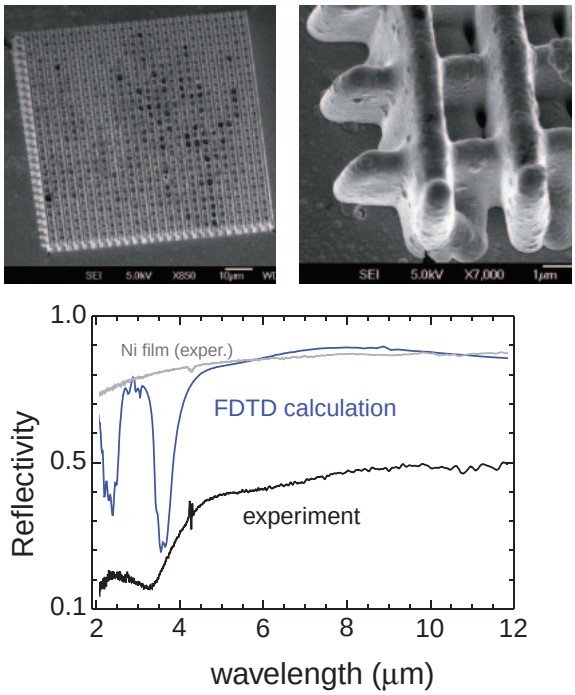

Figure 20. Woodpile structure coated by Ni film (top), and its measured and theoretically calculated optical reflectivity spectra at infrared wavelengths (bottom). The rod-to-rod distance was 3 μm and layer-to-layer was 1 μm.

Illustration of a more complex 3D pattern is given in Figure 21. The configuration of interfering beams is shown schematically in Figure 21a, and involves four beams, like in one of the examples in Figure 3. Symmetric four-beam arrangement results in a body-centered-tetragonal (bct) 3D lattice.[41] However, if two of the beams are asymmetrically located as in Figure 21a, the asymmetry leads to a noticeable tilt of the interference pattern, which is visible in the calculated result shown in the same panel. Figure 21b shows SEM images of the structure fabricated in SU-8 at a pulse energy of 20 μJ after exposure for several tens of seconds at a 1 kHz laser repetition rate. The total diameter of the fabricated structure was 0.8 mm, although near the edges, where exposure dose was lower and connectivity between the cross-linked regions was poorer, significant disorder in the form of peeling layers resulted. Near the center of the sample the recorded pattern resembles closely that following from theoretical calculations.

Another example of complex patterning by multiple-beam interference field is shown in Figure 22. Here, eight beams, arranged according to the scheme shown in Figure 22a are used to create a very complex interference pattern, whose calculated intensity distribution is depicted in Figure 22b. The crucial feature of this layout, not obvious from the scheme, is phase difference of $\pi/2$ between the two nearest beams. As can be seen, the resulting pattern forms a 2D quasi-periodic lattice, and can be used in fabrication of quasi-periodic photonic struc-

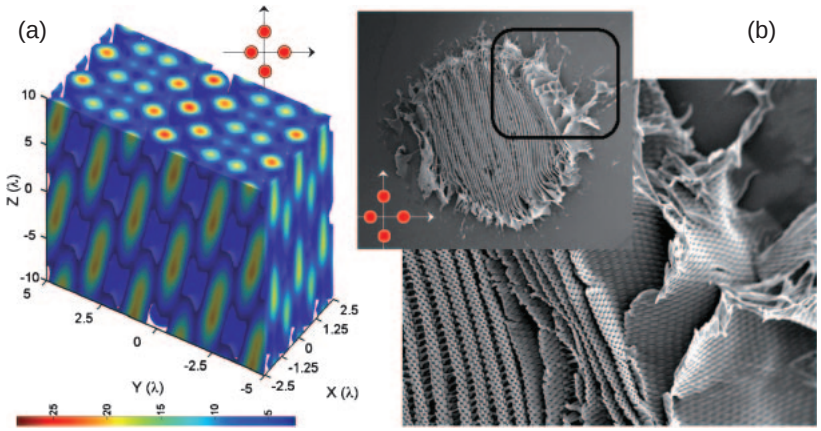

Figure 21. (a) Four-beam asymmetric alignment, as seen on the plane of the beam selector, and its calculated intensity distribution,[41] (b) SEM images of the pattern fabricated in SU-8 using such alignment.

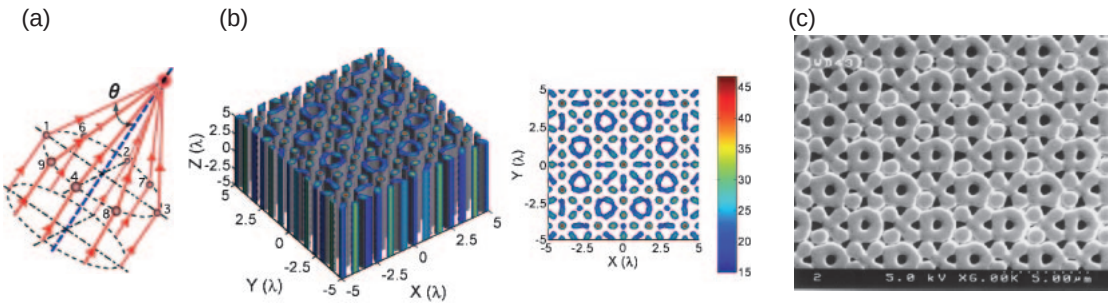

Figure 22. (a) Eight-beam arrangement with phases of two neighboring beams shifted by an amount of $\pi/2$, (b) the calculated interference pattern, (c) top-view SEM image of the structure recorded in SU-8.[100]

tures. Figure 22c shows top-view SEM image of the structure fabricated in SU-8 under conditions similar to those used for the fabrication of the previously discussed sample. As can be seen, the recorded pattern resembles closely the theoretical expectation.

More examples of various 2D and 3D patterns fabricated by multiple-beam interference in polymers and As_2S_3 glass can be found in our earlier publications.[39,41,42,80,101] Just like the structures recorded in SU-8 by DLW, these structures can be infiltrated by high refractive index materials or metals, and are potentially suitable as photonic band gap (or stop gap) materials. Other possible areas of application for such structures include biotechnology, for example scaffolds composed of bio-compatible photo-polymers for cell culture incubation.

7. Mechanism of Light-Matter Interaction: Ultra-Fast Laser Pulses

Since thermal conductivity over the dimensions of the focal volume is negligible on a sub-1 ps time scale, laser microfabrication becomes independent of pulse duration (a change of the diffusional $\propto \sqrt{\tau_p}$ dependence of the dielectric breakdown on pulse duration τ_p). It is sometimes erroneously called non-thermal process since there is a small heat affected zone (HAZ) around the laser fabricated region (Figure 7). Despite the change of $\sqrt{\tau_p}$ dependence, the energy delivered during the pulse into the focal volume turns into thermal excitation on a later stage after the pulse has passed throughout the focal region. Then, the thermal processes becomes important and can even generate high pressure and micro-explosion[46,52] when energy delivered to the electron sub-system is returned to the atoms/ion. The material is turned into fully ionized plasma by dielectric an optical breakdown switching light-matter into light-plasma interaction. The optical properties of plasma determine this interaction.

7.1 Dielectric Function of Ionized Solid. The optical parameters of matter upon ionization are defined via a dielectric function, $\mathcal{E} = \mathcal{E}_1 + i\mathcal{E}_2$. The plasma can be properly described in the Drude approximation when the ions are considered as a neutralizing background:[102]

$$\mathcal{E}_1 = 1 - \frac{\omega_p^2}{\omega^2 + \nu_{eff}^2}, \tag{4}$$

$$\mathcal{E}_2 = \frac{\omega_p^2}{\omega^2 + \nu_{eff}^2}\frac{\nu_{eff}}{\omega}, \tag{5}$$

where the ν_{eff} is the effective electron–ion collision frequency. By assuming $\nu_{eff} \approx \omega_p$, the real and imaginary parts of dielectric function and the refractive index $N \equiv \sqrt{\mathcal{E}} = n + i\kappa$ are expressed:

$$\mathcal{E}_1 \simeq \frac{\omega^2}{\omega_p^2}; \mathcal{E}_2 \simeq \frac{\omega_p}{\omega}\left(1 + \frac{\omega^2}{\omega_p^2}\right)^{-1}; n \simeq k = \sqrt{\frac{\mathcal{E}_2}{2}}. \tag{6}$$

Assuming single ionization early in the laser pulse $n_e \approx n_a \approx 10^{23}\,cm^{-3}$, one obtains $\omega_p^2 \simeq 3.74 \times 10^{32}\,s^{-2}$. Then, the imaginary part of the dielectric function equals $\mathcal{E}_2 \simeq 8.2$, therefore real and imaginary parts of the refractive index are the same, $n \approx k \simeq 2.02$. The absorption length is described by $l_s =$

$c/(\omega k)$, where c is speed of light, $k = 2\pi/\lambda_0$ is the wavevector. For normal incidence the absorption, A, depends on the reflection, R ($A + R = 1$), as $A = 1 - R \simeq 4n/((n^2 + 1) + n^2) \simeq 0.61$.

For laser pulse energy effectively absorbed in a volume that is significantly smaller than the focal volume, $V_{abs} = l_s \times \pi r_{1/2}^2$ (here $r_{1/2}$ is the waist of beam at focus at FWHM and l_s is the Rayleigh length). The optical breakdown converts transparent dielectric into a metal-like medium reducing the energy deposition volume by two orders of magnitude and correspondingly massively increasing the absorbed energy density. The absorbed energy upon equilibration creates high density and temperature plasma which generates shock wave and emits X-rays via bremsstrahlung.

7.2 Absorption by Plasma. The maximum plasma concentration to be reached by optical excitation in continuous wave irradiation is defined by a plasma frequency, which is determined by the critical concentration of free carriers, N_c, by $\omega_p^2 = N_c e^2/\varepsilon_0 m_e$, where m_e is the effective mass of electron (in mass units), e is the electron charge, and ε_0 vacuum permeability. When this frequency is equal to that of laser irradiation, the material reflects the laser light (the reflection coefficient $R \to 1$). This is correct for homogeneous plasma and at a normal incidence. However, in the case on a non-homogeneous plasma and in the presence of a longitudinal light field component, as it is for an oblique incidence of a p-polarized light (at a tight focusing), the light energy can be further delivered to the plasma region by absorption. This is called a resonant absorption widely used in experiments on laser-induced nuclear fusion where longitudinal energy transfer from light to target is implemented. The resonant absorption is particularly important for tightly focused (by the use a microscope objective lens of $NA > 0.2$) laser pulses, since the polarization is not uniform at the focal region[103] and the longitudinal component is present. This is a possibility to reach electron concentrations, at which the stability of lattice is undermined, typically at $N_e \geq 10^{22}\,\mathrm{cm}^{-3}$ [104] and, so called, a non-thermal melting of material can be observed at time duration much shorter than 1 ps.[105]

Paraxial approximation is not adequate to describe the beam trace and focal geometry for a tightly focused beam/pulse. At the exact focus, at the waist of a Gaussian beam, there is an E-field, which is parallel to the beam propagation. Hence, for intensity:

$$E_l^2 = T(E_i \sin\alpha)^2, \tag{7}$$

where T is the transmission coefficient of the lens, and the half-angle of the focusing cone is $\alpha = 16.3^\circ$ for $NA = 0.28$ with focus in air ($n = 1$), E_i is the incident field strength, and E_l is the longitudinal field component at focus responsible for resonant absorption and, correspondingly, to higher electron densities.

In order to separate concentration from temperature dependencies in plasma absorption, the absorption coefficient, α, can be presented in such a form:[106]

$$\alpha = \frac{N_0^2}{\sqrt{1 - N_0}}\alpha_c, \tag{8}$$

where $N_0 = N_e/N_c$, $N_{e,c}$ is the electron density and critical plasma density, respectively, and the only temperature-dependent plasma absorption coefficient, α_c, is given by:[106]

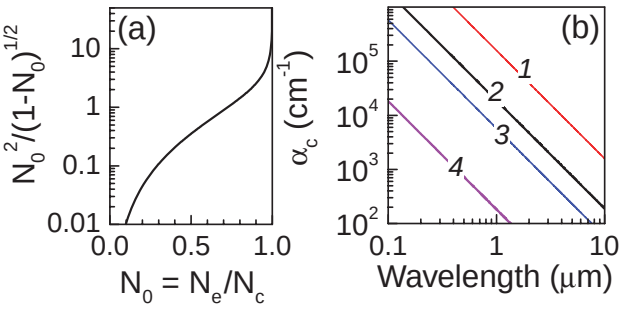

Figure 23. Wavelength dependence of plasma absorption coefficient $\alpha = [N_0^2/\sqrt{1 - N_0}] \times \alpha_c$ (eq 8). (a) Electron density, N_e, dependence of the factor $N_0^2/\sqrt{1 - N_0}$. (b) Wavelength dependence of absorption coefficient, α_c (eq 9), at the critical electron density N_c for the different electron temperatures of 1000 °C or 0.11 eV (1), 5000 °C or 0.454 eV (2), 1 eV (3), and 10 eV (4).

$$\alpha_c \simeq \frac{9}{8c}\sqrt{\frac{2\pi}{m_e}}\frac{Ze^4 N_c}{(kT_e)^{3/2}}, \tag{9}$$

where Z is the ionization number (here we are considering $Z = 1$). Equations 8 and 9 are plotted in Figure 23. It shows that the most effective absorption is taking place at the locations where plasma density is approaching critical and that the plasma is getting more transparent at high temperatures.

7.3 Self-Focusing and Filamentation. When pulse power exceeds the critical value of self-focusing, P_{cr}, the pulse will collapse to a singularity (blowup) point after propagating a self-focusing distance, L_{sf}. The value of P_{cr} is determined by the non-linear part of refractive index, n_2, ($n = n_0 + n_2 I$):[107]

$$P_{cr} = \frac{2\lambda^2}{8\pi n_0 n_2}. \tag{10}$$

The Gaussian beam under above condition self-focuses after propagating along the distance, L_{sf}:[108]

$$L_{sf} = \frac{2\pi n_0 r_{min}^2}{\lambda} \Big/ \sqrt{\frac{P_0}{P_{cr}} - 1}. \tag{11}$$

For example, in a fused silica ($n_0 = 1.45$; $n_2 = 3.54 \times 10^{-16}\,\mathrm{cm}^2\,\mathrm{W}^{-1}$) and for $\lambda = 0.8\,\mu\mathrm{m}$, the critical power comprises $\approx$1 MW. Assuming $P_0 = 100 P_{cr}$ and $r_{min} \approx 10\lambda$, one estimates the self-focusing distance to be 31.6λ.

Self-focusing of femtosecond pulses with presence of strong ionization is currently actively investigated in relation to pulse filamentation phenomenon.[109] There are no analytical solutions available in this case, especially, for tight focusing. Extended focal regions with filament-like structures and spherical breakdown regions were observed even at focusing with a $NA = 1.35$ objective lens inside silica.[110]

The ponderomotive force acting on an electron at irradiance of tens-of-PW/cm^2 at the focus or during pulse self-focusing also leads to disruption of targeted pulse delivery required for well-controlled X-ray generation. The intensity distribution due to ponderomotive effect leads to filamentation via a favorable refractive index modulation as discussed below. The on-

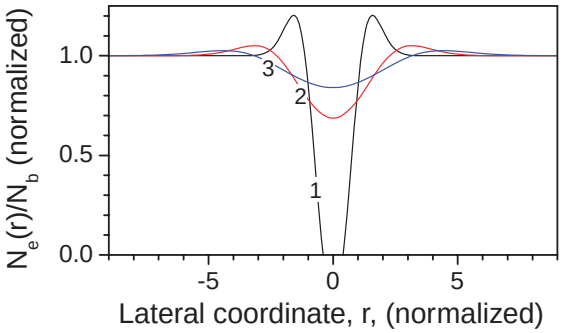

Figure 24. Visualization of eq 14: the normalized electron density vs. the normalized lateral coordinate r for the waist of $r_0 = 2.5$ (1), 5 (2), and 7 (3). The Gaussian intensity distribution of the form $I(r) = I_0 \exp(-4 \ln 2(r/r_0)^2)$ was taken for calculations; r_0 is the FWHM radius (waist) of the beam/pulse, r is the cylindrical coordinate.

axis lateral refractive index in the presence of Kerr and free electron contributions is given by:[111]

$$n(r) = n_0 + n_2 I(r) - \frac{\omega_p(r)^2}{2\omega^2}, \tag{12}$$

where, n_0 is the unperturbed refractive index, n_2 is the nonlinear refractive index [$\mathrm{cm^2\,W^{-1}}$], $\omega = kc$ is the laser frequency, and $\omega_p(r)$ is the radially dependent plasma frequency given by:

$$\omega_p(r) = \sqrt{\frac{N_e(r)e^2}{\varepsilon_0 m_e}}, \tag{13}$$

where the lateral distribution of the electron density is (in cylindrical coordinates):[112]

$$\frac{N_e(r)}{N_b} = 1 + \left(\frac{d^2}{dr^2} + \frac{1}{r}\frac{d}{dr}\right)\sqrt{1 + I(r)^2}, \tag{14}$$

where N_b is the background electron density. Figure 24 shows effective electron density profiles at the focus at different irradiance/intensity. When a non physical (negative) value of N_e/N_b is obtained it corresponds to electron depletion from the center of laser beam/pulse by ponderomotive force and is called electron cavitation. The decrease of electron density creates a region of increased refractive index where light can be guided. The ponderomotive effect distorts the energy delivery to the aimed focal location at high intensity.

7.4 Optically Induced Dielectric Breakdown. The nature of optical breakdown is still under active investigation despite bulk of experimental and theoretical work accomplished. An exact quantitative description of the dielectric breakdown and subsequent material modification is not currently available, though qualitative scenarios are well understood in terms of multi-photon and avalanche ionization and subsequent high temperature and pressure modification of surrounding material. The time-resolved measurements of dielectric function dynamics together with material movement are highly necessary. It is a challenging task requiring tight focusing and time-resolved X-ray measurements applied simultaneously.

Material excitation leading to breakdown is discussed theoretically along few scenarios. The most accepted view is that multi-photon and avalanche ionization creates a critical electron density via an inter-coupled sequential process of electron multiplication. Once the critical density is attained an instantaneous ionization (occurring within few optical cycles) of the entire focal volume ensue. The multi-photon absorption is most important in providing seeding electrons, while the avalanche makes the most effective multiplication. It is noteworthy, that the absorption takes place at the skin depth of ionized volume once the dielectric breakdown occurs. The skin depth is <100 nm and the light-field is effectively shielded (exponential decay) inside the region of dielectric breakdown, which makes the multi-photon process of electron multiplication highly ineffective. However, the avalanche still provides an effective mechanism, since it is linearly dependent on intensity and is effective within the skin depth.

The tight focusing creates conditions when approximately one optical cycle is present at the waist region. At the irradiance $\approx 10^{13}\,\mathrm{W\,cm^{-2}}$ the breakdown, a full ionization of the focal volume, effectively occurs in few optical cycles. For experimental detection of the breakdown by optical plasma emission, it appears as an instant step-like event.[113] This apparent instantaneous dielectric-to-metal transition was explained as analogous to the Mott transition:[113] an effective increase of outer electron orbitals due to strong electric light field causes a loss of correlation between the ions and electrons since the orbitals become overlapping. This randomization creates uncorrelated electrons at certain strength of E-field (irradiance) in a step-like fashion. This qualitative explanation is similar to that of a conductivity jump in Bi under compression when the electrons switch into metallic uncorrelated state due to mechanical compression.

A step-like switch of dielectric into a metallic state has been proposed as a bandgap collapse model[103,114] which explains the breakdown as a collective response of the pulse-affected volume of crystals. The physical mechanism is the Bragg-type reflections of oscillating electrons at boundaries of the first Brillouin zone. The flattening of the bands at high intensity causes a sharp increase in the probability of electronic transitions eventually causing breakdown. The theoretically expected scaling of the dielectric breakdown on the bandgap energy was indeed observed in fluorides. Table 1 shows the experimentally determined light-induced damage threshold (LIDT).[115] The fact of LIDT was judged by statistical analysis of an optical contrast change (see, Ref. 44 for details). It is well established that for fluorides the bandgap can be expressed in the universal form:[116]

$$E_g = \chi_g \frac{\hbar^2}{m} d_{nn}^2, \tag{15}$$

where d_{nn} is the distance to the nearest neighbor ($d_{nn} = 2.36$, 2.70, and 2.33 Å in CaF_2, BaF_2, and CdF_2, respectively), m is electron mass, $\hbar$ is Plank's constant, and $\chi_g \simeq 9.1$ is a compound-dependent parameter. This equation represents the calculations of the bandgap structure by the linear combinations of atomic orbitals (LCAO) taking into account only nearest neighbors. As one can see, the product $Const = \frac{1}{E_g} \times d_{nn}^2$ is constant. Interestingly, we found that for several fluorides the product $LIDT \times d^2$ was indeed constant, where d represents the average distance between atoms (Table 1). This product can be used as a figure of merit for evaluation whether the LIDT scales with E_g as $LIDT \approx \frac{1}{E_g}$. The figure $LIDT \times d^2$

Table 1. The Intrinsic Light-Induced Damage Threshold (LIDT) for a Single 220 fs 800 nm Pulse at 10 μm Depth in Crystalline Fluorides[a)]

Material	LIDT /nJ	Density ρ /g cm^{-3}	Molar mass M /g	Separation[b)] $d = \sqrt[3]{n_a}$ /Å	Figure of merit $LIDT \times d^2$	Refractive[d)] index at $\lambda = 800$ nm
CaF_2	89	3.18	78.08	3.44	1055	1.435
SrF_2	80	4.24	125.62	3.67	1075	1.439(@550 nm)
BaF_2	68	4.83	175.33	3.92	1045	1.470
MgF_2[c)]	105	3.16	62.31	3.20	1076	1.39(@560 nm)

a) Focusing was made by a $NA = 1.3$ objective lens at 100× magnification. b) Separation represents the average distance between neighboring atoms; $n_a = \rho N_A/M$ is the atomic number density with N_A being the Avogadro number. c) MgF_2 is birefringent; the given value of refractive index is an average. d) Refractive indexes were taken from catalogues of Crystran Ltd., UK and Almaz Optics, Inc., USA.

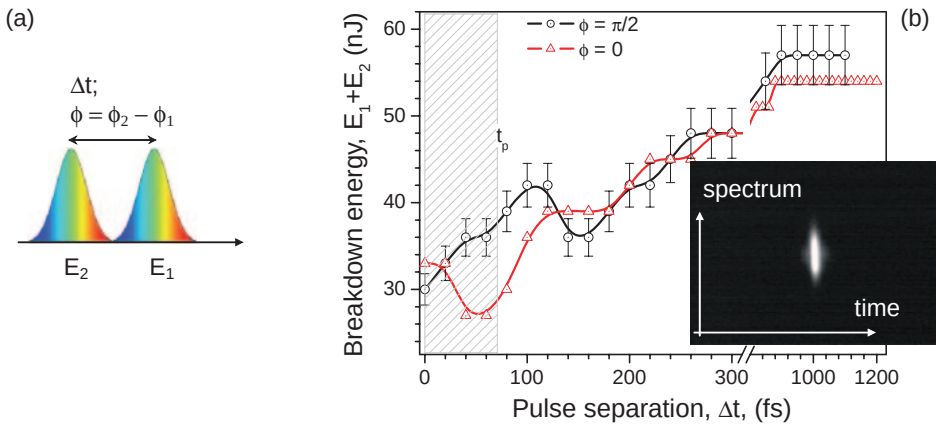

Figure 25. (a) Schematics of two pulses of energy $E_1 = E_2$ produced by Dazzler modulator[49] with controlled chirp, energy, temporal separation, and phase. (b) The cumulative energy $E_1 + E_2$ at which the dielectric breakdown took place was measured at different pulse separations and at different relative phases between the two pulses.[49] The inset shows the time-spectrum map (measured by frequency resolved optical gating (FROG)[50]) of the $t_p = 50$ fs pulse at the laser output. The pulse was split into two pulselets by Dazzler.

was constant in fluorides with high fidelity (<5% distribution). Since, the bandgap of most transparent dielectric crystals and glasses is in the UV and VUV spectral region where measurements require specialized vacuum UV-spectrometry, the breakdown measurement can provide a reliable estimate of the bandgap energy.

A tunneling mechanism has also been proposed recently[117] based on the experimental results of surface ablation[118] by femtosecond pulses at 400 nm. It should be noted, that the values of threshold irradiance were overestimated since the power meter used was not calibrated for measurements at low repetition rate. However, the relative ablation thresholds determined in the same measurement showed an experimental dependence $Th \sim E_g^{\gamma}$ with $\gamma = 3.1$, very close to the expected value $\gamma = 3$ for the tunneling breakdown (E_g is the effective bandgap energy). Usually, it is not possible to make a clear distinction between the two: pure tunneling and multi-photon multiplication of electrons, since the dielectric breakdown used in most experiments and practical applications occurs at the irradiance where both mechanisms are present. The Keldysh parameter $\gamma = \sqrt{2mJ}\omega/(eE_0)$ (valid when $J/(\hbar\omega) > 1$) draws the distinction between the two mechanisms, here e and m are the charge and mass of an electron, E_0 is the amplitude of electrical field, and J is the ionisation potential.[119] For the ionization potential $J = 8$ eV for a silica and irradiance $I = 4 \times 10^{14}$ W cm^{-2} at 800 nm wavelength one could find $\gamma \simeq 0.5$. When $\gamma \ll 1$ (a condition called the strong field and small frequency) the multi-photon ionization is described by the tunneling formula. At $\gamma \gg 1$ (a condition called the low field and high frequency) the multi-photon ionization dominates.

Finally, models of bandgap re-normalization and coherent phonons should be considered at the dielectric breakdown based on recent studies.[120] The importance of coherent light-matter interaction is illustrated in Figure 25, where the cumulative energy of a two-pulse dielectric breakdown threshold, $E_1 + E_2$, vs. time separation, Δt, is plotted at two different relative phases, ϕ, between the two pulses.[49] The pulses were produced by a Dazzler (Femtolite, Inc.) phase modulator, had the same polarization, and were introduced coaxially into the microscope and delivered into a sapphire sample at tight focusing. Clear dependence of the breakdown on the relative phases was observed (see, Figure 25 at small Δt). The dielectric breakdown is related to various phenomenon, e.g., chirp, tilt of the pulse,[121] X-ray, white light continuum (WLC), or third harmonic generation,[76] and filamentation.[86,109] All these optically nonlinear phenomena occur at approximately 1–10 TW cm^{-2} irradiance. The short wavelength emission of the

breakdown plasma delivers energy along a laser pulse propagation into a depth considerably larger than the absorption length in metals.[122] This principle allowed the achievement of ultra-deep structuring. Also, the IR part of the electron emission of plasma provides an effective light source for photo-polymerization of resins which absorb well at 2–3 μm wavelengths.[53] The experimental research field of light-matter interaction when sub-ps pulses are used is currently very active and theoretical description of light-matter interaction in various complex geometries are expected to be established in near future.

8. Laser Manipulation of Nano-/Micro-Objects: Principles

Laser trapping and manipulation has been developed into a solid branch of modern science and technology. Laser tweezers can be seen as a tool to apply force or transfer momentum to (nano-)microscopic objects. Here, we consider an object to be "nano" when its dimensions are smaller that 100 nm.[126] Laser tweezers are applied to get insight into a sub-micrometer world, to measure forces of biomachinery with anticipated new applications in science and technology. There are two principles to manufacturing on the molecular scale:[127] self-assembly of structures from basic chemical building blocks the biomimetic or a "bottom up" approach and assembly by manipulating components with much larger devices a "top-down" approach. The former is considered to be ideal through which nanotechnology will ultimately be implemented, however, the latter approach is more readily achievable using current technology. Laser micro-manipulation is already serving as a research tool for the "top-down"approach.

8.1 The Optical Gradient Force. Most frequently light-material interaction is considered in terms of energy transfer. Light can transfer an impulse as well, that causes mechanical, i.e. ponderomotive action of light. This was demonstrated theoretically by Maxwell in the middle of the 19th century and experimentally by Lebedev in 1901.[128] A single photon carries an impulse $p \equiv \text{Energy/speed} = \hbar\omega/c = \hbar k$, where $\hbar$ is the Plank constant, ω, c, k are angular frequency, speed and wave vector of light in vacuum, respectively.

Despite theoretical complexity the calculations of laser trapping force are feasible when a laser trapping beam is focused to its diffraction limited size.[129] For a highly focused beam the relevant length scale for interaction is the spot size ω and not the particle diameter $2R$. This reduces interference effects and renders this approach applicable to particles of any size. The force due to the interaction of the electromagnetic field with a particle is given by the integral of the Maxwell stress tensor on its surface. The following derivations follow Ref. 129, where practical formulas were demonstrated to describe well experimental data.

For isotropic dielectrics which are not strongly polarized (i.e. the dielectric susceptibility $\chi \ll 1$) and for a linear response the dipole density relates to the electric field by $P = \chi E \simeq \chi E_0$, where E_0 is the unperturbed electric field. Then, the dipole interaction energy of the particle, W, is defined by the integral:

$$W = -\alpha \int I_0 \, \mathrm{d}V, \tag{16}$$

where $I_0 = \varepsilon_0 E_0^2/(8\pi)$ is the volume energy density of the light and $\alpha = \varepsilon_\mathrm{p}/\varepsilon_0 - 1$ accounts for the relative difference of the dielectric constants of the particle, ε_p and the surrounding medium, ε_0. The optical gradient force is simply given by the change of W in response to a change of particle's coordinates.

It is assumed that the localized electromagnetic field near the focal point is a three-dimensional Gaussian with axial symmetry and its energy density is given by:

$$I(\rho, z) = I_0 \mathrm{e}^{-\frac{\rho^2}{2w^2} - \frac{z^2}{2w^2\epsilon^2}}, \tag{17}$$

where w and $w\epsilon$ are the dimensions of the beam waist in the transverse and axial dimensions, respectively, and the eccentricity is ϵ.

First, an isotropic potential well with $\epsilon = 1$ is considered. Taking the gradient of the dipole energy (eq 16) of the Gaussian beam (eq 17), the central restoring force is defined as:

$$F(r) = \frac{\partial W(r)}{\partial r} = \alpha I_0 w^2 \cdot 4\pi \mathrm{e}^{-\frac{a^2+u^2}{2}} (au \cosh au - \sinh au), \tag{18}$$

where $a = R/w$ and $u = r/w$ is the normalized radius and coordinate, respectively. For small particles $R \ll w$, Equation 18 reduces to the product of the particle volume and the gradient of the beam intensity,

$$F(u) \simeq \alpha I_0 w^2 \frac{4\pi}{3} a^3 u \mathrm{e}^{-u^2/2}. \tag{19}$$

Near the equilibrium position, $r = 0$, the restoring force is harmonic and increases to its peak value at the position of maximal gradient at $r = w$. An illustration of the eqs 18 and 19 is shown in Figure 26, where typical experimental conditions for laser trapping biological objects (with low refractive index) were implemented.[130]

In most practical situations, focused beams are not isotropic having eccentricity $\epsilon \geq 3$. The central restoring force can be calculated and it was shown that analytical expressions are available when the spherical particle is approximated by a cube of the same volume.[129] The resulting radial force curve for a general eccentricity, ϵ, is

$$\frac{F_\rho(\rho)}{\alpha I_0 w^2} = A(\epsilon) \mathrm{e}^{-\frac{u^2}{2}} \sinh(a_\mathrm{c} u). \tag{20}$$

The anisotropy effects are embedded in a prefactor $A(\epsilon)$

$$A(\epsilon) = 4\pi\epsilon \mathrm{Erf}\left(\frac{b_\mathrm{c}}{\sqrt{2}}\right) \mathrm{Erf}\left(\frac{b_\mathrm{c}}{\sqrt{2}\epsilon}\right) \mathrm{e}^{-\frac{a_\mathrm{c}^2}{2}}, \tag{21}$$

where $a_\mathrm{c} = b_\mathrm{c} = \frac{R}{w}\sqrt[3]{\pi/6}$, and $u = \rho/w$. The axial force curve is similarly defined

$$\frac{F_z(z)}{\alpha I_0 w^2} = A_z(\epsilon) \mathrm{e}^{-\frac{u_z^2}{2}} \sinh(a_\mathrm{c} u_z), \quad \text{where } u_z = z/(w\epsilon), \tag{22}$$

$$A_z(\epsilon) = 4\pi\epsilon \mathrm{Erf}^2\left(\frac{b_\mathrm{c}}{\sqrt{2}}\right) \mathrm{e}^{-\frac{a_\mathrm{c}^2}{2\epsilon^2}}. \tag{23}$$

In the vicinity of equilibrium position the laser-trapped particle can be considered as a harmonic oscillator with Hookian linear response. For this region it is useful to define the force constant by the curvature of the potential. For a Gaussian beam the resulting force constant $\kappa_{z,\rho}$ for a general eccentricity can be calculated analytically for a sphere as $\partial^2 W/\partial x^2 (x = 0)$

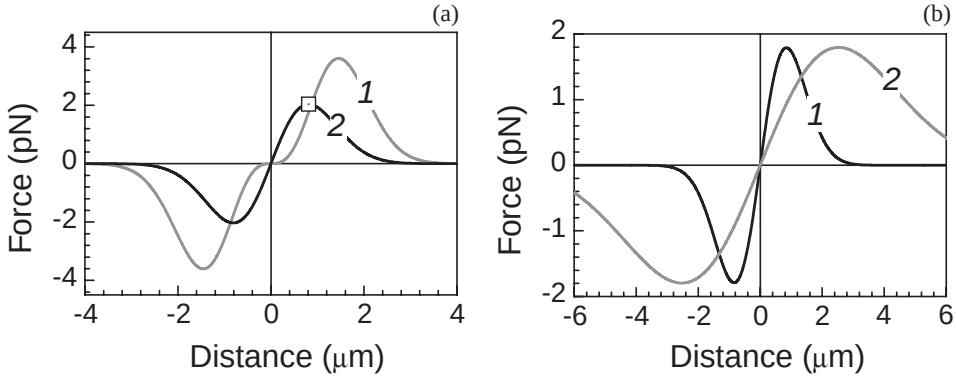

Figure 26. (a) Optical gradient force of isotropic potential well ($\epsilon = 1$). Curve 1 plotted according to eq 18 and curve 2 by eq 19. The lateral radius of a focal spot (the waist) is defined by the numerical aperture, $NA = 0.8$, of objective lens and the laser wavelength, $\lambda = 1.064\,\mu m$, according to $w \equiv 0.61\lambda/NA \simeq 0.81\,\mu m$. The refractive indexes of the laser-trapped particle and its environment (water) were $\sqrt{\varepsilon_p} = 1.370$ and $\sqrt{\varepsilon_0} = 1.326$, respectively, and the laser trapping power was 0.7 W or in terms of volume energy density $I_0 = 7.69 \times 10^{-3}\,J\,cm^{-3}$. The square marks the maximum value of the gradient force $F_m = \alpha I_0 w^2(4\pi/3\sqrt{e})a^3$. (b) Radial (curve 1) and axial (2) gradient forces exerted on a cube-shaped particle trapped in a prolate ($\epsilon = 3$) focus (curve 1 is plotted by eqs 20 and 21, and curve 2 by eqs 22 and 23). Experimental conditions are the same as for (a).[130]

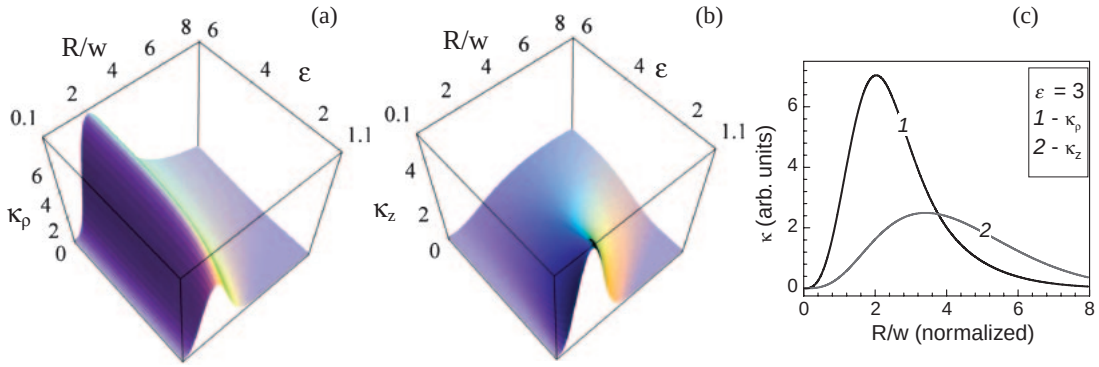

Figure 27. Radial/transverse (a) and axial/longitudinal (b) force constants of a laser trap calculated for a prolate ($\epsilon > 1$) focus. Force constants are plotted as $\kappa_{\rho,z}/(\alpha I_0 w)$ according to eqs 24 and 25. R/w is the normalized radius of the particle, w is the lateral waist of the beam, and ϵ is the eccentricity of focus. (c) Axial and lateral force constants vs. normalized particle radius for a prolate focal spot with $\epsilon = 3$ (typical for the most of experiments).[130]

(here $x \equiv \rho$; z):[131]

$$\kappa_\rho = \alpha I_0 w \cdot e^{-\frac{a^2}{2}} \frac{\pi\epsilon}{\xi^3}\left(-2a\epsilon\xi e^{-\frac{a^2\xi^2}{2\epsilon^2}} + \sqrt{2\pi}(\epsilon^2 + a^2\xi^2)\mathrm{Erf}\left(\frac{a\xi}{\sqrt{2}\epsilon}\right)\right), \quad (24)$$

$$\kappa_z = \alpha I_0 w \cdot \frac{2\pi}{\xi^3}\left(2a\xi^2 e^{-\frac{a^2}{2\epsilon^2}} - \sqrt{2\pi}\epsilon e^{-\frac{a^2}{2}}\mathrm{Erf}\left(\frac{a\xi}{\sqrt{2}\epsilon}\right)\right), \quad (25)$$

where $\xi = \sqrt{1-\epsilon^2}$. The force acting on a particle is then given by $F_{\rho,z} = \kappa_{\rho,z} w$. Figure 27 shows the dependence of the force constants on a particle size and geometry of focal spot (a prolate $\epsilon > 1$ case is considered as it is in a real experiment).

The approach presented above[129,131] describes reliably the spatial extent of a focal region by analysis of laser trapping of a smectic liquid crystal droplet[132] as well as the trapping force of a nematic liquid crystal microsphere.[130]

8.2 Transfer of Angular Momentum from Laser Beam to Particle. The angular momentum carried by light can be characterized by the "spin" angular momentum associated with circular polarization[133] and the "orbital" angular momentum associated with the spatial distribution of the wave.[134] Each photon of Gaussian circularly polarized beam has an angular momentum $\sigma\hbar$, where $\sigma = \pm 1$ left-handed and right-handed circular polarization, respectively. The Laguerre–Gaussian (LG) beam has, additionally, an angular dependence of $\exp(-il\phi)$, where l is the azimuthal mode index or charge. The LG modes can be seen as eigenmodes of the angular-momentum operator L_z and thus carry an orbital angular momentum $l\hbar$ ($l = \pm 1$).[134] The total angular momentum carried by a photon of LG beam is $(l + \sigma)\hbar$. When this is multiplied by the number of photons absorbed per second, the same resulting torque is obtained as that found using electromagnetic theory. The torque due to the angular momentum of the light on a particle that absorbs power P is $\Gamma = P(l + \sigma)/\omega$.

The momentum and angular momentum of light can be transferred to an object not only by light absorption, but by refraction as well (by a change of propagation direction). The reflection from or propagation through a birefringent object can effectively transfer momentum and angular momentum to that object. This principle can be used in development of optically driven micro-mechanical devices.

8.3 Prototypes of Optically Driven Micro-Devices. The method of torque application to a micro-object constitutes the principle of an optically driven micro-device. The element torque is expressed as $\mathrm{d}\boldsymbol{\Gamma} = \mathbf{r} \times \mathrm{d}\mathbf{F}$, where $\mathrm{d}\mathbf{F}$ is the element force and $\mathbf{r}$ is the vector from the pivot point to the location where force is applied. The equation of motion which links torque $\boldsymbol{\Gamma}$ exerted on the object with its angular velocity $\boldsymbol{\Omega}$ and moment of inertia I is then

$$\boldsymbol{\Gamma} = I\frac{\mathrm{d}\boldsymbol{\Omega}}{\mathrm{d}t} + D\boldsymbol{\Omega}, \tag{26}$$

where D is the damping factor (the drag coefficient for the rotational movement). For a spinning sphere $D = 8\pi\eta r^3$ and $D = \frac{32}{3}\eta r^3$ for a disk of radius r in a medium of viscosity η. In the steady state the time derivative in eq 26 drops out and the terminal angular velocity is proportional to the torque divided by the damping factor, which is highly dependent on object's shape and the properties of the environment where the object moves.

Gauthier[135] evaluated numerically the torque acting on an object shaped as a four-wing windmill trapped by single-beam laser tweezers. The derivation was based on ray optics and was evaluated for an object of 13 μm span. Calculations well explained the earlier reported experimental results on spinning of such an object in a laser trap made by using a linearly polarized lowest order Gaussian (TEM_{00}) beam.[136] The rotation at 0.37 Hz was observed for laser power of 80 mW. The direction of spinning can be reversed by inverting optical contrast $n_{\mathrm{rel}} = n_{\mathrm{s}}/n_{\mathrm{m}}$, which is the ratio of refractive index of sample, n_{s}, and that of surrounding media, n_{m}.[135] If $n_{\mathrm{rel}} < 1$ the object is pushed out of the focus along the direction of light propagation and the windmill must be supported for a sustainable rotation. The theory was extended to deal with the different wing shape, which has an inclination of the front surface.[137] It predicts control over the direction of rotation via an illumination spot size.

Another approach was introduced for the fabrication of optically driven rotor.[138] Two polystyrene beads of 2 and 0.94 μm in diameter were linked via avidin-biotin binding. The smaller bead was half-coated with gold/palladium. This geometry allowed the harvest of the gradient pressure of laser trap made by a focused linearly polarized beam and to convert it into a spin torque. An average rotation frequency of 2.6 Hz was observed at 29 mW laser power ($\Gamma \simeq 10^{-19}$ Nm). Even higher rotation frequencies of 10 Hz were reported for 3–4 μm windmill-type structure at 20 mW.[139] The structure was photopolymerized by laser scanning and even the engaged cogwheel structure was made and driven by single beam laser trap.

9. Laser Manipulation of Liquid Crystals

Liquid crystals are among materials of highest optical nonlinearity, however, since it is related to molecular reorientation it is a slow μs–ms process. When liquid crystals are prepared as spherical micro-particles by dispersing them in water, the droplets can be optically trapped and manipulated by laser tweezers.[140] The birefringent particles can be controlled by polarization of impinging light: their orientation follows the linear polarization of laser tweezers or, in the case of circularly polarized light, are put in constant spinning.[141–143] This can be used as a viscosimetry probe of micro-environment revealing changes of reordering at water–liquid crystal boundaries induced by starting and stoping of the droplet.[130,144]

Molecular ordering defines local refractive index and birefringence. It is possible to induce re-alignment of liquid crystal molecules inside adroplet and by doing this to optically induce birefringence.[132,145,146] Then, the droplet can be laser actuated or spined by changing the laser trapping power of a linearly polarized beam or by setting up circularly polarized laser tweezers, respectively. Such mechanical movement of a droplet due to a laser irradiance which modified its optical properties can be considered as a manifestation of a nonlinear optical effect used to laser manipulate a microscopic object.[145]

9.1 Laser Tweezers Acting on Birefringent Particles. Light-induced rotation of absorbing microscopic particles by transfer of angular momentum from light to the material has its shortcomings for practical applications due to overheating and unwanted axial forces, limiting the achievable rotation rates to a, typically, few hertz. Higher rotation frequencies can be obtained when birefringent particles are used as it was demonstrated in the case of ground calcite particles[147] and nematic liquid crystal (LC) droplets[141,142] laser manipulated in water.

Let us consider an elliptically polarized laser beam incident on a particle (the following description is based on Ref. 147). Elliptically polarized light can be described by $\mathbf{E} = E_0 \mathrm{e}^{i\omega t}\cos\phi\cdot\mathbf{x} + iE_0 e^{i\omega t}\sin\phi\cdot\mathbf{y}$, where ω is the angular frequency and E is the electric field of light and x with y are Cartesian coordinates defining the lateral spot size. Here, ϕ describes the degree of ellipticity of the light ($\phi = 0; \pi/2$ indicates plane-polarized and $\phi = \pi/4$ circularly polarized light).

To calculate change in angular momentum of light after the passage through birefringent material, the incident elliptically polarized light is first expressed in terms of components parallel and perpendicular to the optical axis of the material:

$$\begin{aligned}\mathbf{E} = {} & E_0 \mathrm{e}^{i\omega t}(\cos\phi\cos\theta - i\sin\phi\sin\theta)\mathbf{i} \\ & + E_0 \mathrm{e}^{i\omega t}(\cos\phi\sin\theta + i\sin\phi\cos\theta)\mathbf{j}),\end{aligned} \tag{27}$$

where θ is the angle between the fast axis of the quarter-wave plate producing the elliptically polarized light and the optical axis of birefringent material. The phase shift due to passing through a thickness d with refractive index n is kdn, where $k = 2\pi/\lambda$ is the free space wavenumber. So, the emergent light field will be:

$$\begin{aligned}\mathbf{E} = {} & E_0 \mathrm{e}^{i\omega t}\mathrm{e}^{ikdn_{\mathrm{e}}}(\cos\phi\cos\theta - i\sin\phi\sin\theta)\mathbf{i} \\ & + E_0 \mathrm{e}^{i\omega t}\mathrm{e}^{ikdn_{\mathrm{o}}}(\cos\phi\sin\theta + i\sin\phi\cos\theta)\mathbf{j}),\end{aligned} \tag{28}$$

where $n_{\mathrm{e,o}}$ are the refractive indexes of extraordinary and ordinary rays, respectively. The angular momentum of a plane electromagnetic wave is defined as $\mathbf{J} = (\epsilon/(2i\omega))\int \mathrm{d}^3 r \mathbf{E}^* \mathbf{E}$, where $\mathbf{E}^*$ marks the complex conjugate of electric field vector $\mathbf{E}$ and integration is made over all spatial elements $\mathrm{d}^3 r$. The changes in the angular momentum of the light cause a reaction torque per unit area on the thickness d of material:

$$\begin{aligned}\tau = {} & -\frac{\epsilon}{2\omega}E_0^2 \sin kd(n_0 - n_{\mathrm{e}})\cos 2\phi \sin 2\theta \\ & + \frac{\epsilon}{2\omega}E_0^2(1 - \cos kd(n_0 - n_{\mathrm{e}}))\sin 2\phi.\end{aligned} \tag{29}$$

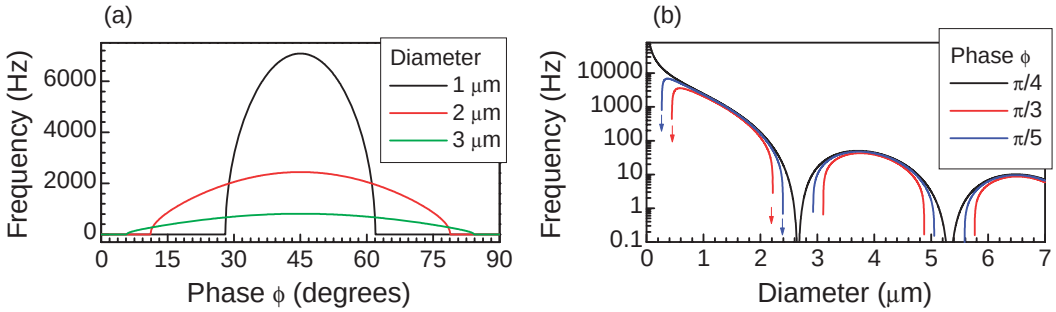

Figure 28. Frequency dependencies of birefringent micro-particle put into rotation by transfer of light's angular momentum to a particle (visualization of eq 30). (a) Rotation frequency vs. ellipticity of light. (b) Rotation frequency vs. particle size. Calculated for a birefringent spherical particle of diameter/thickness d, laser power $P = 0.4$ W, and refractive index difference $\Delta n \equiv n_0 - n_e = 0.2$. The viscosity of surrounding medium, the water, was taken $\eta = 1.002 \times 10^{-3}$ Pa•s.

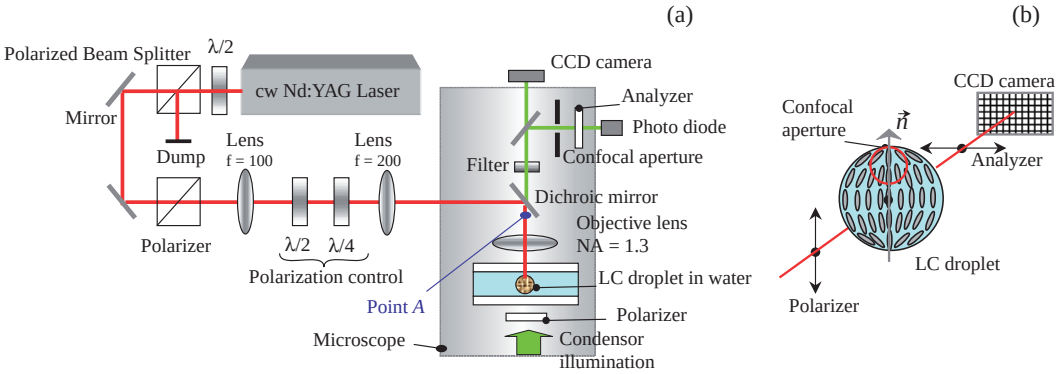

Figure 29. (a) Setup for optical manipulation of liquid crystal droplets. The eccentricity ϵ of the laser beam is determined at point A. (b) Geometry of optical switching experiment. **n** in the director.

The first term in eq 29 is the torque due to the plane-polarized component of elliptically polarized light or, we can call it, the alignment torque. While the second term of eq 29 is due to the change in polarization caused by passage through a birefringent media. For plane-polarized light, $\phi = 0$ or $\pi/2$, the torque on the particle is proportional to $\sin 2\theta$. The particle will experience torque as long as $\theta \neq 0$, and will be at equilibrium when the fast axis of the crystal is aligned with the plane polarization ($\theta = 0$).

For a steady state spinning particle the torque exerted on particle by light (eq 29) is counter balanced by the environment's drag torque (eq 26) according to $\tau = D\Omega = D \times 2\pi f$. The frequency of particle's rotation, f, for a trapping power P and optical frequency ω is:

$$f(d,\phi) = \frac{P\sqrt{(1-\cos kd(n_0-n_e))^2 \sin^2 2\phi - \sin^2 kd(n_0-n_e)\cos^2 2\phi}}{2\pi\omega D}. \quad (30)$$

Figure 28 shows the calculated frequency dependencies of a birefringent spherical particle according to eq 30. The fastest spinning is observed when particle thickness corresponds to a $\lambda/2$-plate. This is the reason for the periodic dependence of frequency vs. particle size (Figure 28b). Every local maximum in the rotation frequency obeys the dependence on particle size $f \propto r^{-3}$, which follows from Stokes law (Figure 28b). The rotation of birefringent calcite micro-particles of ca. 6 μm radius was demonstrated[147] at 50 mW laser trapping, but the rotation frequencies were only few hertz. The large viscous drag due to an irregular particle shape was the main obstacle to achieve higher speed. The frequency limit for the smaller particles is actually imposed by the size of the laser spot, which at its diffraction limit approaches diameter $1.22\lambda/NA$ (NA is the numerical aperture of the objective lens, typically $NA = 0.8$–1.3) and due to increased light scattering, which decreases the efficiency of torque transfer from laser beam to a particle (the efficiency factor is discussed in Section **9.2**).

9.2 Rotation of Liquid Crystal Droplets. Typical setup to perform all-optical switching experiments by laser trapped droplets of liquid crystals (LCs) is shown in Figure 29.[141,143,148,149] A combined angular tuning of $\lambda/2$ and $\lambda/4$ plates allows precise control of the polarization of the laser beam at the focus (the polarization is analyzed by a Nikol prism at point A before the objective lens). The laser trapping force is calibrated by measuring the speed at which the laser trapped micro-sphere of radius, r, is released in liquid of known viscosity, η, using Stokes' law.[150] Typically, a 50 mW laser power corresponded to 10–30 pN trapping force.[150]

Nematic liquid crystal is self-organized into droplets of 0.5–4 μm diameter when dispersed in water. Most droplets possess a polar-like structure of molecular arrangement due

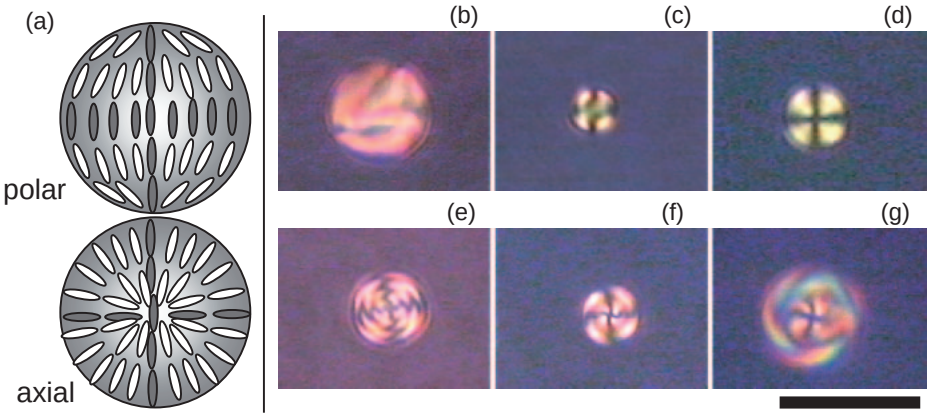

Figure 30. (a) The simplest polar and radial molecular alignments of a nematic LC. The darker regions correspond to the Maltese cross figure observed in the cross-polarized setup. Images in cross-polarized observation of the laser trapped different LC droplets. (b) Typical image of large LC droplets, which usually have complex internal molecular structure. (c) nematic E-44 LC, (d) smectic SmC_{A^*} CS-4001 LC, (e) smectic SmC CS-1017 LC, (f) SmC CS-1029 LC, and (g) SmC CS-1023 LC. Scale bar, 10 µm.

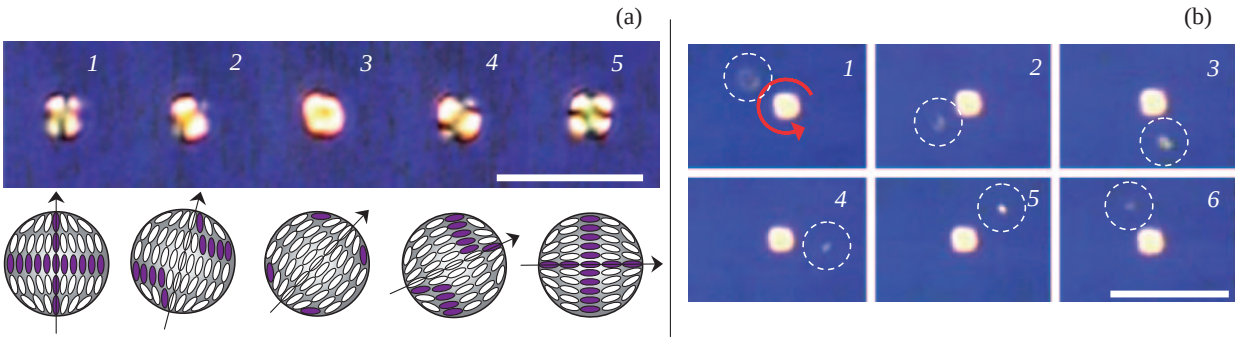

Figure 31. Alignment (a) and rotation (b) of nematic liquid crystal E-44 droplets in water by polarization control of light. Schematic presentation of the molecular order inside a droplet is shown on the bottom (a). The director of the droplet is following the polarization of the light (1⟶5(a)). Spinning of a droplet by a beam of circularly polarized light was evidenced by the drag of a neighboring free-floating droplet (enclosed in a dashed circle(b)). Time interval between images 1⟶6 was ca. 30 ms (b). Scale bars, 10 µm.

to the so-called anchoring effect (shown schematically in Figure 30a). The molecules of the outer regions tend to be oriented along the surface of the droplet, while the inner regions tend to sustain their bulk-like orientation. This brings about the final polar-like structure of the droplet. However, some of LC droplets have a radial or irregular structure. When imaged through a pair of cross-polarized Nikol prisms, the iconoscopic picture, so-called "Maltese cross," is observed (Figure 30). The dark regions correspond to those areas where the passing light was least scattered, and vice versa, the brightest ones where the scattering was strongest. However, the distinction between the polar and radial structures is not straightforward from such an image. As is schematically shown in Figure 30a, both molecular alignments cause similar iconoscopic image. Further distinction on the internal molecular arrangement can be done on the basis of the response of a LC droplet to laser manipulation. The underlying mechanism of the response can be understood in terms of a birefringence of the droplet outlined above in Section **8.2**. If the structure of LC droplet is radial the birefringence is negligible and the droplet will not respond to a change of polarization of the trapping beam. The birefringent particles with a polar internal structure can be efficiently laser manipulated. Even if at the first moment, when laser trap is set at the droplet, its orientation is such that it is seen as radial (top view on a polar structure looks like a radial one), such an orientation is metastable and typically within a few tens-of-milliseconds the LC droplets of 2–5 µm are re-oriented to a stable trapping with the director of the droplet aligned perpendicularly to the propagation of trapping laser beam.

Particles with a polar orientation can be easily laser manipulated (orientated to a preset angle or spined) by polarization control of a laser beam as shown in Figure 31.[141,142] The different iconoscopic images in Figure 31a correspond to different orientation of a laser trapped LC droplet. Once the polarization of a laser trap is set to circular, nematic LC droplet begins to spin (Figure 31b). The spinning is evidenced viscous drag of the nearby floating LC droplet.

The frequency of optical switching can be measured experimentally by a setup shown in Figure 29, where the frequency of optical transmission modulation is four-fold that of droplet's rotation:

$$f_{\mathrm{opt}} = \nu \cdot 4 f(d, \phi), \tag{31}$$

here the factor ν accounts for the efficiency of torque transfer from light to a droplet and $f(d, \phi)$ is given by eq 30.

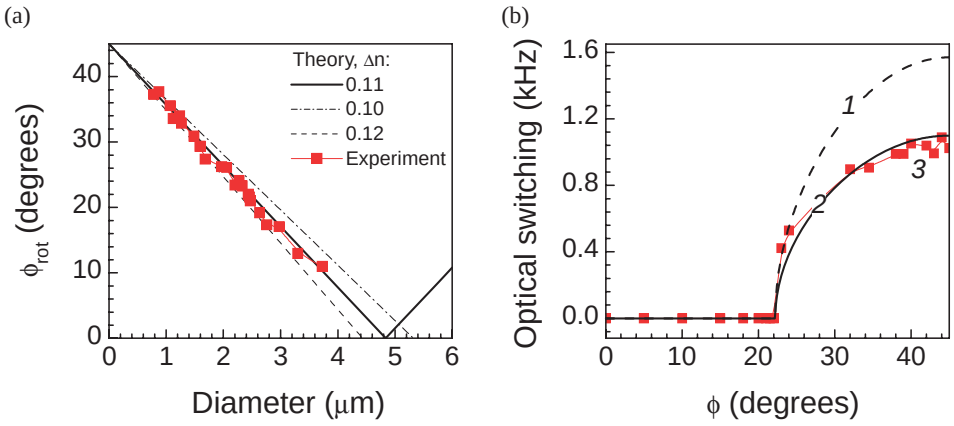

Figure 32. (a) Determination of effective refractive index change of a birefringent spherical particle (eq 32). (b) Frequency of optical switching by a laser manipulated liquid crystal droplet vs. the ellipticity of light, ϕ (eqs 30 and 31). The ellipticity phase angle ϕ is related to the experimentally measured eccentricity of the laser beam by $\phi = \tan^{-1}\epsilon$, where $\epsilon = \sqrt{P_{min}/P_{max}}$ is defined by the ratio of minimum and maximum laser power passed through Nikol polarizer (the angular dependence of the passed laser power is measured). The diameter of droplet was $d = 2.45 \pm 0.08\,\mu m$, the laser power at focal point was 198 mW, and the environment water.[143]

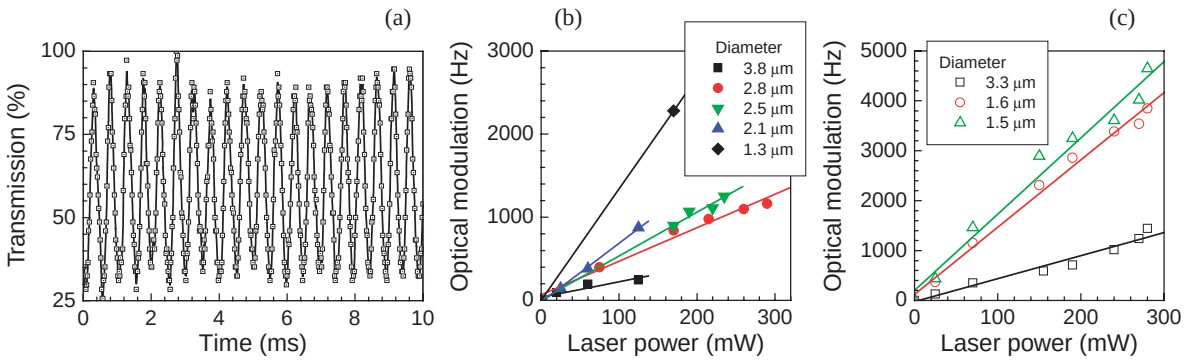

Figure 33. (a) All-optical switching (modulation of transmission) by a rotating nematic LC droplet of 1.8 μm diameter. Droplet was laser trapped by circularly polarized 1064 nm illumination of 0.6 W in pure water. (b) Dependence of the frequency of optical transmission modulation on the trapping laser power for nematic E-44 LC droplets of different sizes. LC droplets were laser manipulated in D_2O (heavy water was used to exclude any absorption at 1064 nm). (c) Same as (b) but the rotation was carried out in a mixture of D_2O:surfactant TWEEN20 (500:1).

Typical refractive index contrast for the ordinary and extraordinary rays in a birefrigent nematic LC is $\Delta n = 0.2$ ($\Delta n = 0.256$ for E-44 nematic LC). When nematic LC has a spherical shape its molecular arrangement changes and the effective refractive index contrast Δn needs to be established experimentally. This can be done by measuring the ellipticity of a laser beam (angle ϕ) at which birefringent particle starts to spin. This can be found from eq 29 for the case when the alignment torque (first term of equation) is maximum and the total torque is zero. This is when

$$\phi_{rot} = [\pm m\pi \mp kd\Delta n]/4, \text{ where } m = 1, 3, 5, \ldots . \quad (32)$$

The best fit of experimentally measured ϕ_{rot} gives the value of effective refractive index, $\Delta n = 0.11$ with a precision better than 10^{-2} (Figure 32a). With this established value of Δn the experimentally observed dependence of optical switching frequency f_{opt} on the degree of ellipticity of a laser beam can be fitted by eq 31 as shown in Figure 32b, where the curve 1 is plotted for an ideal 100% torque transfer from laser light to a spherical droplet. The experimental data of f_{opt} can be fitted by eq 31 with efficiency factor $\nu = 0.7$ (curve 2 in Figure 32b). It is noteworthy, that a better fit of experimental data at the maximum rotation speed can be achieved with $\nu = 0.58$,[130] however, then the theoretical and experimental angles of the onset of rotation, ϕ_{rot}, become different. This difference can be discussed as a result of an actual surface drag (kind of change of static into dynamic friction) during starting and stopping of the spinning.[130]

High frequency and contrast of optical switching (Figure 33a) can be further improved by decreasing viscous drag of a rotating LC droplet or/and by increasing the laser power as required by eq 30. In order to avoid absorption at elevated laser powers heavy water, D_2O, is a preferable environment for a laser manipulation, since the absorption at ca. 1 μm is almost by an order of magnitude lower than that in H_2O. Typical experimental results of the dependence of optical switching on laser power are summarized in Figure 33b. Addition of a surfactant TWEEN20 increased the frequency of LC droplet rotation (Figure 33c). As can be seen, the revolution frequencies of the LC droplet over 1 kHz (4 kHz of optical

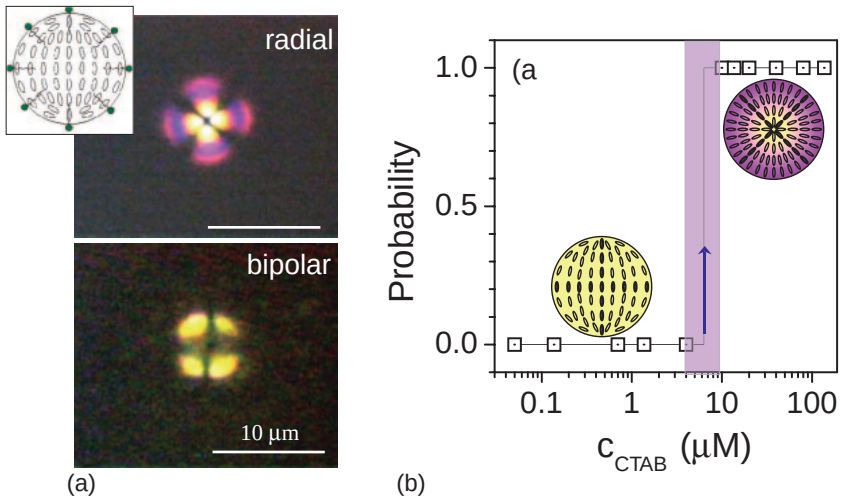

Figure 34. (a) Optical polariscope images of 5CB liquid crystal droplet having a radial (top) and polar (bottom) structural compositions, respectively. Inset schematically show the effect of surface covered by surfactant CTAB molecules. (b) Probability of a 5CB droplet having radial internal alignment versus the concentration of cationic surfactant CTAB. The region from 4 to 10 μM is transitional, in which smaller particles are bipolar and the larger are radial.[151]

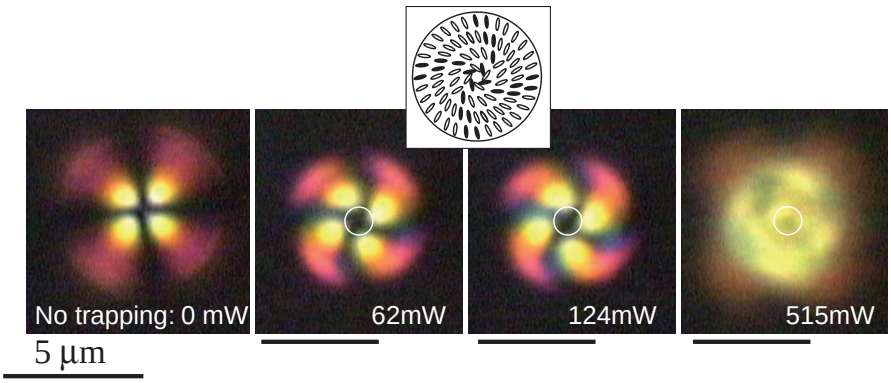

Figure 35. Optical polariscope images of a 5CB droplet at different laser power of circularly polarized laser tweezers. The inset shows schematic molecular alignment inside the droplet. The central circle marks the approximate diameter of the focal spot.

switching rate) can be reached in the case of 0.3 W laser trapping power and surfactant-modified 1.5 μm diameter droplets. This power level is approximately half of that required to achieve such a frequency in pure D_2O.[142] However, at larger surfactant concentrations and at high laser power the rotating particle stops. This phenomenon can be explained by a change of surface tension over the LC droplet which in turn changes the anchoring energy at a pre-surface area of the droplet as illustrated in Figure 34.[151] Such internal rearrangement of LC might prove useful for the application of monitoring the ambience of a laser-manipulated particle via control of the LC droplet rotation, which is governed by the interaction at the droplet's surface–liquid interface.

Apart from structural changes of the internal structure of liquid crystal droplets by surface tension effects discussed above, optically induced internal molecular reordering is also possible by laser trapping of droplets with linearly and circularly polarized laser beam.[145,146,151] Such molecular reordering is illustrated in Figure 35 taking place inside laser-trapped radial 5CB liquid crystal droplet at increasing laser power of circularly polarized tweezers. The radial droplet is optically isotropic and its spinning is not possible due to absence of birefringence. However, with increasing laser power the molecular alignment changes and the induced birefringence causes onset of rotation (right-side image in Figure 35). This is manifestation of ponderomotive action of optical nonlinearity.

9.3 Texture Control of Liquid Crystals via Optical Alignment. When the optical alignment of LC droplets cannot be controlled by changing the polarization of the light due to their internal close-to-radial or irregular structure, other phenomenon can be observed. Namely, an internal molecular re-orientation takes place on a time scale of tens-of-minutes (Figure 36). Since LC materials usually do not absorb at 1 μm the structural changes observed are caused by dipole re-orientation rather than by absorption-induced heating. There is another indirect proof of the non-thermal character of such an internal re-structuring of LC droplets. Most LC materials undergo the phase transition from the ordered to isotropic state, which is optically isotropic, too, at ca. 100 °C, (for E-44 at 100 °C, CS-1017 at 68.7 °C, CS-1023 at 94 °C, CS-1029 at 92 °C, and CS-4001 at 86.6 °C). Once isotropic, the droplet do not rotate under circular polarization. However, for nematic LC droplets partly ordered into a polar structure, the experiments did not show any changes in the rotation frequency over

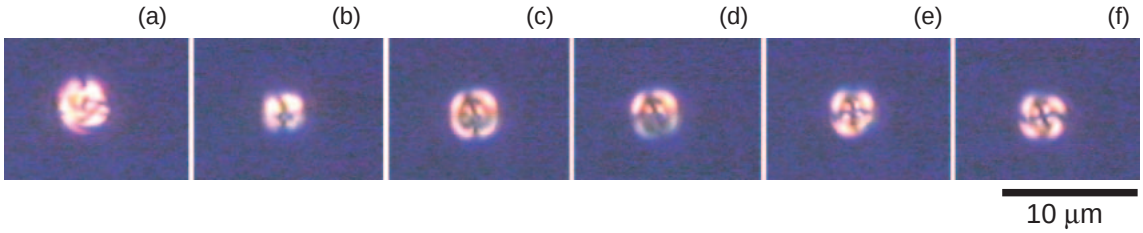

Figure 36. Texture manipulation of liquid crystal. Rearrangement of internal structure of a CS-1017 LC droplet in time. LC droplet was laser trapped by linearly polarized light of 1064 nm. (a) at 0–20 min, (b) 23 min, (c) 24 min, (d) 25 min, (e) 26 min, and (f) 26–30 min. Trapping laser power on the particle was 0.4 W. Scale bar, 10 μm.

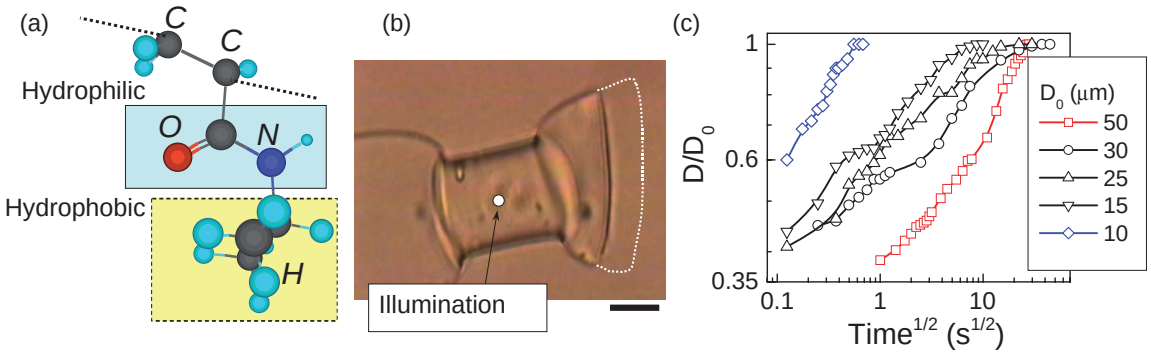

Figure 37. NIPAM molecular structure (a) showing the hydrophilic amido and hydrophobic isopropyl groups. Three-dimensional conformation of a single polymer building block was calculated by ChemDraw. (b) Volume-phase transition of a p-NIPAM gel rod induced by radiation force. Gel was immersed in D_2O, light intensity was 1 W. The dashed profile in (b) corresponds to the initial shape of a gel rod before irradiation. Scale bar, 10 μm. (c) Time evolution of volume-phase transition for gel rods of different diameters. D_0 is the equilibrium diameter of the rod in D_2O.[152]

a time scale of more than an hour. This exclude the heating and material convection inside the LC droplet as being the cause of the internal molecular reorientation.

The rearrangement of internal molecular structure orientation occurs as a result of dipole reordering in the electric field of the light. No causal dependence was found between the size of the LC droplets (2–5 μm) and the time required for the modification. In SmC LC the restructuring was found to take place non-monotonously (Figure 36). This is most likely related to the restructuring of the domains inside the droplet. Usually, SmC LC material in water will preferentially self-arrange into a droplet with an internal structure (the usual structure is a radial one), which does not satisfy the occurrence of torque when the LC droplet is laser-trapped by circularly polarized light. However, few droplets can be found to be rotatable by circularly polarized light, but usually at very low frequency ($\ll$0.1 Hz).[152] Most probably, their internal structure has domains, which were partly polar.

10. Volume-Phase Transitions Induced by Laser Tweezers in Gels

Laser tweezers can trap and manipulate (a spatial transfer or alignment by linearly polarized laser beam) objects as small as 10 nm as well as tens-of-micrometers in cross section. Namely, the gradient force of laser tweezers is responsible for immobilization of objects at the focal position. The acting principle of laser tweezers is the optically induced dipole force for nano-objects or an integral force generated by the impulse change when rays are traversing the micro-object.

In polymeric networks such as gels the gradient force causes compaction of the coils. When laser tweezers are set into gel immersed in heavy water the volume-phase transition can be triggered when gel is formed from molecules having hydrophobic and hydrophilic segments.[153] This is a fully reversible process triggered by laser compaction only.

10.1 Light Control over Weak Interactions in Polymers. Laser trapping[154] has been developed into a mature experimental technique, which allows measurement of extremely weak interactions of pico-/femto-newtons and detection of movements as small as few nanometers.[155,156] Radiation force of a laser trap acting on sub-μm-sized particles immobilize them inside a parabolic potential well and suppress their Brownian motion as it was confirmed by evanescent light scattering[157] and by Kramers theory[158] of thermally activated transition rates in a double-well laser-trap.[159] A single-beam laser trap affects particles as small as 10 nm.[154] Molecular assembling of 60–100 nm poly(*N*-isopropylacrylamide) (p-NIPAM building block is shown in Figure 37a) polymer fragments, which are of the typical globule-coil size of p-NIPAM was demonstrated in water solution by radiation force.[160,161] Heating via direct or solvent absorption of the laser trapping illumination can cause the volume-phase transition of p-NIPAM gel as well.[162] It was found that absorption of 1064 nm laser illumination by an overtone of O–H vibration of water molecules was responsible for local temperature increase and a coil-to-globule transition of polymers in the vicinity of the focus.[163]

Much theoretical and experimental work has been accomplished to understand the conformational modifications of polymer gels under different conditions, such as pH,[164] heating by light,[162] solvent composition,[165] and ionic content,[166] in

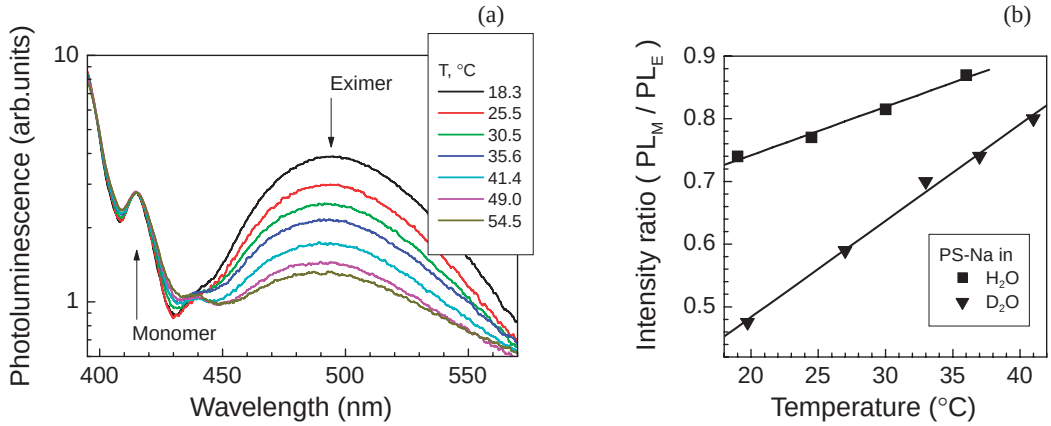

Figure 38. (a) Temperature dependence of PS-Na (1-pyrenesulfonic acid sodium salt) photoluminescence in D_2O. (b) The ratio of PL of monomers at 415 nm to that of eximers at 485 nm as a function of temperature in H_2O and D_2O, measured under the microscope excitation-detection conditions. Lines in (b) are the linear fits.

order to elucidate the roles of the different, mostly short-range weak interactions in gels.[167,168] It was experimentally demonstrated that long-range Coulomb forces can cause a frustrated volume phase transition in polyampholyte gel[169] as well. Shape/volume transformations have been proven to be responsible for the selectivity of chemical reactions,[170] where, as a matrix, the p-NIPAM gel was doped by compound responsible for a selective multi-point adsorption of target molecules. Polymer gels are good prototypes to mimic biomolecular machinery governed by short-range interactions such as hydrogen bonding, hydrophobic, van der Waals, and long-range Coulomb force in some proteins.

Yet another example of light control over the mechanical properties of material is the radiation force driven volume-phase transition of p-NIPAM gels (Figure 37b) immersed in D_2O.[153] When tightly focused light illuminates the p-NIPAM gel rod, the resulting volume-phase transition leads to the expulsion of the solvent D_2O out of the collapsed gel rod (Figure 37b). The coexistence of the hydrophilic amido and hydrophobic isopropyl groups in close vicinity inside p-NIPAM gel is responsible for the phenomenon of volume-phase transition. Phase separation during volume-phase transition takes place via the diffusion,[171] as can be seen from approximately linear $D \propto \sqrt{t}$ dependence (Figure 37c), where D is the diameter of gel rod and t stands for time. Factor 1.7 described well the difference in diffusion coefficient of phase separation in the case of 10 and 50 μm diameter gels (see the difference in the slopes of curves representing a collapse of gel rods in Figure 37c).

Volume-phase transition of p-NIPAM gel can be induced by the radiation force alone without a local temperature rise (Section **10.2**), which itself could cause the transition.[162] The radiation force induces a local compaction of a metastable gel around the focal point (Section **10.3**), which is enough to drive locally a volume-phase transition. The extension of collapsed phase is defined by elastic properties of gel's polymer network (Section **10.4**) and can be explained by the collective diffusion theory of gels.[171,172]

10.2 Measurement of Local Temperature inside Gel. To validate the mechanism of volume-phase transition the local temperature at the focal point inside a gel needs to be measured. First, a laser trap was established at the focus of objective lens (40× magnification; numerical aperture $NA = 0.85$) by illumination of continuous wave (cw)-YAG laser light at 1064 nm inside a gel sample. Rods and films of a p-NIPAM gel were prepared by free radical polymerization of a D_2O solution of NIPAM at 27 °C for 1 h (according to the procedure described in Ref. 166). A p-NIPAM gel was formed in a glass capillary tube or was cast over a cover glass slip to form the rod or film, respectively.

To evaluate the actual temperature at the focus inside gel, we measured the intensity ratio of the photoluminescence (PL) bands of 1-pyrenesulfonic acid sodium salt (PS-Na) dye at the monomers and eximers PL bands at 415 and 485 nm, respectively, in D_2O and H_2O solutions (Figure 38). PL of PS-Na was excited by a 380 nm wavelength laser illumination at 82 MHz repetition rate with pulse duration of 100 fs, which was introduced into a microscope and focused on a dye-permeated gel sample. Back-scattered PL was collected by the same objective lens and recorded by spectrometer. Linear dependence of the PL ratio was found valid over the temperature range from 22 to 55 °C (Figure 38b). The precision of temperature evaluation was better than 2 °C and it was higher for D_2O solution as compared with that of H_2O. The optical density of D_2O at 1064 nm $OD = 5 \times 10^{-2}$ (1 cm cuvette) is almost ten times lower than that of H_2O, while the absorption of p-NIPAM was negligible in a swollen state. Since the volume of p-NIPAM is changing at the focal point during the volume-phase transition, the eventual judgement of the actual temperature at the focus was carried out by the PL measurement of a PS-Na dye dispersed inside p-NIPAM gel. Two spectra recorded with the laser radiation switched on and off showed no local change of temperature at illumination power of 1.2 W, which was already 2–3 times larger than that necessary to trigger a volume-phase transition of gel kept at an ambient temperature of 27 °C.

The occurrence of volume-phase transition was judged by the direct CCD camera imaging as it is shown in Figure 37b, where the rod-shaped gel is seen collapsed around the irradiation point. An expected local temperature distribution can be evaluated numerically for a Gaussian light beam (heat source)[173] due to D_2O absorption at 1064 nm. An expected

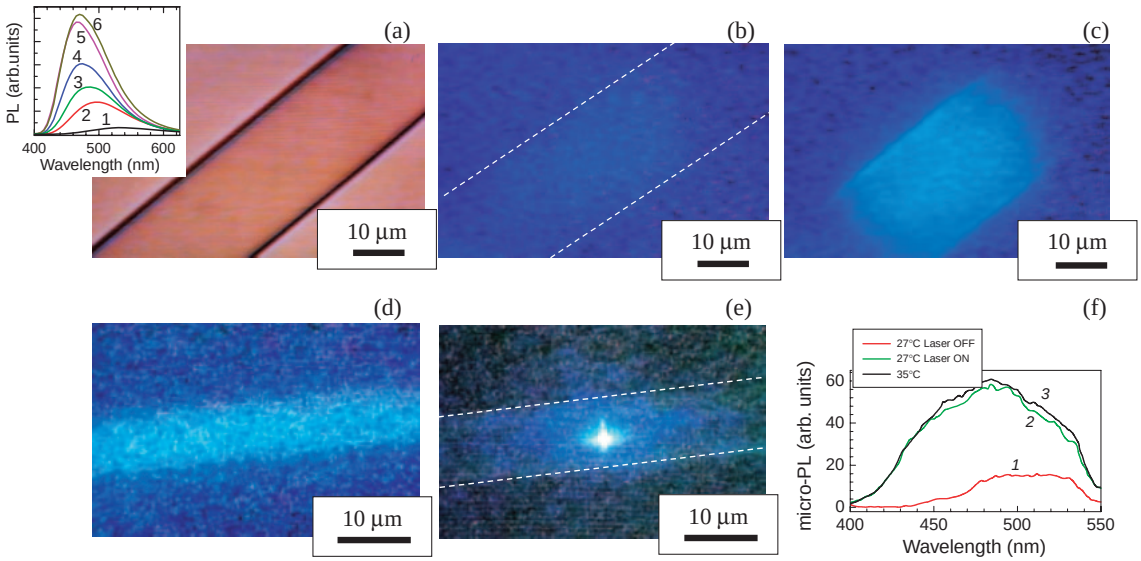

Figure 39. (a) Image of p-NIPAM gel doped with a fluorescent probe ANS-Na (8-anilino-1-naphthalenesulfonic acid sodium salt) soaked in H_2O inside a glass capillary. In the inset: PL of ANS-Na in H_2O (1; multiplied by 10), ethylene glycol (2), methanol (3), ethanol (4), 2-propanol (5), and 1-octanol (6). Image of the dye-doped gel under Hg-lamp excitation at 26 °C (b) and at 36 °C (c), respectively. Image of ANS-Na doped p-NIPAM gel (with PL maximum at 485 nm) in D_2O was imaged at $T = 35\,^{\circ}C > T_{VP}$ without (d) and at $T = 27\,^{\circ}C < T_{VP}$ with (e) 1.2 W laser illumination at 1064 nm. (f) PL of ANS-Na doped gel in D_2O measured under microscope conditions at 27 °C without (1) and with (2 as in (e)) laser irradiation. PL without laser illumination at 1064 nm at 35 °C is given by curve 3. p-NIPAM gel was formed inside a silane-modified capillary to avoid a collapse of gel at the conditions of volume-phase transition. Capillary walls are marked by dashed lines in (b,e).

temperature rise would be less than (1.7 ± 0.2) K for an irradiation power of 1.2 W. It is well-established fact that a temperature rise at the focal point is not a critical issue for two-photon microscopy where the intensities similar to those we have employed are routinely used.[174] Thus, the rise of temperature at the focus was negligible and can be excluded from consideration as a probable cause of a volume-phase transition of p-NIPAM gel at typical laser powers of 0.75–1 W.[153]

10.3 Radiation Force-Induced Compaction of Gel. Local compaction of gels induced by tightly focused non-absorbing illumination at the focal point is a universal property and was demonstrated in the case of thermally insensitive acryloamide (AA) gels, too.[153] Initial compaction of gel is induced by the optical gradient force and, in the case of p-NIPAM, is driving a metastable gel towards the volume-phase transition. The fluorescent probe 8-anilino-1-naphthalenesulfonic acid sodium salt (ANS-Na), which is sensitive to the hydrophobicity of its micro-environment, was chosen to check a radiation force-induced compaction of gels by measuring a dye's PL at 400–550 nm under Hg-lamp irradiation at 365 nm. p-NIPAM gel was soaked in a D_2O solution of the dye,[153] the PL of which is more intense in less polar environments or/and in the absence of water (inset to Figure 39a). A glass capillary containing a gel (Figure 39a) was chemically modified by a silane-coupler, which immobilized and prevented gel rod from collapsing under the conditions of volume-phase transition. In such a case, the internal morphological restructuring of gel could be observed by measuring the PL of dye. PL of ANS-Na was invisible at temperatures lower than that of volume-phase transition, $T_{VP} \approx 34\,^{\circ}C$, and became strong at temperatures over the T_{VP} (Figures 39b and 39c) in H_2O. In D_2O the enhancement of ANS-Na PL was observed from the illuminated area at high temperatures (Figure 39d) or when laser tweezers were set to a gel (Figure 39e). Spectral shape of PL was similar in both cases (Figure 39f). This shows that a compaction of gel on a sub-micrometer scale can be induced by either heating or by a radiation force and is due to a segment–segment interaction of the polymer coils. This interaction expels solvent and a solid(gel)–liquid(solvent) phase separation takes place. The dye entrapped in the "drier" regions contributes to the PL.

10.4 Mechanism of Gel Compaction. The phenomenon of polymer gel collapse has similarities to a coil-to-globule transition in polymer solutions (not necessarily gels), which is explained as follows:[175] the water molecules arrange themselves into hydrogen-bonding networks, which surround hydrophobic isopropyl segments of p-NIPAM and help to keep it in an extended coil state. With an increase of temperature, attractive forces eventually overcome the stiffness of the water network, which is hindered by increased thermal energy, and the coil collapses into a globule. For example, van der Waals forces between equal monomers (polymer–polymer affinity) are known to be higher than those between unlike pairs and dominate at separations of tens-of-nm according to $F_{VDW} \propto x^{-7}$,[176] where x is the distance between interacting particles. Gel is a cross-linked network of polymers immersed in fluid, which can undergo a volume-phase transition in response to changes in external conditions such as temperature solvent, pH, electric field, light. The competing forces which act on a gel are: rubber elasticity, polymer–polymer affinity, and hydrogen ion pressure. Competition between these forces, collectively called osmotic pressure, determine the equilibrium of gels. Volume-phase transition has been analyzed in terms of the mean field theory and the osmotic pressure is given by Flory's equation:[166]

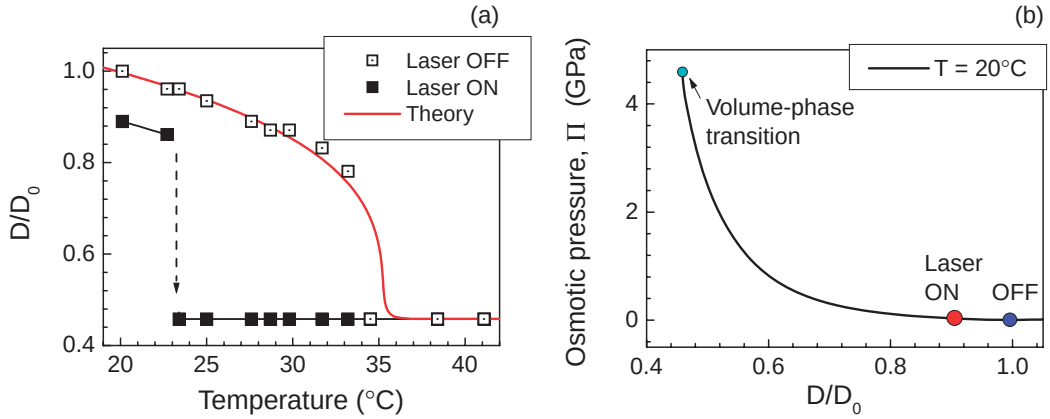

Figure 40. (a) Volume-phase transition of p-NIPAM gel rod induced without (open markers) and with (solid) laser illumination of 0.75 W vs. temperature plotted together with theoretical simulations.[166] (b) Osmotic pressure (by eq 33), Π, of gel at 20 °C vs. diameter change, D/D_0, where D_0 is the initial diameter of gel rod. Parameters to calculate a theoretical curve in (b) where obtained by regression fitting of experimental data (a). The osmotic pressure at volume-phase transition is ca. 4.1 GPa. Gel compaction at 20 °C induced by radiation force corresponds to the $\Delta\Pi = 45$ MPa osmotic pressure (the points laser ON, OFF in (b)).

$$\Pi = \nu kT\left[\frac{\phi}{2\phi_0} - \sqrt[3]{\frac{\phi}{\phi_0}}\right] - \left[\frac{(\Delta H - T\Delta S)N_A}{2v_1}\phi^2 + \frac{kTN_A}{v_1}\left(\ln(1-\phi)+\phi\right)\right] + \varphi\nu kT\frac{\phi}{\phi_0}, \quad (33)$$

where ϕ is the volume fraction of polymer network; f is the number of counter ions per chain ($\varphi = 0$ was used for undoped p-NIPAM gel); v_l is the molar volume of D_2O; N_A, Avogadro number; k, Boltzmann constant; and T, the absolute temperature. The parameters: enthalpy ΔH, entropy ΔS, total number of chains in gel ν, were evaluated from the fit of experimental data of gel's rod diameter D change vs. temperature. The value of the final volume fraction of polymer network $\phi_0 = 0.096$ was estimated from experimental asymptotic value of V/V_0 (here V is for volume), using approximation $V/V_0 = (D/D_0)^{1/3}$. One can find that the light-induced shrinkage of about 0.11 (the change of D/D_0) at 20 °C can be expressed in terms of osmotic pressure of 45 MPa, which is equivalent to an increase of temperature by $\Delta T \approx 7$ °C (Figure 40).

Though gels can be described as a small amount of polymer in a large amount of solvent, the dynamics of polymer solutions are not suitable for gels. The elasticity of inter-connected polymer network needs to be considered. The theory of collective diffusion was developed to describe the dynamics of gel networks.[171,172] The equation of motion for small displacement, $u(r,t)$, in gel of mass density, ρ, can be expressed as:

$$\rho\frac{\partial^2}{\partial t^2}u(r,t) = \nabla\tilde{\sigma} - f\frac{\partial}{\partial t}u(r,t), \quad (34)$$

where f is the friction coefficient between the network and the solvent, $\tilde{\sigma}$ is the stress tensor, and r with t are space and time coordinates, respectively. In most cases the left side, the acceleration term in eq 34 is much smaller than the stress produced by volume deformation (the first right-side term) and the polymer network solvent friction (the second term) terms. Equation 34 has three solutions corresponding to one longitudinal and two transverse modes, which describe the collective diffusion of gel:[177]

$$\frac{\partial u_l}{\partial t} = \frac{K + 4\mu/3}{f}\frac{\partial^2 u_l}{\partial x^2}, \quad (35)$$

$$\frac{\partial u_t}{\partial t} = \frac{\mu}{f}\frac{\partial^2 u_t}{\partial x^2}, \quad (36)$$

where x is the coordinate along the wave vector of the mode. The diffusion coefficient $D_{dif} = (K + 4\mu/3)/f$ corresponds to volume dynamics of a spherical gel. In the case of cylindrical and disk shaped gels the diffusion coefficient is time and position dependent. For example $D_{cylinder}(\text{center}) = 0.9D_{dif}$ and decreasing towards the edge where it is $2D_{dif}/3$; for disk $D_{disk}(\text{center}) = 0.78D_{dif}$ and $D_{dif}/3$, respectively.[177] The consequence of collective diffusion is that asymmetric gels (cylinder or disk shaped) have the same swelling/shrinkage ratios along both their axial and radial directions, i.e.:

$$\frac{u_{axial}(z,t)}{z} = \frac{u_{radial}(r,t)}{r}. \quad (37)$$

This is a key point for stimulus-sensitive response of gels. Once a volume-phase transition in gel is triggered, its shape will follow transformations defined by eq 37, which governs a liquid–solid phase separation within a gel. If the transition is triggered locally by radiation force of a tightly focused laser beam with focus size comparable to its wavelength, then the volume of the collapsed state can be much larger that the initially illuminated point, the stimulus. This phenomenon can be explained by diffusion-shear deformation of gel,[177] which is a direct consequence of collective diffusion model. The total energy of a gel can be separated into bulk energy and shear energy. The bulk energy is related to the volume change, which is controlled by diffusion. Meanwhile the build-up of shear energy can be minimized by readjusting the shape of gel[177] at no volume change (no solvent-polymer friction is involved in this case).

Local illumination of a 1.5 μm spot was found to trigger a large compaction over tens-of-μm along the axis of a cylindrical gel[153] or tens-of-μm area around the illumination spot in a gel film. The shrunken part of the gel can be moved along a

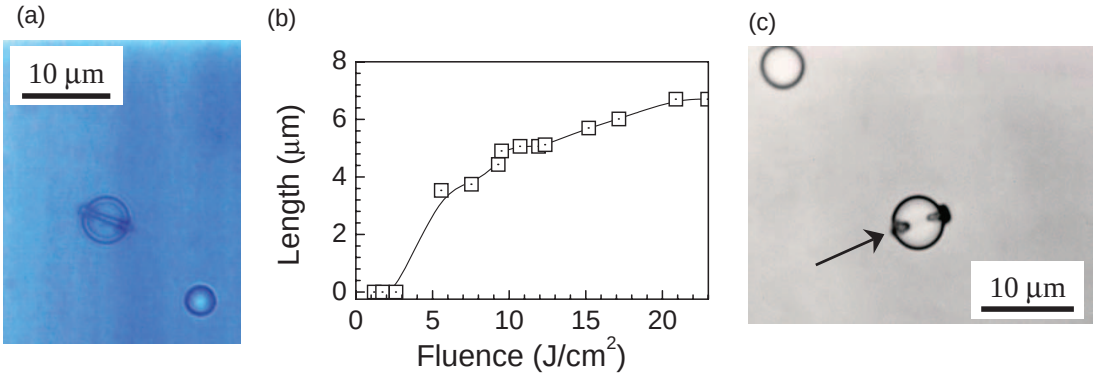

Figure 41. (a) Video frame of a laser-ablated PMMA particle in water. Scale bar, 5 μm. (b) Power dependence of a through-out ablation of PMMA particles. Ablation was made by a single 7 ns pulse at 355 nm. (c) Video frame of a partly laser-ablated PMMA particle in water.[179,183] Arrow marks the direction of pulsed irradiation, which made an ablation.

rod with the velocities of microns per second. The speed is limited by a diffusional process of phase separation of solvent (D_2O) and polymer. The contraction/expansion rate is defined as $t_c = c_d D_0^2$,[171] where $c_d \propto 1/D_{dif}$ is the contraction rate constant reciprocal to the diffusion coefficient ($c_d = 2 \times 10^{-9}$ s m^{-2} for p-NIPAM) and D_0 is the initial diameter of the gel rod. Laser beams can scan at much higher frequency, which allows transfer of the pre-programmed patterns of swollen-shrunken states on gel rods or films. The high Poisson ratio of gels $\sigma \approx 0.45$,[178] facilitates the triggering of a volume-phase transition, since the initial impact at the focal point delivers perturbation centro-symmetrically. The present field of gel-based applications[167] could be extended by adding an actuator, which could move 10^{-6}–10^{-3} mm as a result of described laser beam scanning. A gel membrane, the properties of which can be locally modified by laser scanning is possible. Such stimulus-sensitive gels can be considered as a kind of "artificial muscle," which can be manipulated (flexed) locally by laser irradiation without local temperature increase.

The gradient field at the focal point of a laser trap, which measures $1.22\lambda/NA \approx 1.5$ μm in diameter under our experimental conditions (marked by a circle in Figure 37b), was found to induce a compaction of 220 μm-thick p-NIPAM film, similarly as in a gel rod. Laser focus was set to the middle of a gel film and switched on and off. The time necessary to accomplish volume-phase transition was tens-of-seconds. This is larger by approximately an order of magnitude as compared with that of a p-NIPAM gel rod, where the 20–30 μm diameter gels were collapsing/swelling with a time constant of seconds[153] (Figure 37c). This pinching of the gel film was done reversibly at the same point without observable degradation for more than 200 cycles.

Here, we have demonstrated how a radiation force of a single beam laser trap can trigger volume-phase transition in the gels of p-NIPAM. The trap acts on sub-μm-sized coils of a polymer network by their immobilization against Brownian motion and by a gradient force-induced compaction. These two factors trigger volume-phase transition when proper thermal conditions are met (gel is at a temperature 5–10 degrees bellow that of transition). It is noteworthy that in a very different field, the volume-phase transition can be used to change patterns pre-recorded inside plastic by annealing.[59]

11. Photo-Structuring by Laser Tweezers: Ablation, Assembly, and Welding

Functionalization of materials by laser ablation (removal of material from the surface by laser irradiation) is a fast growing field of science and technology. In Latin the "ablatio" means to take out, remove. Laser trapping can be combined with laser microfabrication by ablation as well. A micrometer-sized "workpiece" can be laser trapped and can be modified by irradiation with additional high fluence laser pulse.[179] An extension of this technique was introduced[180] where separate particles were laser trapped and manipulated. The additional pulsed laser exposure made an assembly by laser-induced melting at the joint points, welding single polymer beads into a complex structure. Among the possible applications of laser trapping in microfabrication[140] we could mention: controlled ablation of micro-capsules[181] for drug delivery systems, microfabrication of flexible joints between laser-trapped objects by controlled gelification (polymerization),[54] marking and drilling of a "workpiece" by a laser-trapped diamond particle,[182] etc.

11.1 Photo-Structuring by Using a Single Laser Trap. Let us consider the laser ablation of a spherical polymer [poly-(methyl methacrylate) (PMMA)] microbead in more details.[183] First, a droplet is laser trapped by 150–200 mW cw-illumination at 1064 nm. Then, the trapped droplet is coaxially irradiated to by a single pulse of 7 ns (FWHM value) at 355 nm. After again the trapping the droplet, an in situ observation of the ablation site was made by in microscope. Three distinct ablation patterns were observed: (i) a throughout ablation of a PMMA microsphere, (ii) two-side ablation along the propagation of the beam, and (iii) ablation of the opposite side to that irradiated (Figures 41a–41c). The most stable laser trapping conditions corresponded to the orientation of a microsphere when an ablated structure was perpendicular to the optical axis of laser tweezers. This facilitated an observation of the ablation channel. The laser fluence in a single pulse needed to make the throughout channel in a droplet is shown in Figure 41d.

The minimal laser power at 355 nm necessary for a throughout ablation of a microsphere of PMMA was measured. The diameter of ablated micro-channel was constant in the range of laser fluencies employed and was about 0.67 μm or $\propto 2\lambda$.

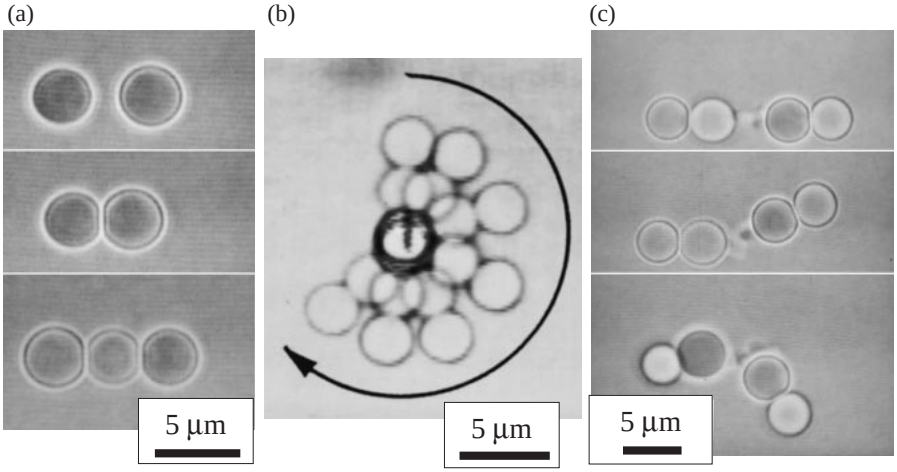

Figure 42. (a) Optical images of welded structure of polystyrene beads in water. The welding of beads was made by a single 20 ps 355 nm laser pulse pointed to a contact spot between beads. Fabrication was carried out by adding one additional bead at a time (top-to-bottom images). (b) Clockwise rotation of an integrated microstructure of polystyrene beads by using two-beam laser tweezers (overlaid image). Laser trapping power was 290 mW and the circular scan rate was $120^{\circ}\,s^{-1}$. (c) Optical images of laser manipulated flexible silica—AA-gel structure. One-photon photoinitiator DHBP was used for polymerization at 532 nm.[54,179,180,185]

The fluence dependence of the length of a throughout ablated channel is shown in Figure 41d. Dependence is plotted in a form adopted from the laser ablation studies, where the threshold of ablation for a Gaussian beam can be determined by fitting the experimental results with:

$$F_{\mathrm{th}} = F_0 \exp -\left(\frac{L}{l_0}\right)^2, \tag{38}$$

where $F_{\mathrm{th},0}$ are the threshold and incident fluencies, respectively, l_0 is the length of the Gaussian beam waist, and L is the depth of ablated dip. Fitting the experimental results yielded in the overestimated values for the ablation threshold fluence $F_{\mathrm{th}} = 3.75\,\mathrm{J\,cm^{-2}}$ and $l_0 = 7.5\,\mu\mathrm{m}$. Ablation threshold for PMMA film was found at $<1\,\mathrm{J\,cm^{-2}}$ and the waist length of Gaussian beam can be calculated as the two Rayleigh lengths $2z_{\mathrm{R}} = 2n\pi\omega_0^2/\lambda$, where $n \simeq 1.5$ is the refractive index at the focus for the wavelength λ and the Gaussian beam waist is given by $\omega_0 \simeq 0.61\lambda/NA$ with $NA = 1.3$ being the numerical aperture of the objective lens. For our experimental conditions the theoretical beam waist was $2\omega_0 = 0.33\,\mu\mathrm{m}$ and its length $2z_{\mathrm{R}} = 0.74\,\mu\mathrm{m}$. Thus, experimental data can not be explained by laser ablation in the waist of a Gaussian pulse. The effect of self-focusing also is irrelevant at the region of employed pulse powers, since $10\,\mathrm{J\,cm^{-2}}$ corresponds to 1.25 W/pulse and is much smaller than the critical power of self-focusing, which we can estimate from the constants of borosilicate glass by[184] $P_{\mathrm{cr}} = \varepsilon_0 c\lambda^2/(4\pi\gamma) \simeq 3.1\,\mathrm{MW}$, where ε_0 is the vacuum permittivity, c speed of light, and the nonlinear refractive index is $\gamma = 0.68 \times 10^{-22}\,\mathrm{m^2\,V^{-2}}$.

The discussion above considered an ideal diffraction limited focusing free from aberrations and was based on the known parameters of borosilicate glass (similar to those of PMMA glass). In reality, focusing of light inside a microsphere is subject to spherical aberration. However, the difference is too large (more than four orders of magnitude) between the evaluated experimental value P_{cr} and that required for the effects on nonlinear pulse propagation to become significant.[183] Aberrations primarily change the axial location of the focus, however, ablation of the interior of microsphere was never observed before ablation of the rear surface (Figure 41c). These considerations allow us to exclude the aberrations and nonlinear pulse propagation as being responsible for the observed pattern of ablation.[183]

11.2 Photo-Structuring by Using Two Laser Tweezers. Two laser tweezers can be easily set by combining co-axially two beams of different polarizations at the same wavelength and introducing them into a microscope. This kind of "two-hand" manipulator is a useful tool to trap and modify micrometer-sized objects.[180] Pulsed laser irradiation can be additionally introduced and delivered to the focus where welding or polymerization of two trapped microparticles can be carried out as shown in Figure 42.

Two polystyrene beads were trapped by two separate laser traps using laser power of 100–150 mW per beam, as shown in Figure 42a. The beads were drawn close to each other, and welded together at the point of contact by a single 20 ps 355 nm laser pulse. The energy density was $2\,\mathrm{J\,cm^{-2}}$. Afterwards, the newly fabricated two-bead structure was re-trapped several times to make three- and multi-bead structures, respectively (Figure 42a). At any step of fabrication two-beams laser tweezers made it possible to hold and manipulate the structure as shown in Figure 42b.

This type of micro-welding by a single pulse ablation is technically similar to a multibeam laser manipulation and fixation technique where the assembly of several laser-trapped latex particles was achieved via polymerization. In water solution of acrylic acids, photo-polymerization results in a gelled material. Very low friction forces existing between gels as well as between gels and solid surfaces, make them interesting candidates for applications in artificial joint implants. In the experiments silica beads were laser trapped and manipulated in aqueous solution of the acrylic acid monomers (AA, 2

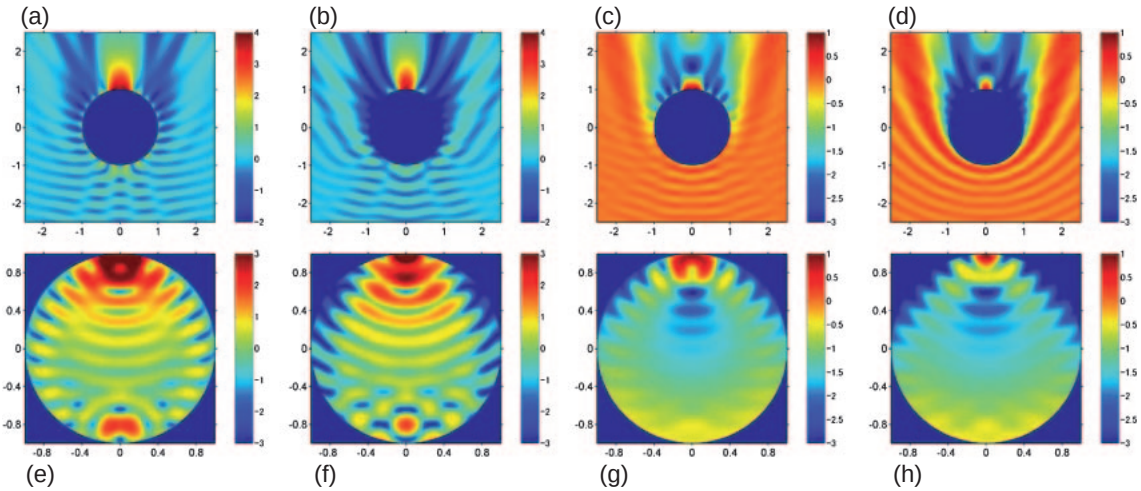

Figure 43. Calculated scattered light intensity distributions around a dielectric sphere with size parameter $x = (2\pi/\lambda)r = 10$ (upper row) and inside the particle itself (lower row) in a *XZ*-plane.[183] The radius of the particle is normalized $r = 1$. Relative refraction index employed for calculations was $m = 1.5 + 0i$ (a, b, e, and f) and $m = 1.5 + 0.1i$ (c, d, g, and h), respectively. The sphere was irradiated by light of intensity 1 (bottom-up direction in the images) which was parallel ($\parallel$ in *XZ*-plane for (a, c, e, and g)) or perpendicular ($\perp$ to the image plane for (b, d, f, and h)). Color encoding represents the logarithmic scale of intensity given on the colorbars (note the different scales). The intensities higher or lower than those presented by bars are rendered in colors corresponding to maximum and minimum intensity, respectively.

mol dm^{-3}), photoinitiator, and conjugator/crosslinker. For initiation of polymerization by two-photon absorption, 2,2-diethoxy-1-phenylethanone (DEPE, 0.1 mol dm^{-3}, with absorption at wavelengths <270 nm) was used as photoinitiator. We have also found that a single-photon photoinitiator, 4,4′-dihydroxybenzophenone (DHBP, 0.8 mol dm^{-3}), can be used as well at the same wavelength of 532 nm. The conjugator in both cases was *N*,*N*′-methylenebisacrylamide (MBA) at a concentration of 0.03 mol dm^{-3} for two-photon, and 0.1 mol dm^{-3} for single-photon initiation reactions.

The trapped beads were synchronously moved along the axis aligned through their centers, and illuminated by laser pulses at 532 nm (Figure 42c). As a result, an AA-gel formed between the silica beads. The surface of the silica beads remained chemically unmodified, and the gel–silica contact was maintained solely by physical forces. However, the contact was strong enough to withstand laser manipulation forces over 250 pN.

11.3 Mie Scattering and Ponderomotive Forces Acting on a Microsphere. The actual light intensity distribution around a micrometer-sized particle is a key factor for laser fabrication by ablation. At this particular particle size relevant to most laser trapping experiments (0.1–10 μm in diameter), the Rayleigh scattering according to $I_s \propto \lambda^{-4}$ (I_s is the intensity of scattered light) is not valid and one needs to consider the more general Mie scattering.[184] We have implemented the code developed by Barber and Hill[186] for calculation of Mie scattering by a spherical dielectric particle with relative refraction index *m*. This index is defined as a ratio between the index of a particle to that of the surroundings. The entire scope of angular intensity distribution of the scattered light field is shown in Figure 43 for the inside and outside of a dielectric sphere. Localization of the light inside the sphere is clearly seen. Additional absorption by a microsphere accounted for by the imaginary part of the relative refractive index did not change considerably the pattern of light localization on the surface and inside of the microspheres (Figures 43c, 43d, 43g, and 43h). These figures can explain consistently the ablation of the two opposite sides of the microsphere without damaging the inside region of the microparticle. Also, ablation of the opposite side to that irradiated (Figure 41c) can be understood from light focusing by a sphere (Figure 43).

Formation of a throughout microchannel in PMMA microsphere (Figure 41) by ablation should be discussed in more detail. First, let us evaluate ponderomotive forces exerted on a laser-trapped PMMA particle. It was demonstrated how ductile (small Young's modulus, $E < 10^3$ Pa) particles such as red blood cells, can be stretched in laser tweezers.[187] The reason for stretching is the light impulse changes during passage through boundaries between different refractive indices as shown in Figure 44. When the light enters the material of higher refractive index, *n*, it gains the impulse ($p = n \cdot \text{Energy}/c$) and vice versa. Let us consider the indexes are $n_0 = 1.326$ (water-like) and $n_1 = 1.370$ (dielectric particle) at the wavelength of laser tweezers at 1064 nm. Then, at right angle incidence the reflection coefficient is just $R = (n_1 - n_0)^2/(n_1 + n_0)^2 \simeq 0.027\%$. The forces acting on the front and back planes can be found from the impulse change according to:[187]

$$F_{\text{front}} = (n_0 - (1 - R)n_1 + Rn_0)P/c, \quad (39)$$

$$F_{\text{back}} = (n_1 - (1 - R)n_0 + Rn_1)(1 - R)P/c. \quad (40)$$

For a laser trapping power of $P = 0.75$ W the light pressure or the scattering force is given by $F_{\text{back}} - F_{\text{front}} = 3.6$ pN, while the stretching force, $(F_{\text{back}} + F_{\text{front}})/2 = 110$ pN, is much larger. As was demonstrated,[187] such a stretching force when doubled by adding a second counter-propagating beam was enough to introduce observable shape deformations of an erythrocyte. This simple model described quantitatively well the shape changes of an erythrocyte.[187]

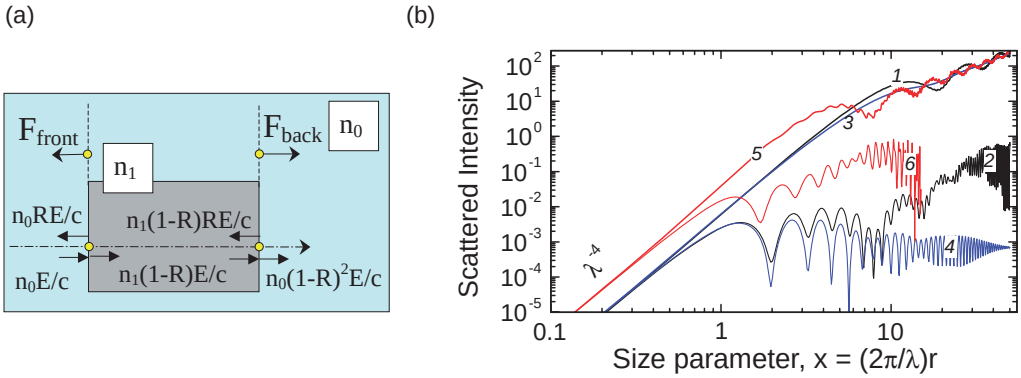

Figure 44. (a) Schematic presentation of the forces acting on an object by light passage through it (see text for explanation). (b) Forward ($\theta = 0$) and backward ($\theta = \pi$) scattered light intensity as a function of size parameter $x = (2\pi/\lambda)r$, where θ is the angle of scattering, r = diameter of spherical particle, and λ = wavelength. The relative refractive index, m, was taken: $m = 1.2 + 0i$ for curves 1 ($\theta = 0$) and 2 ($\theta = \pi$), $m = 1.2 + 0.05i$ for curves 3 ($\theta = 0$) and 4 ($\theta = \pi$), and $m = 1.5 + 0i$ for curves 5 ($\theta = 0$) and 6 ($\theta = \pi$).

Similar ponderomotive stretching force would act on a laser trapped particle during ablation by a single pulse. Let us evaluate this force for an ablation pulse fluence of $10\,\mathrm{J\,cm^{-2}}$ (Figure 41a), which in terms of power per pulse is 1.25 W. Elongation of the laser trapped polymer particle by passage of an ablation pulse can be estimated from Hook's law $\sigma = \varepsilon E$, where stress is $\sigma =$ Force/Area and strain $\varepsilon = \Delta l/l$ is defined by the change of length, Δl, and length, l, respectively. E is Young's modulus, which is small $E = 1$–$10\,\mathrm{MPa}$ for ductile rubber-type materials and typically 1–4 GPa for polymers. Stretching of an $l = 10\,\mu\mathrm{m}$ particle by a laser pulse of 1.25 W tightly focused to a spot area of $\pi\omega_0^2$ on a ductile material with $E = 1\,\mathrm{MPa}$ exerts a tensile stress of $\sigma \simeq 10\,\mathrm{kPa}$. Such a stress would cause just a 1% axial elongation of a particle, too small to be relevant for the formation of a microchannel, even if the yield stress, which has very strong thermal dependence in polymer materials,[188] is small.

High ablation pressure and temperature are necessary to evaporate and melt the material. Also, it triggers a shock wave, which is a part of the removal mechanism of material along the channel.[183]

The complexity of the forward ($\theta = 0$) and backward ($\theta = \pi$) scattered light intensity vs. size parameter $x = (2\pi/\lambda)r$ is illustrated by Mie scattering calculations[186] as given in Figure 44b, where r is the diameter of a spherical particle and λ is the wavelength. A distinct transition from the Rayleigh regime to Mie scattering is seen at size parameters larger than $x = 1$. In fact, one needs to consider an actual intensity distribution around and inside the particle to evaluate the ponderomotive forces exerted upon the particle.

Mie scattering can be effectively utilized to deliver excitation at a particular wavelength inside a spherical micro-particle. This principle was used to excite lasing whispering gallery modes (or morphology dependent resonances (MDR)) in dye-doped spherical and elliptical micro-particles.[149] The microcavity of a particle can provide necessary feedback for lasing in the case of active media (usually a dye) being inside the cavity or even outside. In the later case the dye emission enters the cavity as an evanescent field and is amplified via the MDR mechanism. The principles of such laser are given in Ref. 189. Laser-manipulated active lasing micro-spheres are utilized for basic studies of quantum electrodynamics[190] as well as being potential light-sources in micro-mechanical and micro-fluidic applications.

Spherical cavities store light energy predominantly in a subsurface layer,[189,190] where spatial and spectral concentration of electromagnetic energy takes place. Inelastic light scattering is proportional to the square of the Purcell factor, which accounts for an increase of photon density of states at the resonance frequency. For a silica glass spherical microcavity with quality $Q = 5 \times 10^9$ the enhancement becomes $f^2 \simeq 10^{14}$.[191] Spherical microcavities available in practice with lower Q-factors of the order of 10^8, leading to Purcell factors of $f = 2 \times 10^5$, and consequently, can enhance scattering by a factor of $f^2 \simeq 4 \times 10^{10}$. This is much higher than enhancement achievable with noble metal nanoparticles, approximately 10^6. This makes micro-spheres attractive for sensor applications were micro-cavity and nanoparticle enhancements of local light field can be utilized.

11.4 Laser Manipulation by Complex Light Fields. Apart of the classical laser tweezers considered to date (Sections **9**, **10**, and **11**), which are based on Gaussian beams for laser trapping and manipulation, there is a growing interest in the use of more complicated light fields. Burns et al. proposed to use multi-beam interference patterns to arrange microspheres into 3D patterns called "optical matter."[192] It was demonstrated that all fourteen Bravais lattices can be simulated by the interference of just four non-coplanar light beams.[193] The other approach in multi-beam laser manipulation is to use a diffractive beam splitter to generate multi-focus arrays at the focus of a conventional microscope.[194]

Bessel beams[83] can be used to trap microparticles and to guide them along the non-diffracting core of the beam due to light pressure.[195] By changing the divergence of the Gaussian incident beam on the Bessel-beam-generating axicon lens a tilted-periodic ("washboard") potential can be controlled. This allows a size selective capture, manipulation and guiding of microparticles.[196] The stochastic resonance is considered as being a cause of size-selective capture into the ring-structure of the Bessel beam. Similar size-selective gathering of microspheres was reported in a Newton ring interference pattern.[197]

In the field of optically driven micromechanical systems, angular momentum transfer to a laser trapped absorbing particles was demonstrated using a doughnut laser beam with helical wave-front structure.[198] Controlled formation of complex patterns and their manipulation can be achieved in the interference fields of two annular Laguerre–Gaussian (LG) beams[199] or in the interference field between a Gaussian and annular beam.[200] In these cases too, the mechanism of torque is a transfer of an angular momentum of the helical wave-front. Direction of rotation can be controlled by introducing frequency shifts into the interfering beams.[201]

The range of applications of laser tweezers reviewed in Sections **9**, **10**, and **11** does not cover the entire scope of this fast growing field. Here, we focused on applications which are based on combination of laser trapping and laser microfabrication (ablation and photopolymerization) techniques for future microtechnology applications. Future micro-fluidic and nano-/micro-mechanical systems (NEMS and MEMS) will most probably include optically driven motors of different kinds. Nematic liquid crystals are among the candidates for high efficiency torque harnessing optically driven rotors. We also believe in a wider application of laser tweezers in basic research on weak forces in bio-/bio-compatible materials such as gels, since this technique is indispensable due to its unique domain of applicability in the small dimensions of 10–10^4 nm and weak fN–pN forces.

12. Overall Conclusions and Outlook

Very different applications of 3D laser structuring of materials have been overviewed by presenting particular examples. The batch processing approach of exposure and development of the recorded patterns is expected to become a working principle for practical implementation of nano-/micro-technology. Fabrication of 3D photonic crystal templates and wet etching of channels for micro-fluidics are just two examples of this method.[87,202] The optical control of phase transitions in materials is one of the underlying principles of the laser nano-micro-fabrication discussed here. Materials are laser photo-modified and then the chemically, structurally, or optically altered regions provides new functionality or the possibility of further post-processing. This approach can be applied to chemically inert materials such as wide bandgap glasses and crystals widely used in UV optical applications by wet processing of photo-modified regions. Hence, the phase transformations of materials induced optically render them processable or deliver new functionality. Such phase transformations have been discussed here in the case of crystals, gels, and liquid crystals.[145,153,203] The volume-phase transition of gels and optical control of internal molecular ordering of liquid crystals are expected to add new functionalities to micro-mechanical and micro-fluidic applications.

Future progress of 3D laser photo-structuring will be based on novel methods of beam delivery; wavelength, pulse duration, repetition rate, polarization, wave front, lateral and axial intensity distributions should be flexibly controlled in order to make them most suitable for photo-structuring. The laser structuring is expected to be based on implementation of self-learning algorithms by monitoring, controlling, and changing exposure parameters via feedback loop for a required outcome. This also allows the adoption of processing sequences to different materials. The 3D structures of required parameters and functions should be recorded by a simple and fast process, preferably, in a single processing step to make such 3D photo-structuring approaches practical.

The impact of the advanced 3D laser writing and holography for the chemistry field is expected in several directions. The surfaces patterned with nanostructures by ablation or photo-polymerization can provide new substrates which can be funcionalized for practical sensor applications and be useful in development of new analytical methods and tools. The planar and volumetric 3D structures are prospective in catalytic and fuel cell applications.

In micro-/nano-fluidics and sequencing applications where pure dielectric materials are increasingly required in order to avoid screening of the applied electrophoretic fields by movable ions, the demonstrated wet etching of structures amorphised or photo-modified by laser irradiation in sapphire, quartz, or glass[204] can be adopted. Similar laser irradiation conditions can be used to process samples immersed in water,[205,206] then, the channels can be formed by scanning laser beam in a direct laser writing fashion.[207] This is expected to provide micro-channels for sequencing at the ultimate one base pair resolution on a miniaturized micro-fluidic chip. The micro-fluidic devices for assay applications can be made by light-induced back-side wet etching (LIBWE) which has recently achieved a high aspect ratio processing of large areas of transparent glass and crystal materials.[208–210] All the above-mentioned laser fabrication methods are expected to guide development of fast and accurate analytical techniques and sensor applications.

It is expect that recent fast development of micro-devices (micro/nano-electro-mechanical systems MEMS/NEMS) where new principles of nano-/micro-object manipulation and actuation are constantly emerging will promote research in photo-responsive materials based on soft-materials: polymers, liquid crystals, and gels.[211] New materials chemically designed and purified with a required nano-structure and funcionality can be incorporated into MEMS/NEMS. This direction of merging top-down and bottom-up approaches in nanotechnology already can be discerned from current scientific publications. New principles of energy conversion, i.e., light-to-mechanical, light-to-electrical (and vice versa), etc., can become efficient on a particular size scale do to scaling laws of interactions.[212] The inherent 3D character of the methods discussed here makes them applicable for a highly required miniaturization of micro-fluidic devices and creation of new 3D-structured cellular materials. Merger of fluidic, electrical, photonic, and mechanical technologies is a promising route of modern applied and basic science.

We acknowledge contributions from our former group members, doctoral students and postdocs over the last decade 1997–2007 and in particular to Drs. Y. Tanamura, M. Watanabe, K. Yamasaki, T. Takasone, M. Miwa, T. Kondo, K. K. Seet, N. Murazawa, A. Marcinkevicius, V. Jarutis, master and bachelor students T. Ebisui, Y. Tabuchi, K. Nishimura. We are indebted for fruitful discussions to all our co-authors.

References

1 *Three-Dimensional Laser Microfabrication: Fundamentals and Applications*, ed. by H. Misawa, S. Juodkazis, Wiley, **2006**.

2 P. F. McMillan, *Nat. Mater.* **2005**, *4*, 715.

3 A. B. Belonoshko, *Science* **1997**, *275*, 955.

4 G. E. Duvall, K. M. Ogilvie, R. Wilson, P. M. Bellamy, P. S. P. Wei, *Nature* **1982**, *296*, 846. doi:10.1038/296846a0

5 Q. Johnson, A. C. Mitchell, *Phys. Rev. Lett.* **1972**, *29*, 1369.

6 S. D. Gilev, A. M. Trubachev, *J. Phys.: Condens. Matter* **2004**, *16*, 8139.

7 A. N. Dremin, *Combust., Explos. Shock Waves* **2000**, *36*, 704.

8 A. Vogel, J. Noack, G. Hüttman, G. Paltauf, *Appl. Phys. B: Lasers Opt.* **2005**, *81*, 1015.

9 U. K. Tirlapur, K. König, *Nature* **2002**, *418*, 290.

10 E. Yablonovitch, *Phys. Rev. Lett.* **1987**, *58*, 2059.

11 S. John, *Phys. Rev. Lett.* **1987**, *58*, 2486.

12 K. Busch, G. von Freymann, S. Linden, S. F. Mingaleev, L. Tkeshelashvili, M. Wegener, *Phys. Rep.* **2007**, *444*, 101.

13 E. M. Purcell, *Phys. Rev.* **1946**, *69*, 681.

14 S. Juodkazis, V. Mizeikis, H. Misawa, *Adv. Polym. Sci.* **2007**, in press.

15 M. Grätzel, *Nature* **2001**, *414*, 338.

16 V. M. Shalaev, *Nat. Photonics* **2007**, *1*, 41.

17 http://www.microchem.com/products/su_eight.htm

18 G. Witzgall, R. Vrijen, E. Yablonovitch, V. Doan, B. J. Schwartz, *Opt. Lett.* **1998**, *23*, 1745.

19 T. Kondo, S. Juodkazis, H. Misawa, *Appl. Phys. A: Mater. Sci. Process.* **2005**, *81*, 1583. doi:10.1007/s00339-005-3337-7

20 S. Juodkazis, V. Mizeikis, K. K. Seet, M. Miwa, H. Misawa, *Nanotechnology* **2005**, *16*, 846.

21 H. Sun, Y. Xu, S. Juodkazis, K. Sun, M. Watanabe, S. Matsuo, H. Misawa, J. Nishii, *Opt. Lett.* **2001**, *26*, 325.

22 K. K. Seet, V. Mizeikis, S. Matsuo, S. Juodkazis, H. Misawa, *Adv. Mater.* **2005**, *17*, 541. doi:10.1002/adma.200401527

23 K. K. Seet, V. Mizeikis, S. Juodkazis, H. Misawa, *Appl. Phys. A: Mater. Sci. Process.* **2005**, *82*, 683. doi:10.1007/s00339-005-3459-y

24 K. K. Seet, V. Mizeikis, S. Juodkazis, H. Misawa, *J. Non-Cryst. Solids* **2006**, *352*, 2390.

25 H. Ishii, S. Juodkazis, S. Matsuo, H. Misawa, *Chem. Lett.* **1998**, 655.

26 M. Watanabe, H.-B. Sun, S. Juodkazis, T. Takahashi, S. Matsuo, Y. Suzuki, J. Nishii, H. Misawa, *Jpn. J. Appl. Phys.* **1998**, *37*, L1527.

27 S. Juodkazis, H. Ishii, S. Matsuo, H. Misawa, *J. Electroanal. Chem.* **1999**, *473*, 235.

28 S. Juodkazis, M. Watanabe, H.-B. Sun, S. Matsuo, J. Nishii, H. Misawa, *Appl. Surf. Sci.* **2000**, *154–155*, 696.

29 S. Juodkazis, A. Yamaguchi, H. Ishii, S. Matsuo, H. Takagi, H. Misawa, *Jpn. J. Appl. Phys.* **2001**, *40*, 4246.

30 P. Eliseev, H.-B. Sun, S. Juodkazis, T. Sugahara, S. Sakai, H. Misawa, *Jpn. J. Appl. Phys.* **1999**, *38*, L839.

31 K. Yamasaki, S. Juodkazis, T. Lippert, M. Watanabe, S. Matsuo, H. Misawa, *Appl. Phys. A: Mater. Sci. Process.* **2003**, *76*, 325.

32 S. Juodkazis, K. Yamasaki, V. Mizeikis, S. Matsuo, H. Misawa, *Appl. Phys. A: Mater. Sci. Process.* **2004**, *79*, 1549. doi:10.1007/s00339-004-2845-1

33 S. Juodkazis, H. Okuno, N. Kujime, S. Matsuo, H. Misawa, *Appl. Phys. A: Mater. Sci. Process.* **2004**, *79*, 1555. doi:10.1007/s00339-004-2846-0

34 S. Juodkazis, H. Misawa, I. Maksimov, *Appl. Phys. Lett.* **2004**, *85*, 5239.

35 S. Juodkazis, P. G. Eliseev, M. Watanabe, H.-B. Sun, S. Matsuo, T. Sugahara, S. Sakai, H. Misawa, *Jpn. J. Appl. Phys.* **2000**, *39*, 393.

36 S. Juodkazis, N. Murazawa, H. Wakatsuki, H. Misawa, *Appl. Phys. A: Mater. Sci. Process.* **2007**, *87*, 41.

37 T. Kondo, S. Matsuo, S. Juodkazis, H. Misawa, *Appl. Phys. Lett.* **2001**, *79*, 725.

38 T. Kondo, S. Matsuo, S. Juodkazis, V. Mizeikis, H. Misawa, *Appl. Phys. Lett.* **2003**, *82*, 2758.

39 T. Kondo, S. Matsuo, S. Juodkazis, V. Mizeikis, H. Misawa, *J. Photopolym. Sci. Technol.* **2003**, *16*, 427.

40 T. Kondo, K. Yamasaki, S. Juodkazis, S. Matsuo, V. Mizeikis, H. Misawa, *Thin Solid Films* **2004**, *453–454*, 550.

41 H. Misawa, T. Kondo, S. Juodkazis, V. Mizeikis, S. Matsuo, *Opt. Express* **2006**, *14*, 7943.

42 T. Kondo, S. Juodkazis, V. Mizeikis, S. Matsuo, H. Misawa, *New J. Phys.* **2006**, *8*, 250. doi:10.1088/1367-2630/8/10/250

43 M. Gu, G. Zhou, *Spherical Aberration and its Compensation for High Numerical Aperture Objectives* in *3D Laser Microfabrications: Principles and Applications*, ed. by H. Misawa, S. Juodkazis, Wiley, Berlin, **2006**.

44 E. Vanagas, I. Kudryashov, D. Tuzhilin, S. Juodkazis, S. Matsuo, H. Misawa, *Appl. Phys. Lett.* **2003**, *82*, 2901.

45 A. Marcinkevicius, V. Mizeikis, S. Juodkazis, S. Matsuo, H. Misawa, *Appl. Phys. A: Mater. Sci. Process.* **2003**, *76*, 257.

46 E. E. Gamaly, S. Juodkazis, K. Nishimura, H. Misawa, B. Luther-Davies, L. Hallo, P. Nicolai, V. Tikhonchuk, *Phys. Rev. B* **2006**, *73*, 214101.

47 R. Fisher, B. Tadic-Galeb, *Optical System Design*, McGraw-Hill, **2000**.

48 S. Juodkazis, T. Kondo, S. Dubikovski, V. Mizeikis, S. Matsuo, H. Misawa, *Proc. SPIE* **2002**, *5147*, 226.

49 S. Juodkazis, K. Nishimura, H. Misawa, *Chin. Opt. Lett.* **2007**, *5*, S198.

50 R. Trebino, P. O'Shea, M. Kimmel, X. Gu, *Opt. Photonics News* **2001**, *12*, 23.

51 F. Verluise, V. Laude, Z. Cheng, C. Spiellmann, P. Tournois, *Opt. Lett.* **2000**, *25*, 575.

52 S. Juodkazis, K. Nishimura, S. Tanaka, H. Misawa, E. E. Gamaly, B. Luther-Davies, L. Hallo, P. Nicolai, V. Tikhonchuk, *Phys. Rev. Lett.* **2006**, *96*, 166101.

53 K. K. Seet, S. Juodkazis, V. Jarutis, H. Misawa, *Appl. Phys. Lett.* **2006**, *89*, 024106.

54 S. Juodkazis, M. Horyama, M. Miwa, M. Watanabe, A. Marcinkevicius, V. Mizeikis, S. Matsuo, H. Misawa, *Proc. SPIE* **2001**, *4644*, 27.

55 S. Maruo, K. Ikuta, *Appl. Phys. Lett.* **2000**, *76*, 2656.

56 M. Horiyama, H. Sun, M. Miwa, S. Matsuo, H. Misawa, *Jpn. J. Appl. Phys.* **1999**, *38*, L212.

57 M. Miwa, S. Juodkazis, T. Kawakami, S. Matsuo, H. Misawa, *Appl. Phys. A: Mater. Sci. Process.* **2001**, *73*, 561.

58 K. Yamasaki, S. Juodkazis, S. Matsuo, H. Misawa, *Appl. Phys. A: Mater. Sci. Process.* **2003**, *77*, 371.

59 S. Juodkazis, K. Yamasaki, S. Matsuo, H. Misawa, *Appl. Phys. Lett.* **2004**, *84*, 514.

60 K. M. Ho, C. T. Chan, C. M. Soukoulis, R. Biswas, M.

Sigalas, *Solid State Commun.* **1994**, *89*, 413.
61 K. Yamasaki, S. Juodkazis, M. Watanabe, H.-B. Sun, S. Matsuo, H. Misawa, *Appl. Phys. Lett.* **2000**, *76*, 1000.
62 S. Juodkazis, S. Matsuo, H. Misawa, V. Mizeikis, A. Marcinkevicius, H. B. Sun, Y. Tokuda, M. Takahashi, T. Yoko, J. Nishii, *Appl. Surf. Sci.* **2002**, *197–198*, 705.
63 T. Hashimoto, S. Juodkazis, H. Misawa, *Appl. Phys. A: Mater. Sci. Process.* **2006**, *83*, 337. doi:10.1007/s00339-006-3501-8
64 M. Watanabe, S. Juodkazis, H.-B. Sun, S. Matsuo, H. Misawa, *Phys. Rev. B* **1999**, *60*, 9959.
65 H.-B. Sun, S. Juodkazis, M. Watanabe, S. Matsuo, H. Misawa, J. Nishii, *J. Phys. Chem.* **2000**, *104*, 3450.
66 S. Juodkazis, A. Marcinkevicius, M. Watanabe, V. Mizeikis, S. Matsuo, H. Misawa, *Proc. SPIE* **2000**, *4347*, 212.
67 M. Watanabe, S. Juodkazis, J. Nishii, S. Matsuo, H. Misawa, *Proc. SPIE* **2002**, *4637*, 159.
68 A. Marcinkevicius, S. Juodkazis, M. Watanabe, M. Miwa, S. Matsuo, H. Misawa, J. Nishii, *Opt. Lett.* **2001**, *26*, 277.
69 S. Juodkazis, H. Misawa, T. Hashimoto, E. Gamaly, B. Luther-Davies, *Appl. Phys. Lett.* **2006**, *88*, 201909.
70 K. Sun, Z. Li, K. Ueno, S. Juodkazis, S. Noji, H. Misawa, *Electrophoresis* **2007**, *28*, 1572.
71 S. Matsuo, Y. Tabuchi, T. Okada, S. Juodkazis, H. Misawa, *Appl. Phys. A: Mater. Sci. Process.* **2006**, *84*, 99.
72 M. Watanabe, S. Juodkazis, H.-B. Sun, S. Matsuo, H. Misawa, M. Miwa, R. Kaneko, *Appl. Phys. Lett.* **1999**, *74*, 3957.
73 M. Watanabe, S. Juodkazis, H. Sun, S. Matsuo, H. Misawa, *Appl. Phys. Lett.* **2000**, *77*, 13.
74 M. Watanabe, S. Juodkazis, S. Matsuo, J. Nishii, H. Misawa, *Jpn. J. Appl. Phys.* **2000**, *39*, 6763.
75 S. Juodkazis, A. V. Rode, E. G. Gamaly, S. Matsuo, H. Misawa, *Appl. Phys. B: Lasers Opt.* **2003**, *77*, 361.
76 S. Juodkazis, E. Gaižauskas, V. Jarutis, J. Reif, S. Matsuo, H. Misawa, *J. Phys. D: Appl. Phys.* **2006**, *39*, 50. doi:10.1088/0022-3727/39/1/009
77 K. Miura, J. Qiu, H. Inouye, T. Mitsuyu, K. Hirao, *Appl. Phys. Lett.* **1997**, *71*, 3329.
78 S. Juodkazis, M. Sudzius, V. Mizeikis, H. Misawa, E. G. Gamaly, Y. Liu, O. A. Louchev, K. Kitamura, *Appl. Phys. Lett.* **2006**, *89*, 062903.
79 E. G. Gamaly, S. Juodkazis, V. Mizeikis, H. Misawa, A. V. Rode, W. Z. Krolikowski, K. Kitamura, *Curr. Appl. Phys.* **2008**, *8*, 416.
80 S. Juodkazis, T. Kondo, H. Misawa, A. Rode, M. Samoc, B. Luther-Davies, *Opt. Express* **2006**, *14*, 7751.
81 S. Juodkazis, K. Nishimura, H. Misawa, T. Ebisui, R. Waki, S. Matsuo, T. Okada, *Adv. Mater.* **2006**, *18*, 1361. doi:10.1002/adma.200501837
82 M. Mazilu, S. Juodkazis, T. Ebisui, H. Misawa, *Appl. Phys. A: Mater. Sci. Process.* **2007**, *86*, 197. doi:10.1007/s00339-006-3732-8
83 J. Durnin, J. Miceli, J. Eberly, *Phys. Rev. Lett.* **1987**, *58*, 1499.
84 A. Marcinkevicius, S. Juodkazis, S. Matsuo, V. Mizeikis, H. Misawa, *Jpn. J. Appl. Phys.* **2001**, *40*, L1197.
85 A. Marcinkevicius, S. Juodkazis, V. Mizeikis, S. Matsuo, H. Misawa, *Proc. SPIE* **2001**, *4271*, 150.
86 E. Gaižauskas, E. Vanagas, V. Jarutis, S. Juodkazis, V. Mizeikis, H. Misawa, *Opt. Lett.* **2006**, *31*, 80.
87 S. Juodkazis, H. Misawa, *Forming tiny 3D structures for micro- and nanofluidics* in *SPIE Newsroom: Micro/Nano Lithography & Fabrication*, **2007**. doi:10.1117/2.1200612.0510; http://spie.org/x8371.xml
88 S. Matsuo, S. Juodkazis, H. Misawa, *Appl. Phys. A: Mater. Sci. Process.* **2005**, *80*, 683. doi:10.1007/s00339-004-3108-x
89 A. Moroni, J. Mijovic, E. M. Pearce, C. C. Foun, *J. Appl. Polym. Sci.* **1986**, *32*, 3761.
90 S. Juodkazis, T. Kondo, V. Mizeikis, S. Matsuo, H. Murata, H. Misawa, *Proc. SPIE* **2003**, *4977*, 94.
91 K. K. Seet, V. Mizeikis, S. Juodkazis, H. Misawa, *Appl. Phys. Lett.* **2006**, *88*, 221101.
92 K. Ueno, S. Juodkazis, M. Mino, V. Mizeikis, H. Misawa, *J. Phys. Chem. C* **2007**, *111*, 4180. doi:10.1021/jp068243m
93 K. Ueno, S. Juodkazis, V. Mizeikis, K. Sasaki, H. Misawa, *J. Am. Chem. Soc.* **2006**, *128*, 14226. doi:10.1021/ja0645786
94 K. Ueno, V. Mizeikis, S. Juodkazis, K. Sasaki, H. Misawa, *Opt. Lett.* **2006**, *30*, 2158.
95 V. Mizeikis, K. K. Seet, S. Juodkazis, H. Misawa, *Opt. Lett.* **2004**, *29*, 2061.
96 B. Cumpston, S. Ananthavel, S. Barlow, D. Dyer, J. Ehrlich, L. Erskine, A. Heikal, S. Kuebler, I.-Y. Lee, D. Mccord-Maughon, J. Qin, H. Rockel, M. Rumi, X.-L. Wu, S. Marder, J. Perry, *Nature* **1999**, *398*, 51.
97 K. K. Seet, Ph.D. Thesis, Hokkaido University, Hokkaido, **2006**.
98 N. Tétreault, G. von Freymann, M. Deubel, M. Hermatschweiler, F. Pérez-Willard, S. John, M. Wegener, G. Ozin, *Adv. Mater.* **2006**, *18*, 457.
99 V. Mizeikis, S. Juodkazis, R. Tarozaitė, J. Juodkazytė, K. Juodkazis, H. Misawa, *Opt. Express* **2007**, *15*, 8454.
100 T. Kondo, Ph.D. Thesis, Hokkaido University, Hokkaido, **2005**.
101 T. Kondo, S. Juodkazis, V. Mizeikis, H. Misawa, *J. Non-Cryst. Solids* **2008**, *354*, 1194.
102 D. Bauerle, *Laser Processing and Chemistry*, 2nd ed., Springer, Berlin, **1996**.
103 V. E. Gruzdev, *Proc. SPIE* **2005**, *6256*, 625602.
104 A. Cavalleri, K. Sokolowski-Tinten, J. Bialkowski, M. Schreiner, D. von der Linde, *J. Appl. Phys.* **1999**, *85*, 3301.
105 C. W. Siders, A. Cavalleri, K. Sokolowski-Tinten, C. Toth, T. Guo, M. Kammler, M. H. von Hoegen, K. R. Wilson, D. von der Linde, C. P. J. Barty, *Science* **1999**, *286*, 1340.
106 N. I. Koroteev, I. L. Shumai, *Physics of Strong Laser Radiation*, Science, Moscow, **1991**.
107 Y. B. Band, *Light and Matter: Electromagnetism, Optics, Spectroscopy and Lasers*, Wiley, Chichester, **2006**.
108 S. A. Akhmanov, V. A. Vyslouch, A. Chirkin, *Optics of Femtosecond Laser Pulses*, Nauka, Moscow, **1988**.
109 A. Couairon, A. Mysyrowicz, *Phys. Rep.* **2007**, *441*, 47.
110 H. Misawa, H.-B. Sun, S. Juodkazis, M. Watanabe, S. Matsuo, *Proc. SPIE* **2000**, *3933*, 246.
111 L. Ding, J. Song, Z. Sun, L. Deng, Z. Wang, *Chin. Opt. Lett.* **2006**, *4*, 617.
112 V. I. Berezhiani, S. M. Mahajan, Z. Yoshida, M. Pekker, *Phys. Rev. E* **2002**, *65*, 046415.
113 O. Efimov, S. Juodkazis, H. Misawa, *Phys. Rev. A* **2004**, *69*, 042903.
114 V. E. Gruzdev, *Phys. Rev. B* **2007**, *75*, 205106.
115 S. Juodkazis, T. Kondo, A. Rode, S. Matsuo, H. Misawa, *Proc. SPIE* **2004**, *5662*, 179.
116 W. A. Harrison, *Electronic Structure and the Properties of Solids*, Dover publications, Inc., New York, **1989**.
117 P. G. Eliseev, O. N. Krokhin, I. N. Zavestovskaya, *Appl.*

Surf. Sci. **2005**, *248*, 313.
118 P. G. Eliseev, I. N. Zavestovskaya, S. Juodkazis, H. Misawa, 17th European Conf. Laser Interaction with Matter, Moscow, Russia, October 7–11, **2002**.
119 L. V. Keldysh, *Zh. Eksp. Teor. Fiz.* **1964**, *47*, 1945.
120 S. I. Kudryashov, M. Kandyla, C. A. D. Roeser, E. Mazur, *Phys. Rev. B* **2007**, *75*, 085207.
121 Z. Sacks, G. Mourou, R. Danielius, *Opt. Lett.* **2001**, *26*, 462.
122 S. Paul, S. I. Kudryashov, K. Lyon, S. D. Allen, *J. Appl. Phys.* **2007**, *101*, 043106.
123 N. Taniguchi, *On the Basic Concept of Nanotechnology* in *Proc. ICPE*, **1974**.
124 R. Feynman *J. Microelectromech. Syst.* **1992**, *1*, 60.
125 R. Feynman *J. Microelectromech. Syst.* **1993**, *2*, 4.
126 The concept of nanotechnology (the term coined by Taniguchi in 1974[123]) was introduced by Feynman in his lectures "There's plenty of room at the bottom" (1960)[124] and "Infinitesimal machinery" (1983).[125] In this, he considered that by developing scaleable manufacturing system, a device could be made which could make a miniature replica of itself, and so on down to molecular level.
127 K. E. Drexler, *Nanosystems: Molecular Machinery, Manufacturing and Computation*, Wiley, New York, 1992.
128 P. N. Lebedev, *Ann. Phys.* **1901**, *311*, 433.
129 T. Tlusty, A. Meller, R. Bar-Ziv, *Phys. Rev. Lett.* **1998**, *81*, 1738.
130 N. Murazawa, S. Juodkazis, Y. Tanamura, H. Misawa, *Jpn. J. Appl. Phys.* **2006**, *45*, 977. doi:10.1143/JJAP.45.977
131 T. Tlusty, private communication: the form of equations which are given here differ from those in Ref. 128 and were kindly provided by Dr. T. Tlusty.
132 N. Murazawa, S. Juodkazis, H. Misawa, *Eur. Phys. J. E* **2006**, *20*, 435.
133 R. Beth, *Phys. Rev.* **1936**, *50*, 115.
134 L. Allen, M. W. Beijersbergen, R. J. C. Speeuw, J. P. Woerdman, *Phys. Rev. A* **1992**, *45*, 8185.
135 R. C. Gauthier, *Appl. Phys. Lett.* **1995**, *67*, 2269.
136 E. Higurashi, H. Ukita, H. Tanaka, O. Ohguchi, *Appl. Phys. Lett.* **1994**, *64*, 2209.
137 R. C. Gauthier, *Appl. Phys. Lett.* **1996**, *69*, 2015.
138 Z.-P. Luo, Y.-L. Sun, K.-N. An, *Appl. Phys. Lett.* **2000**, *76*, 1779.
139 P. Galajda, P. Ormos, *Appl. Phys. Lett.* **2001**, *78*, 249.
140 H. Misawa, S. Juodkazis, *Prog. Polym. Sci.* **1999**, *24*, 665.
141 S. Juodkazis, M. Shikata, T. Takahashi, S. Matsuo, H. Misawa, *Jpn. J. Appl. Phys.* **1999**, *38*, L518.
142 S. Juodkazis, M. Shikata, T. Takahashi, S. Matsuo, H. Misawa, *Appl. Phys. Lett.* **1999**, *74*, 3627.
143 S. Juodkazis, S. Matsuo, N. Murazawa, I. Hasegawa, H. Misawa, *Appl. Phys. Lett.* **2003**, *82*, 4657.
144 N. Murazawa, S. Juodkazis, V. Jarutis, Y. Tanamura, H. Misawa, *Europhys. Lett.* **2006**, *73*, 800. doi:10.1209/epl/i2005-10457-7
145 N. Murazawa, S. Juodkazis, S. Matsuo, H. Misawa, *Small* **2005**, *1*, 656. doi:10.1002/smll.200500038
146 N. Murazawa, S. Juodkazis, H. Misawa, *Opt. Express* **2006**, *14*, 2481.
147 M. E. J. Friese, T. A. Nieminen, H. Rubinsztein-Dunlop, N. R. Heckenberg, *Nature* **1998**, *394*, 348.
148 T. Takasone, S. Juodkazis, Y. Kawagishi, A. Yamaguchi, S. Matsuo, H. Sakakibara, H. Nakayama, H. Misawa, *Jpn. J. Appl. Phys.* **2002**, *41*, 3015.
149 S. Juodkazis, K. Fujiwara, T. Takahashi, S. Matsuo, H. Misawa, *J. Appl. Phys.* **2002**, *91*, 916.
150 M. Miwa, S. Juodkazis, H. Misawa, *Jpn. J. Appl. Phys.* **2000**, *39*, 1930.
151 N. Murazawa, S. Juodkazis, H. Misawa, *J. Phys D: Appl. Phys.* **2005**, *38*, 2923.
152 H. Misawa, S. Juodkazis, A. Marcinkevicius, V. Mizeikis, A. Yamaguchi, H. Sun, S. Matsuo, Micromechanotronics & Human Sci., MHS-2000, IEEE Proc., Nagoya, Japan, October 22–25, **2000**, pp. 23–33.
153 S. Juodkazis, N. Mukai, R. Wakaki, A. Yamaguchi, H. Misawa, *Nature* **2000**, *408*, 178.
154 A. Ashkin, *Phys. Rev. Lett.* **1970**, *24*, 156.
155 K. Svoboda, S. M. Block, *Annu. Rev. Biophys. Biomol. Struct.* **1994**, *23*, 247.
156 Y. Inouye, S. Shoji, H. Furukawa, O. Nakamura, S. Kawata, *Jpn. J. Appl. Phys.* **1998**, *37*, L684.
157 K. Sasaki, M. Tsukima, H. Masuhara, *Appl. Phys. Lett.* **1997**, *71*, 37.
158 H. A. Kramers, *Physica* **1940**, *7*, 284.
159 L. I. McCann, M. Dykman, B. Golding, *Nature* **1999**, *402*, 785.
160 J. Hofkens, J. Hotta, K. Sasaki, H. Masuhara, K. Iwai, *Langmuir* **1997**, *13*, 414.
161 T. A. Smith, J. Hotta, K. Sasaki, H. Masuhara, Y. Itoh, *J. Phys. Chem. B* **1999**, *103*, 1660.
162 A. Suzuki, T. Tanaka, *Nature* **1990**, *346*, 345.
163 M. Ishikawa, H. Misawa, N. Kitamura, R. Fujisawa, H. Masuhara, *Bull. Chem. Soc. Jpn.* **1996**, *69*, 59.
164 M. Annaka, T. Tanaka, *Nature* **1992**, *355*, 430.
165 Y. Hirokawa, T. Tanaka, *J. Chem. Phys.* **1984**, *81*, 6379.
166 S. Hirotsu, Y. Hirokawa, T. Tanaka, *J. Chem. Phys.* **1987**, *87*, 1392.
167 H. Schild, *Prog. Polym. Sci.* **1992**, *17*, 163.
168 F. Ilmain, T. Tanaka, E. Kokufuta, *Nature* **1991**, *349*, 400.
169 Y. Takeoka, A. N. Berker, R. Du, T. Enoki, A. Grosberg, M. Kardar, T. Oya, K. Tanaka, G. Wang, X. Yu, T. Tanaka, *Phys. Rev. Lett.* **1999**, *82*, 4863.
170 T. Oya, T. Enoki, A. Grosberg, S. Masamune, T. Sakiyama, Y. Takeoka, K. Tanaka, G. Wang, Y. Yilmaz, M. S. Feld, R. Dasari, T. Tanaka, *Science* **1999**, *286*, 1543.
171 P. Chiarelli, D. De Rossi, *Prog. Colloid. Polym. Sci.* **1988**, *48*, 4.
172 T. Tanaka, L. O. Hocker, B. G. Benedek, *J. Chem. Phys.* **1973**, *59*, 5151.
173 M. Fritze, M. B. Stern, P. W. Wyatt, *Opt. Lett.* **1998**, *23*, 141.
174 A. Schoenle, S. W. Hell, *Opt. Lett.* **1998**, *23*, 325.
175 H. G. Schild, D. A. and, *J. Phys. Chem.* **1990**, *94*, 4352.
176 R. Wiesendanger, *Scanning Probe Microscopy and Spectroscopy*, Cambridge University Press, Cambridge, **1994**.
177 M. Shibayama, T. Tanaka, *Adv. Polym. Sci.* **1993**, *109*, 1.
178 E. Geissler, A. M. Hecht, *Macromolecules* **1980**, *13*, 1276.
179 H. Misawa, M. Koshioka, K. Sasaki, N. Kitamura, H. Masuhara, *J. Appl. Phys.* **1991**, *70*, 3829.
180 H. Misawa, K. Sasaki, M. Koshioka, N. Kitamura, H. Masuhara, *Appl. Phys. Lett.* **1992**, *60*, 310.
181 H. Misawa, N. Kitamura, H. Masuhara, *J. Am. Chem. Soc.* **1991**, *113*, 7859.
182 H. Shimizu, T. Miyoshi, S. Kiyono, *Proc. SPIE* **2000**, *4088*, 385.

183 S. Juodkazis, H. Misawa, *J. Micromech. Microeng.* **2004**, *14*, 1244.
184 R. Menzel, *Photonics. Linear and Nonlinear Interactions of Laser Light and Matter*, Springer, Berlin, **2001**.
185 T. Takasone, S. Juodkazis, S. Matsuo, A. Yamaguchi, K. Sasaki, J.-I. Hotta, H. Misawa, *Proc. SPIE* **2002**, *4830*, 212.
186 P. W. Barber, S. C. Hill, *Light Scattering by Particles: Computational Methods* in *Advanced Series in Applied Physics*, World Scientific Publishing Co., Pte. Ltd., Singapore, **1990**.
187 J. Guck, R. Ananthakrishnan, T. J. Moon, C. C. Cunningham, J. Käs, *Phys. Rev. Lett.* **2000**, *84*, 5451.
188 G. Strobl, *The Physics of Polymers*, 2nd ed., Springer Verlag, Berlin, **1997**.
189 V. V. Datsuyk, S. Juodkazis, H. Misawa, *J. Opt. Soc. Am. B* **2005**, *22*, 1471.
190 V. V. Datsyuk, S. Juodkazis, H. Misawa, *Phys. Rev. A* **2005**, *72*, 025803.
191 V. Datsyuk, *Phys. Rev. A* **2007**, *75*, 043820.
192 M. Burns, J.-M. Fournier, J. A. Golovchenko, *Science* **1990**, *249*, 749.
193 L. Cai, X. Yang, Y. Wang, *Opt. Lett.* **2002**, *27*, 900.
194 E. Dufresne, D. Grier, *Rev. Sci. Instrum.* **1998**, *69*, 1974.
195 J. Arlt, V. Garces-Chavez, W. Sibbett, K. Dholakia, *Opt. Commun.* **2001**, *197*, 239.
196 S. Tatarkova, W. Sibbett, K. Dholakia, *Phys. Rev. Lett.* **2003**, *91*, 038101.
197 H. Misawa, M. Koshioka, K. Sasaki, N. Kitamura, H. Masuhara, *Chem. Lett.* **1991**, 469.
198 H. He, M. E. J. Friese, N. R. Heckenberg, H. Rubinsztein-Dunlop, *Phys. Rev. Lett.* **1995**, *75*, 826.
199 M. P. MacDonald, L. Peterson, K. Volke-Sepulveda, J. Arlt, W. Sibbett, K. Dholakia, *Science* **2002**, *296*, 1101.
200 L. Paterson, M. P. MacDonald, J. Arlt, W. Sibbett, P. E. Bryant, K. Dholakia, *Science* **2001**, *292*, 912.
201 M. P. MacDonald, K. Volke-Sepulveda, L. Peterson, J. Arlt, W. Sibbett, K. Dholakia, *Opt. Commun.* **2002**, *201*, 21.
202 H. Misawa, S. Juodkazis, *Light forms tiny 3D structures* in *SPIE Newsroom: Micro/Nano Lithography & Fabrication*, **2006**. doi:10.1117/2.1200603.0181; http://spie.org/x8778.xml
203 *Record-breaking laser is hot stuff* in *Nature News*, **2006**. doi:10.1038/news060508-14; http://www.nature.com/news/2006/060508/full/060508-14.html
204 Y. Bellouard, A. Said, M. Dugan, P. Bado, *Opt. Express* **2004**, *12*, 2120.
205 Y. Li, K. Itoh, W. Watanabe, K. Yamada, D. Kuroda, J. Nishii, Y. Jiang, *Opt. Lett.* **2001**, *26*, 1912.
206 R. An, Y. Li, Y. Dou, D. Liu, H. Yang, Q. Gong, *Appl. Phys. A: Mater. Sci. Process.* **2006**, *83*, 27.
207 K. Ke, E. F. Hasselbrink, A. J. Hunt, *Anal. Chem.* **2005**, *77*, 5083.
208 Y. Kawaguchi, T. Sato, A. Narazaki, R. Kurosaki, H. Niino, *J. Photochem. Photobiol., A* **2006**, *182*, 319.
209 G. Kopitkovas, T. Lippert, C. David, S. Canulescu, A. Wokaun, J. Gobrecht, *J. Photochem. Photobiol., A* **2004**, *166*, 135.
210 R. Bohme, K. Zimmer, *Appl. Surf. Sci.* **2007**, *253*, 8091.
211 Y. Yu, M. Nakano, T. Ikeda, *Nature* **2003**, *425*, 145.
212 P. Tabeling, *Introduction to Microfluidics*, Oxford University Press, Oxford, **2005**.

Saulius Juodkazis is Associate Professor at the Research Institute for Electronic Science of Hokkaido University, Japan. He received his Physics Diploma in 1986 from Vilnius University, Lithuania. In 1997, he received Ph.D. in physics and material science jointly from Vilnius University and l'Université Claude Bernard of Lyon, France. He carried out post-doctoral research at Tokushima University, Japan, in 1997–2000 working in Nitride Photonic Semiconductor and Photonic Nano-Materials Laboratories. He became assistant professor at University of Tokushima in 2000 and from 2004 he joined Hokkaido University. His current interests include space-time-spectrum-resolved characterization of light-matter interactions in micro-domain, nano-photonics/plasmonics, laser tweezers, and applications of ultra-fast laser pulses. With coauthors he published over 100 scientific papers.

Vygantas Mizeikis was born in 1965 in Lithuania. He has received Ph.D. degree in physics from Vilnius University in 1997. Since then he worked at the Institute of Applied Science and Materials Research, Vilnius University as a researcher. In 2000 he has joined Satellite Venture Business Laboratory, The University of Tokushima, as a post-doctoral researcher. From 2003 to 2007 he has worked in a research project funded by Japan Science and Technology (JST) Agency at Hokkaido University. His current scientific interests include laser microstructuring of materials, and its application for the fabrication of photonic band gap structures.

Shigeki Matsuo was born in Morioka, Japan in 1967. He graduated and received his doctoral degree from Tohoku University in 1995. He worked as a post-doc at the Institute for Molecular Science (IMS) in 1995–1997. He joined the University of Tokushima in 1997 where he is associate professor. His research interests include femtosecond laser microfabrication/spectroscopy.

Kosei Ueno was born in Saitama, Japan in 1974. He is Assistant Professor at the Research Institute for Electronic Science of Hokkaido University, Japan. He has received Ph.D. degree in chemistry from Hokkaido University in 2004. From 2004 to 2006, he works in Prof. Misawa's laboratory as a JSPS research fellow. His current scientific interests are fabrication and optical characterization of gold nanostructures defined with sub-nanometer precision and its plasmonic applications especially in the research field of chemistry.

Award recipient

Hiroaki Misawa is Professor at the Research Institute for Electronic Science at Hokkaido University, Japan. He obtained his B.Sc. degree in engineering from the Department of Engineering at Tokyo Metropolitan University in 1979, received M.Sc. in Engineering from the University of Tsukuba in 1981 and completed his Ph.D. at the Department of Chemistry there in 1984. After post-doctoral positions at the Universities of Texas (USA) and Tsukuba (Japan) and an assistant professorship at Tsukuba University, he joined the Micro-photo-conversion project (Exploratory Research for Advanced Technology ERATO of Japan Science & Technology Agency (JST)). He then moved on to the Department of Engineering at the University of Tokushima in 1993 and was promoted to full Professor in 1995. His current research interests include photochemistry, light-matter interaction, ultra-fast processes in materials, photonic crystals, and plasmonics. He has authored more than 200 papers.